

Self-differential GNSS for synthetic aperture radar

Implementation and evaluation of a GNSS method for obtaining a relative position estimation of an airborne synthetic aperture radar

Master's thesis in "Wireless, photonics and space engineering" and "Communication engineering"

ERIK ENGLUND

DANIEL JOHANSSON

MASTER'S THESIS 2022

Self-differential GNSS for synthetic aperture radar

Implementation and evaluation of a GNSS method for obtaining a
relative position estimation of an airborne synthetic aperture radar

ERIK ENGLUND
DANIEL JOHANSSON



CHALMERS
UNIVERSITY OF TECHNOLOGY

Department of Space, Earth and Environment
Geoscience and Remote Sensing
CHALMERS UNIVERSITY OF TECHNOLOGY
Gothenburg, Sweden 2022

Self-differential GNSS for synthetic aperture radar
Implementation and evaluation of a GNSS method for obtaining a relative position
estimation of an airborne synthetic aperture radar
ERIK ENGLUND
DANIEL JOHANSSON

© ERIK ENGLUND, 2022.
© DANIEL JOHANSSON, 2022.

Supervisors: Patrik Dammert, SAAB, Surveillance
Joakim Strandberg, SAAB, Surveillance
Gary Smith-Jonforsen, SAAB, Surveillance
Examiner: Jan Johansson, Chalmers, Department of Space, Earth and Environment,
Geoscience and Remote Sensing

Master's Thesis 2022
Department of Space, Earth and Environment
Geoscience and Remote Sensing
Chalmers University of Technology
SE-412 96 Gothenburg
Telephone +46 31 772 1000

Cover: Visualization of GNSS method time-differenced carrier phase for obtaining
relative position

Typeset in L^AT_EX
Printed by Chalmers Reproservice
Gothenburg, Sweden 2022

Self-differential GNSS for synthetic aperture radar
Implementation and evaluation of a GNSS method for obtaining a relative position
estimation of an airborne synthetic aperture radar
ERIK ENGLUND

DANIEL JOHANSSON
Department of Space, Earth and Environment
Chalmers University of Technology

Abstract

Obtaining an accurate position while using global navigation satellite systems (GNSS) signals, for example the global positioning system (GPS) can be useful for various applications. In this study a self-differential GNSS method called time-differenced carrier phase (TDCP) is evaluated as a measure of acquiring a precise position of a GNSS receiver mounted on a helicopter. The derived position from this method is used to produce synthetic aperture radar (SAR) images with a radar system developed by Saab AB called CARABAS-3 (VHF-band). A high accuracy of the helicopter's flight path yields SAR images with higher focus and thus, contain more information about the desired target area. The most common method used for calculating such a position is called real time kinematic (RTK) which relies on ground based reference stations that are placed in the vicinity of the planned flight path in order to differentiate and correct for the impact of atmospheric delay among other system derogating effects. These reference stations limit the mobility of the system, since they need to be manually placed prior to flight. However, the TDCP method eliminates the need for these reference stations by using self-differentiation. A prominent difference between these methods is that in RTK the position is derived as an absolute value but with TDCP the position is relative former positions. If this relative position is accurate to the real flight path but with a constant bias it will still be admissible for SAR processing and it will not affect the focus of the image. The method has been implemented in Matlab and Python and compared with RTK processed flight paths of the helicopter in order to evaluate the performance of the method. The TDCP method effectively removes the need for the reference stations while having a median drift of less than 100 mm in each dimension compared to the RTK solutions, which is sufficient for focusing radar images taken with the CARABAS-3 system. For higher frequency (microwave) SAR systems, TDCP can aid automatic focusing algorithms (autofocus), by improving initial estimates of the synthetic aperture and hence reducing the computational demands.

Keywords: TDCP, RTK, GNSS, GPS, CARABAS-3, SAR, flight path, self-differencing, sp3, broadcast orbits, autofocus

Acknowledgements

We would like to express our appreciation for all the interesting and valuable discussions with our supervisors Joakim Strandberg and Gary Smith-Jonforsen, and for their general support during the project. As well as as appreciation to our supervisor Patrik Dammert for initiating this project, and Martin Ankel for lending us the necessary equipment to succeed. We would also like to show gratitude towards our boss Per Gustavsson for a warm welcoming at Saab. And lastly, we would like to thank our examiner Jan Johansson for introducing us to the topic of GNSS and for all the help along the way.

ERIK ENGLUND, Gothenburg, June 2022
DANIEL JOHANSSON, Gothenburg, June 2022

List of Acronyms

Below is the list of acronyms used throughout the thesis, listed in alphabetical order:

AOA	Angle Of Attack
BOC	Binary Offset Carrier
BPSK	Binary Phase Shift Keying
C/A-code	Course Acquisition (GPS code)
CDMA	Code Divison Multiple Access
CRF	Celestial Reference Frame
ECEF	Earth-Centered, Earth-Fixed (reference frame)
ENU	East North Up (Directions)
FDMA	Frequency Division Multiple Access
GEO	Geostationary Orbit
GDOP	Geometric DOP
GLONASS	Globalnaja Navigatsionnaja Sputnikovaja Sistema
GNSS	Global Navigation Satellite System
GPS	Global Positioning System
HDOP	Horizontal DOP
HVHF	High Very High Frequency (High frequencies of VHF band)
IGS	International GNSS Service
INS	Inertial Navigation System
KPPP	Kinematic Precise Point Positioning
LHC	Left Hand Circular (polarization of signal)
LPF	Low Pass Filter
LVHF	Low Very High Frequency (Low frequencies of VHF band)
MEO	Medium Earth Orbit
M-code	Military Code (GPS code)
P-code	Precise Code (GPS code)
PDOP	Positional DOP
PPP	Precise Point Positioning
PRI	Pulse Repetition Interval
QZSS	Quazi-Zenith Satellite System
RHC	Right Hand Circular (polarization of signal)

RINEX	Receiver Independent Exchange Format
RMSE	Root Mean Square Error
RTK	Real Time Kinematic
SAR	Synthetic Aperture Radar
SLAR	Side-Looking Airbourne Radar
TDCP	Time Differenced Carrier Phase
TRF	Terrestrial Reference Frame
VDOP	Vertical DOP
VHF	Very High Frequency (30 - 300 MHz)
Y-code	Anti Spoofing Code (GPS code)
ZHD	Zenith Hydrostatic Delay
ZTD	Zenith Total Delay
ZWD	Zenith Wet Delay



Contents

List of Acronyms	viii
List of Figures	xv
List of Tables	xix
1 Introduction and background	1
1.1 Purpose	1
1.2 Goal	2
1.3 Report outline	2
2 Synthetic aperture radar (SAR)	5
2.1 CARABAS-3	7
2.2 High frequency applications	8
3 Introduction to GNSS	11
3.1 Satellite orbits and specifications	12
3.2 Signal theory	14
3.2.1 Signal Generation - Atomic clocks	17
3.3 GNSS receivers	17
3.3.1 Carrier phase measurements	18
3.4 Dilution of precision (DOP)	22
3.5 Antenna models	23
3.6 Possible error sources when using GNSS	24
3.6.1 Vertical component	24
3.6.2 Multipath	25
3.6.3 Relativistic effects	26
4 GNSS processing	27
4.1 RINEX	27
4.2 U-center	27
4.3 RTKLIB	28
4.4 Satellite Orbits	28
4.4.1 International GNSS Service (IGS)	29
4.4.2 GeoBM GmbH	30
4.4.3 Broadcasted navigation message	30
4.4.4 Elevation angle from navigation message	33

4.5	Reference frames	34
5	Positioning using GNSS	37
5.1	Real time kinematic (RTK)	37
5.2	Precise point positioning (PPP)	37
5.3	Time differenced carrier phase (TDCP)	38
5.4	Referenced TDCP	42
5.5	Error sources and mitigation for TDCP	43
5.5.1	Cycle slip detection	43
5.5.2	Outlier detection	45
6	Performance of TDCP	49
6.1	TDCP and outliers	49
6.2	TDCP and positional drift	51
6.3	TDCP method using different sp3-files	53
6.4	TDCP versus RTK	54
6.5	Analysis of SAR runs	56
6.6	Possible errors from SAR runs	59
6.7	Error in starting position	62
6.8	Processed SAR image	64
7	Discussion	67
7.1	Future of TDCP	67
7.1.1	Future improvements for project	67
8	Conclusion	69
A	Number of runs processed for spliced flight data	I
B	Stats of SAR runs from single SAR flights	III

List of Figures

2.1	SAR integration angle, stripmap mode, adapted from [1]	6
2.2	Slow platform movements Δr_{slow} (top) and fast platform movements Δr_{fast} (bottom)	7
2.3	CARABAS-3 SAR mounted on a helicopter, Source: Saab AB	8
3.1	Example of bad coverage due to low elevation angle	12
3.2	GPS orbital planes with 55° inclination. Source: U.S Government [15]	13
3.3	GPS satellite, block III. The large panels are the solar arrays and the GPS antennas are the array of 12 elements at the bottom of the spacecraft. Source: U.S Government [15]	14
3.4	Modulated carrier with C/A-code. The time scales included in the picture is not to scale since the frequency of the carrier is higher than the frequency of the code.	15
3.5	Modulated carrier with C/A-code and navigation message. Adapted from J.C. Ramón [17]	16
3.6	Receiver correlation between satellite clock and receiver clock	18
3.7	Different elevation angles ϵ of satellites compared to the receiver. $\epsilon = 90^\circ$ is zenith and $\epsilon = 15^\circ$ is the lowest elevation angle for "simple" mapping functions.	20
3.8	Beat signal for detecting phase ambiguity. Adapted from [19]	21
3.9	Dilution of precision, left with high DOP, right with low DOP.	22
3.10	Phase center for choke-ring and mobile antenna	24
3.11	Phase center for Antcom antennas and GNSS puck antenna	24
3.12	Example of GNSS receiver experiencing multipath	25
4.1	Satellite data collection, from raw GNSS data to RINEX	28
4.2	Process from .ubx to .obs with U-center and RTKLIB	28
4.3	IGS tracking stations for all GNSS across the world. The green dots represent healthy stations that have collected data within the last ten days, the orange squares healthy stations that have collected data within the last month and the red triangles represent the faulty stations in the network. Source: International GNSS Service (IGS) [33]	29
5.1	TDCP basic geometry. The image represents the method in two different time epochs t_j and one epoch before t_{j-1} . Where the subscripts S and U represents satellite and user (receiver). Source: Modified from [42]	38

5.2	TDCP flow chart. Source: Modified from [42]	42
5.3	Code and phase differences ΔC and ΔL on data with a large cycle slip	44
5.4	Outliers in measured velocity for stationary receiver. The blue points are positions when integrating over the velocities with the outliers, and the orange points are positions calculated when the outliers in the velocities are removed. The outliers that are removed are highlighted with red circles.	46
5.5	Exponentially weighted moving average (EWMA) filter on velocity data for stationary receiver.	47
6.1	Impact of cycle slips on measurement data: Velocities on still/stationary receiver. Top left: Velocities in ENU on still receiver, shows many cycle slips. Top right: Velocities in ENU on still receiver with obvious outliers removed. Bottom center: Positional (EN) difference from velocities with outliers (blue) and with outliers removed (orange).	50
6.2	Test setup, receiver placed on board. Moved along a straight line	51
6.3	Position result (EN) of straight line test, The plot shows the receiver moving towards the end of the track and then returning to the starting position.	52
6.4	3D Receiver position as a function of time for straight line test.	52
6.5	TDCP velocity in ENU for stationary receiver during one hour using navigation message (top left), using an sp3-file with five minute update rate (top right) and using an sp3-file with 15 minute update rate (bottom center).	53
6.6	Difference in satellite positions over one hour between navigation message and sp3-files. Left: five minute sp3-file (gbm) compared to navigation message. Right: 15 minute sp3-file (igu) compared to navigation message	54
6.7	Part of CARABAS-3 flight with RTK solution in RED and straight SAR runs highlighted in blue.	55
6.8	Velocity for SAR run with added EWMA outlier detection for east (green), north (blue) and up (red).	56
6.9	One SAR run (90 s) is split in to multiple shorter runs.	57
6.10	East median drift. Created using navigation message (left) for satellite positions and compared to drift with sp3 (right)	58
6.11	North median drift. Created using navigation message for satellite positions and compared to drift with sp3 (right)	58
6.12	Up median drift. Created using navigation message for satellite positions and compared to drift with sp3 (right)	58
6.13	3D positional drift for TDCP using satellite navigation message and sp3-files with a line at 100 mm	59
6.14	Drift in the north direction	60
6.15	CARABAS flight with SAR runs highlighted in blue for FWD0929b, the SAR runs are flown in an eastern direction with very little difference in north.	60

6.16	Sky-plot with visible satellites along with elevation and azimuth angle, from Carabas-3 flight FWD0929b	61
6.17	DOP from Carabas-3 flight FWD0929b where the yellow line represents geometric DOP (GDOP), the purple position DOP (PDOP), the green number of satellites available, the red vertical DOP (VDOP) and the blue horizontal DOP (HDOP).	62
6.18	3D positional drift from different starting positions using sp3-files for satellite positions	63
6.19	3D positional drift from different starting positions using navigation file for satellite positions	63
6.20	Satellite image from flight FWD0611a, the red arrows mark a power line which is visible in the SAR images, and the circles mark radio masts. Source: Google Earth [50].	64
6.21	Processed SAR image from flight FWD0611a with RTK solution at the top and TDCP at the bottom. The white lines in the SAR images are electrical power lines which reflect the transmitted signal. And to the right in the pictures is a field with radio towers that also appears as bright spots on the SAR images. The blurry part in the top right corner is where the aircraft has flown, and no data is available in that area because of that, thus the unfocused area.	65
B.1	FWD0929a Flight path with highlighted SAR runs (top) with East North and Up drifts using GPS navigation message	IV
B.2	FWD0929a DOP presented in number of visible satellites divided by DOP (top). Yellow line = GDOP, purple = PDOP, green = number of satellites visible, red = VDOP and blue = HDOP. Together with a skyplot for the satellites during the measurements (bottom)	V
B.3	FWD0929b Flight path with highlighted SAR runs (top) with East North and Up drifts using GPS navigation message	VI
B.4	FWD0929b DOP presented in number of visible satellites divided by DOP (top). Yellow line = GDOP, purple = PDOP, green = number of satellites visible, red = VDOP and blue = HDOP. Together with a skyplot for the satellites during the measurements (bottom)	VII
B.5	FWD0611a Flight path with highlighted SAR runs (top) with East North and Up drifts using GPS navigation message	VIII
B.6	FWD0611a DOP presented in number of visible satellites divided by DOP (top). Yellow line = GDOP, purple = PDOP, green = number of satellites visible, red = VDOP and blue = HDOP. Together with a skyplot for the satellites during the measurements (bottom)	IX
B.7	FWD1002c Flight path with highlighted SAR runs (top) with East North and Up drifts using GPS navigation message	X
B.8	FWD1002c DOP presented in number of visible satellites divided by DOP (top). Yellow line = GDOP, purple = PDOP, green = number of satellites visible, red = VDOP and blue = HDOP. Together with a skyplot for the satellites during the measurements (bottom)	XI

B.9 FWD0604a Flight path with highlighted SAR runs (top) with East North and Up drifts using GPS navigation message XII

B.10 FWD0604a DOP presented in number of visible satellites divided by DOP (top). Yellow line = GDOP, purple = PDOP, green = number of satellites visible, red = VDOP and blue = HDOP. Together with a skyplot for the satellites during the measurements (bottom) XIII

B.11 FWD1017b Flight path with highlighted SAR runs (top) with East North and Up drifts using GPS navigation message XIV

B.12 FWD1017b DOP presented in number of visible satellites divided by DOP (top). Yellow line = GDOP, purple = PDOP, green = number of satellites visible, red = VDOP and blue = HDOP. Together with a skyplot for the satellites during the measurements (bottom) XV

B.13 FWD1017c Flight path with highlighted SAR runs (top) with East North and Up drifts using GPS navigation message XVI

B.14 FWD1017c DOP presented in number of visible satellites divided by DOP (top). Yellow line = GDOP, purple = PDOP, green = number of satellites visible, red = VDOP and blue = HDOP. Together with a skyplot for the satellites during the measurements (bottom) XVII

List of Tables

2.1	Position requirements for LVHF and HVHF SAR-systems when experiencing fast/slow variations. The position requirement is displayed in mm and indicates the maximum 3D error from the true flight path.	8
3.1	Characteristics of the GNSS constellations at the time of the report	11
3.2	Code specification	16
4.1	IGS orbital products. Source: IGS [34]	30
4.2	Kepler elements inside navigation message. Note that the symbols are different from the ones in table 4.3	31
4.3	Derived orbital elements inside navigation message. Note that the symbols are different from the ones in table 4.2	31
4.4	Constants used for calculating satellite position	32
A.1	Number of runs processed from four SAR flights.	II

1

Introduction and background

The content of this report is done in collaboration with Saab Surveillance. A part of Saab AB's area of operation is design and development of products that ensure territorial integrity and security via airborne surveillance. An efficient way of achieving this is through the use of radars on airborne vehicles to produce images of the activity on the ground beneath. Unlike the more conventional method of obtaining information via optical images, radar has the ability to work both day and night and in all weathers if designed properly [1].

In order to achieve images of high quality and resolution, a special kind of method for obtaining radar imagery called synthetic aperture radar (SAR) is being used. A common requirement when producing high resolution images from a SAR system is that the position of the airborne vehicle on which the SAR is mounted has to be known. The more accurate of a position, the higher the quality of the resulting radar image due to a reduction of phase errors in the signals [2]. However, when using SAR this position can be relative to former positions and does not have to be an absolute position [3]. This allows for tracking the airborne vehicle with methods that rely solely on relative positioning, which has the advantage of potentially requiring less processing time, increase the mobility of the system and can enables implementation in close to real time. Having the possibility to collect data and information in real time is crucial for surveillance applications, since targets can move and change positions over long time periods. The tracking of the airborne vehicle will be done with satellite signals from different global navigation satellite systems (GNSS). A conventional method for tracking airborne vehicles using GNSS for SAR applications is by using real time kinematic (RTK). This method relies on the placement of a ground station with a known location that is used as a reference position for the airborne receiver. This is not always a practical solution since it is necessary to make measurements in areas where ground stations can not be established. Thus, a different method, that does not rely on these ground stations will be evaluated in order to cover situations where base stations are unavailable.

1.1 Purpose

The purpose of the project is to evaluate the accuracy of the method time differenced carrier phase (TDCP) for relative positioning using GNSS signals. If this method is

deemed viable for use with SAR processing it might be possible to remove the need to set up a ground reference station before the flight. The main application for the system is to be implemented on a helicopter with Saab's SAR system CARABAS-3. If acceptable results can be extracted from the method it could be implemented for real time surveillance applications in various radar products.

1.2 Goal

In order for the method to be acceptable when being used for radar imagery, the derived position of the flight path has to be accurate on sub decimeter level for over a minute. In addition, the position has to be accurate when the receiver is traveling at velocities above 30 m/s since this is a common velocity for the used helicopter. This is the required minimum performance of the system. If better accuracy and velocity thresholds can be obtained it will improve the quality and allow the use of the method on even faster aircraft platforms and for SAR systems with higher operating frequency, which are able to capture radar images with higher resolution.

1.3 Report outline

Chapter 2

"Synthetic aperture radar (SAR) gives a brief description of the principles of synthetic aperture radar. The need for measurements of the radar motion are described, and the requirements on positioning accuracy defined. The CARABAS-3 system used in this report is presented in more detail, as well as some considerations on requirements for other radar systems.

Chapter 3

"Introduction to GNSS" presents an introduction to GNSS and more specific the functions of the GPS system. The chapter involves theory about the signals transmitted from the satellites and considerations that have to be made when GPS is used to determine a position of a receiver.

Chapter 4

"GNSS processing" contains more detailed information about what is required in order to process GNSS signals and how this can be done.

Chapter 5

"GNSS positioning" explains different methods that could be viable to use in order to get a position of the CARABAS-3 system. The chapter describes how the method time-differenced carrier phase works and the theory behind it.

Chapter 6

"Performance of TDCP" gives an in depth description of the performance of the method, it presents how the end result can be affected by using different receivers, antennas and satellite positions. The chapter gives detailed information about how the system performs when applied to real SAR runs, as well as the resulting SAR

image.

Chapter 7

"Discussion" explains the possible future improvements for the method and for the project generally.

Chapter 8

"Conclusion" provides information about if the system could be implemented for SAR processing, and the possibilities and limits for the system.

Appendix A-B contains the segmented SAR runs used for analysing the method, along with information about each SAR run/flight.

2

Synthetic aperture radar (SAR)

Synthetic aperture radar (SAR) is a form of radar imaging that can provide detailed images of stationary targets. The main reason to use SAR instead of a conventional optical photograph of an area is that unlike optical images, a SAR image can be formed in all weathers during both day and night and still provide high quality information. When using long wavelengths it is possible to look through canopies and find hidden targets, as well as seeing structures that are buried shallowly under ground.

In a radar image, good resolution in all directions is often needed to distinguish multiple targets that may blend together as a single target if the resolution is inadequate. In radars mounted on flying vehicles the cross range resolution is dependent on the beam width of the antenna and the range from the antenna to the target. These kind of radars are known as SLAR or side looking airborne radar. By flying in this way the resolution of the image is limited by the length of the antenna aperture (D) as in equation (2.1) below [1].

$$\rho_{cr} = R \frac{\lambda}{D} \tag{2.1}$$

Where R is the range between the target and the antenna, and λ is the wavelength of the radar signal. For long ranges a large antenna aperture is needed to get satisfactory resolution for a given wavelength. Increasing the antenna size is only viable to a certain extent, until antennas become impractical because of their large size.

To overcome the problem with antenna size SAR can be used. SAR uses coherent pulses at specific pulse repetition intervals (PRI) to create an image. When using SAR the image resolution is limited by the wavelength and the integration angle θ . The integration angle is the angle between the first and last pulse that creates the synthetic aperture. An illustration of the integration angle over four pulses can be seen in figure 2.1.

When using SAR the cross-range resolution ρ_{cr} is limited by the integration angle

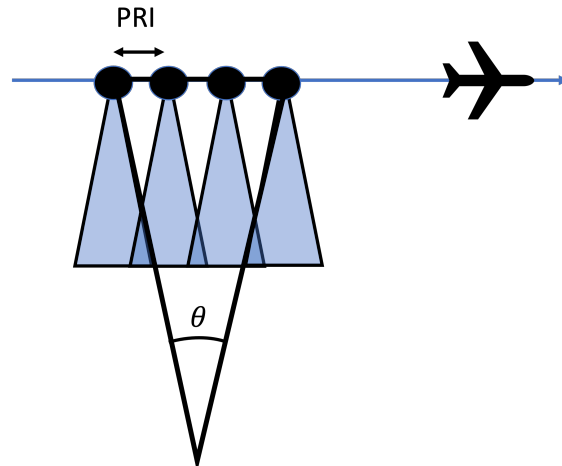


Figure 2.1: SAR integration angle, stripmap mode, adapted from [1]

and the wavelength as in equation (2.2) below.

$$\rho_{cr} = \frac{\lambda}{2\theta_{int}} \quad (2.2)$$

The wavelength of SAR systems can be different depending on the design and application for each system. For most uses, SAR systems are deployed to work from the X-band (8 - 12 GHz) down to the P-band (0.3 - 1 GHz) with wavelengths spanning from around 3 cm to 100 cm. When using higher frequency systems the signals will bounce off the tops of targets. For example a resulting SAR image of a forest with this frequency will provide an image of the landscape and tops of trees. When using longer wavelengths the signals will instead move through the leaves and detect targets below the canopies [4].

To get a clear and focused image from SAR the exact flight path has to be known when processing the data. If an incorrect flight path is handed to the algorithms that create the final image, the final image will be unfocused and difficult to interpret [5]. The SAR processing algorithms use coherent processing of the signal phases that are received. A positional error will cause the signal to travel shorter or further which will cause the signal to change its phase and thus decreasing the focus of the image [2]. It is however not necessary that a precise absolute position of the SAR is available. The processed image will still be focused given the exact relative position of the flight path. With relative position it is implied that the positional change is known from one time period to another, in the case of SAR, the position change needs to be known between the radar pulses. This will ensure that there is no phase error in the received pulses.

To get well focused images from a SAR-system, the accuracy of motion measurement in terms of relative position has to be accurate differently depending on how smooth the variations are along the synthetic aperture. For fast motions of the platform the requirements of the accuracy will be higher than for slow/linear variations of

motion. This makes the motion tracking of more importance when using systems that experience fast motion variations along the aperture such as fighter jets and drones, and a bit more lenient when using systems with slow motion variations such as helicopters. An illustration of such movements can be seen in figure 2.2.

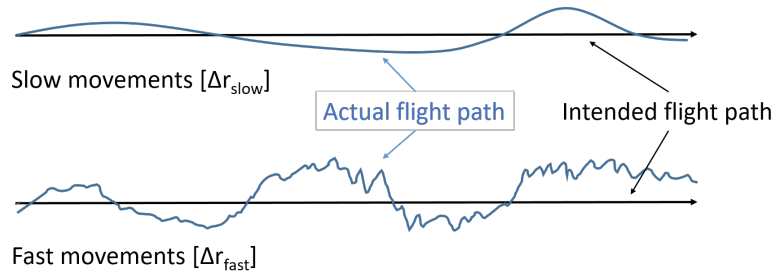


Figure 2.2: Slow platform movements Δr_{slow} (top) and fast platform movements Δr_{fast} (bottom)

In equations (2.3) and (2.4) below the requirements are expressed in wavelengths for slow and fast variations.

$$\Delta r_{slow} < \frac{\lambda_{SAR}}{16} \quad (2.3)$$

$$\Delta r_{fast} < 0.008 \cdot \lambda_{SAR} \quad (2.4)$$

These requirements can be lowered when using autofocus for the SAR-system. This allows for radar images with phase errors to be corrected in order to get a coherent picture of the target. When using SAR signals for radar imaging a present issue is unfocused images due to uncorrected quadratic and high order phase errors. Autofocus algorithms use what is called pull-in range to determine how erroneous the position can be along the aperture for the autofocus to be able to correct and focus an unfocused image. So even if Δr for the SAR platform is larger than the threshold in equations (2.4) and (2.3) above there is still measures to improve the resolution, focus and regain usability of the resulting radar images [6]. The allowable error from the real flight path also depends on the dimension of the error. If the error is along the flight path/aperture the threshold for regaining focus of the image is higher than for across path errors. However, the accuracy of the initial estimation of the flight path affects the processing time of the autofocus algorithms. The closer the initial estimation, the less computationally demanding the autofocus.

2.1 CARABAS-3

The SAR-system that is used for this project is called CARABAS-3 and can be seen mounted underneath a helicopter in figure 2.3. The CARABAS-3 is operational on

two separate frequencies on the VHF-band (30-300 MHz). High VHF (HVHF) with $\lambda = 1$ m (the small vertical antennas) and Low VHF (LVHF) at $\lambda = 5$ m (the larger horizontal antennas) [7].



Figure 2.3: CARABAS-3 SAR mounted on a helicopter, Source: Saab AB

The requirements of the motion estimation is displayed in table 2.1. The requirements changes depending on the type of movement that is introduced for the SAR platform and the operating frequency of the SAR.

Table 2.1: Position requirements for LVHF and HVHF SAR-systems when experiencing fast/slow variations. The position requirement is displayed in mm and indicates the maximum 3D error from the true flight path.

Frequency band	Movement	Position requirement [mm]
HVHF	Δr_{slow}	62.5
HVHF	Δr_{fast}	8.00
LVHF	Δr_{slow}	312.5
LVHF	Δr_{fast}	40.0

2.2 High frequency applications

An alternative to using the low frequency CARABAS-3 system can be to use radar systems with higher frequencies (shorter wavelengths). The primary advantage of using a higher operating frequency for SAR applications is that the acquired resolution from the images can be substantially higher if the frequency is increased, according to equation (2.2) above. A higher resolution is desirable since the resulting images will contain more information about the target. However, a higher operating frequency would also require a more precise determination of the flight path since the requirements in equation (2.3) and equation (2.4) above have to be fulfilled.

In practise this would subsequently resolve in that a SAR system with an X-band operating frequency (8-12 GHz or $\lambda = 2.5 - 3.75$ cm) would require a position

accuracy of 1.875 mm for slow variations and 0.24 mm for fast variations¹. This precision has to be maintained for the duration of data collecting from the SAR. Thus, reducing the time of a SAR run can be a viable option.

When using high frequency and or high velocity systems the integration time needed to create a synthetic aperture will be shorter. Short wavelengths (high frequencies) reduce the needed integration angle to get a certain resolution is smaller than for using larger wavelengths in accordance with equation (2.2). Also, if the platform velocity is higher the needed time to fly along the aperture is decreased. A common method used for complementing the flight path estimation from GNSS is to introduce inertial navigation system (INS) that may include barometers, gyroscopes, accelerometers among other units [8]. These can be made to cooperate using sensor fusion to add redundancy in the position solution and thus, increasing positional accuracy. These INS devices are prone to significant drift in position when used over time [9]. However, if the integration time of the system is short, highly accurate INS devices can be used in combination with the relative position from GNSS to create a highly accurate position. This position can then be used for the high frequency systems which are very sensitive to errors in position.

¹If 10 GHz is used for the SAR

2. Synthetic aperture radar (SAR)

3

Introduction to GNSS

Global navigation satellite systems (GNSS) is the collective term used for the multiple existing satellite systems that are operational for navigation around the world. There are four global GNSS which have been developed and implemented by different nations. The American global positioning system (GPS), the Russian globalnaja navigatsionnaja sputnikovaja sistema (GLONASS), the Chinese Beidou and the European Galileo. They are all designed and built on similar technology and principles, but there are some differences between the systems. The fundamental idea that each satellite system is built upon is a constellation of satellites that orbits the earth in medium earth orbit (MEO) in order to supply position references across the entire globe. In table 3.1 below some general parameters about the different systems are displayed.

Table 3.1: Characteristics of the GNSS constellations at the time of the report

Parameter	GPS	Galileo	GLONASS	BeiDou
Number of orbital planes	6	3	3	3
Number of satellites	32	30 ¹	24	35 ²
Modulation type	CDMA	CDMA	FDMA	CDMA
Height of MEO ³ [km]	20 200	23 222	19 100	21 500-24 100
Inclination i [°]	55	56	65	55

The number of orbital planes for the systems along with the total number of satellites and height of these, differ a bit from system to system. However, the difference is not that significant since they are designed with the same principles. The more noticeable differences are the modulation type for the systems which are the same except for the GLONASS system. Instead of the more regularly used modulation type code division multiple access (CDMA) the system is based upon frequency division multiple access (FDMA). The difference is that each satellite in the GLONASS constellation will broadcast their signals on different frequencies, historically this was implemented to protect against jamming of the signals since the frequencies

¹30 satellites is the goal for the Galileo system, however at the time this report is being made the number is only 22 operational satellites.

²5 of these 35 satellites are situated in a geostationary orbit, not MEO.

³The height of each MEO orbit is from earth's surface not earth's center.

will alter. However, this is no longer an advantage when compared to the same capacities of CDMA, so the administration of GLONASS have started to turn their system towards a CDMA base instead [10]. The CDMA modulation type is instead based on that all satellites transmit their carriers at the same frequencies but each individual satellite transmits a unique code that is used for identification of the satellite. This is further explained in section 3.2 "Signal theory" below.

The inclination angle i of the orbits will affect the coverage area of each system. If an area is located such that the latitudinal coordinates of a location is higher than the inclination angle of the GNSS orbit, there will be no satellites available in zenith direction. This can degrade the performance of positioning. For this exact reason the GLONASS system is designed to have a higher inclination angle since Russia is located at a high latitude. The higher inclination angle enables better coverage for countries far from the equator (\pm high latitudes ϕ) [11]. In figure 3.1 below an example of bad coverage in urban environments is displayed, for countries with no satellites in zenith this problem will be of higher magnitude than countries at lower ϕ . For the other systems whose countries are located more towards the equator, the inclination angle of the orbit can be lower and the system will still give good coverage.

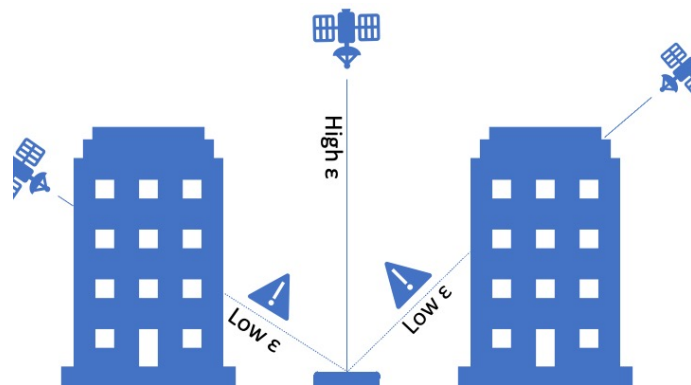


Figure 3.1: Example of bad coverage due to low elevation angle

3.1 Satellite orbits and specifications

To easier understand the fundamentals of GNSS the explanation of the systems is done using the American GPS as a reference. The parts where the different systems differ are explained more in detail as they appear in the text.

The first GNSS system to be developed was the GPS system by the USA. The original idea for such a system originates from the 1960s but it was not developed until the late 1970s when technology had advanced enough for such a system to be constructed. Since the first launch in 1978, 78 satellites has been launched into orbit and out of those, 30 are still operational⁴. The remaining 48 satellites have

⁴As of February 2, 2022, not including two satellites that are in orbit but decommissioned as spares [12]

been retired due to either old technology, faulty components or launch failures. Since there has been over 40 years of development in the area of GPS, the different generations of satellites throughout the years have been divided into three different groups/blocks depending on the production/launch year. In each block there are further sub blocks which categorizes the satellites depending on the technology they contain. Block III which is the present and most technologically advanced generation has only four operational satellites in orbit, the remaining satellites are mostly from block II [13, 14].

The GPS constellation is ideally made up of 32 satellites that are split into six different orbital planes. In figure 3.2 the six orbital planes of GPS are displayed. For GPS to be operational and have coverage all around the globe the system ideally consists of at least 24 out of 32 satellites to be operational. At least four operational satellites are required in each orbital plane in that case, i.e a minimum of 24 satellites for the system to be operational with full earth coverage.

GPS is currently the only system out of the four which relies solely on MEO-satellites to supply coverage for its origin country. In contrast, several nations have deployed support satellites for GPS based applications to further increase coverage in regional areas. One such system is the quazi-zenith satellite system (QZSS) for Japan which supports the GPS constellation with four⁵ satellites in geostationary/elliptical geosynchronous orbits⁶. Other systems have also implemented support satellites in different orbits to further increase the coverage of all the GNSS satellites. Galileo, GLONASS and Beidou have support satellites in inclined geosynchronous and in geostationary orbits that enables the respective system to achieve better coverage of regional areas, focused on the origin country of each system.

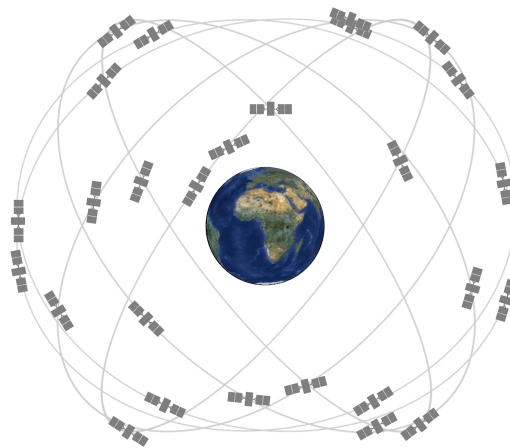


Figure 3.2: GPS orbital planes with 55° inclination. Source: U.S Government [15]

Each GPS satellite is powered with solar panels that automatically direct towards the sun. They are also equipped with small rocket boosters that correct the course

⁵Seven support satellites are planned to be operational by 2023

⁶A Geostationary orbit (height $\approx 35\,786$ km) allows satellites to have the same orbital time as the earth's rotation time.

of the satellite when necessary. This has to be done since there is a natural orbital drift towards the earth due to gravitational pull, which over time will be of larger magnitude than the centrifugal force that affects the satellites in the opposite direction. By increasing this centrifugal force by the use of rocket boosters the satellites can remain in their intended orbits. The GPS antenna consists of an antenna array with 12 antenna elements. This array is continuously directed towards the surface of the earth in order to supply continual availability. In figure 3.3 below a GPS satellite from the latest block III is displayed.



Figure 3.3: GPS satellite, block III. The large panels are the solar arrays and the GPS antennas are the array of 12 elements at the bottom of the spacecraft. Source: U.S Government [15]

3.2 Signal theory

Modern GPS satellites transmit right hand circular polarized (RHC) signals on three different carrier frequencies. These carriers have frequencies which are all based on a multiple of a reference frequency that is created by a local crystal oscillator on the satellites. The reference frequency is 10.23 MHz [16]. The carriers are called L1, L2 and L5. L1 has a frequency of 1575.42 MHz, L2 at 1227.60 MHz and the most modern L5 at 1176.45 MHz which is only available on the latest block III satellites.

The transmitted signals use alteration of the carrier phase as method of transmitting information. The most prominent components of the signals are the carrier frequencies, the course acquisition code (C/A-code), the precise code (P-code), the anti-spoofing code (Y-code) and the navigation message. Each of the codes are transmitted as together with the carrier phase and each individual code has its own application and design. In figure 3.4 below, the C/A-code can be seen modulated on to the carrier phase. For each change of value in the C/A-code the phase of the

carrier shifts 180° in order to carry the information.

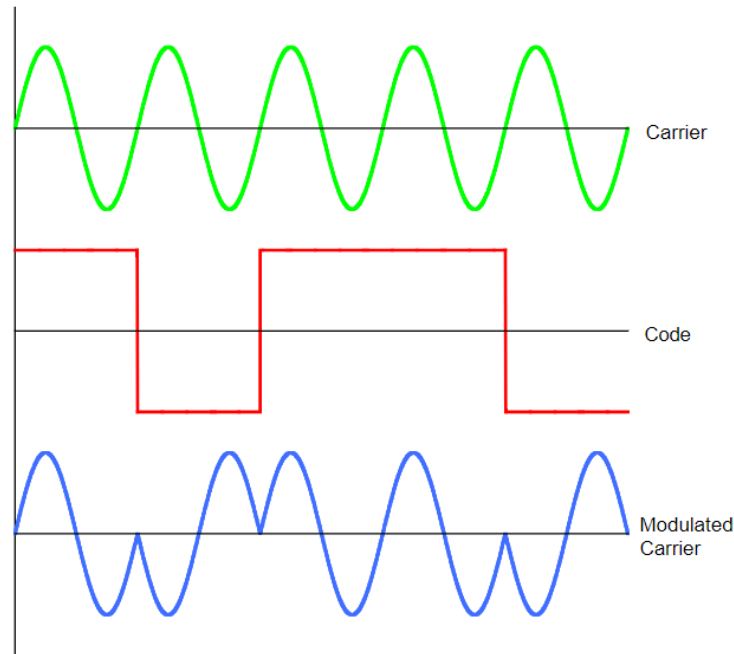


Figure 3.4: Modulated carrier with C/A-code. The time scales included in the picture is not to scale since the frequency of the carrier is higher than the frequency of the code.

The P-code is transmitted at 10.23 MHz on both L1 and L2. When using the P-code for measurements an accuracy of around 0.3 m can be expected, this is around ten times better when compared to the C/A-code (chip rate 1.023 MHz) which has an expected accuracy of around 3 m instead. This is because the P-code has a bit rate which is $10.23 \cdot 10^6$ bit/s, which is 10 times that of the C/A-code and because the P-code gets transmitted on dual frequencies which can mitigate ionospheric impact of the signal. The Y-code is a combination of the P-code and an unknown W-code which enables it to be a restricted signal which requires a special receiver with the correct authorization to interpret the signal. The anti-spoofing enables the code to withstand attempted jamming of the signal. In table 3.2 below additional and more detailed information about the codes are displayed. The navigation message contains information about the satellite orbit, satellite ID and satellite health (if the satellite is out of commission or off track etc.).

Table 3.2: Code specification

Type	Abbr.	Phase shift from L1,L2 [°]	Transmission
Precise code	P-code	90	L1, L2
Coarse Acquisition	C/A-code	180	L1
Anti-spoofing	Y-code	90 (from C/A)	L1, L2
-	W-code	Unknown	L1,L2
Encrypted precise	P(Y)-code	-	L1, L2
Military code	M	-	L1, L2

The M-code is a restricted signal that is used by the military. It is a more modern version of the old military code P(Y)-code and allows for more protection against jamming and is more autonomous in the sense that navigation can be made with only M-code if necessary.

With both the C/A-code, navigation message and carrier the modulated multiplied carrier will look like figure 3.5 below. The C/A-code will phase shift 180°, and all the phase shifting is enabled with binary phase shift keying (BPSK) which is a digital modulation type which can modulate the phase of a signal.

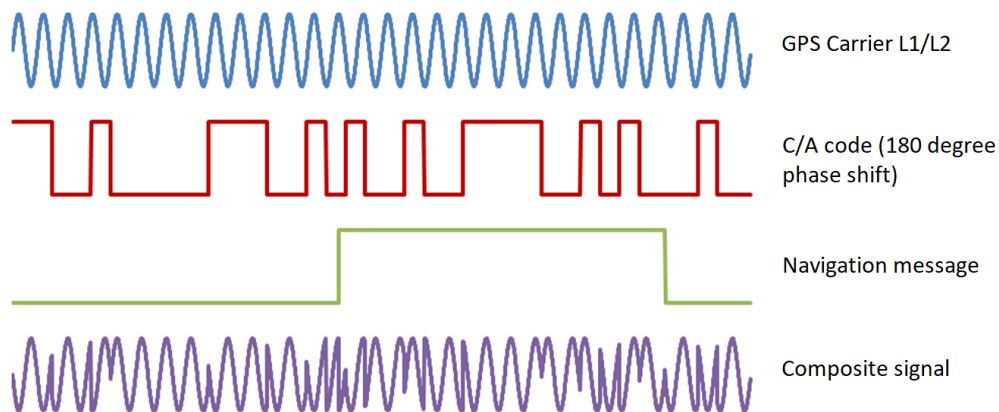


Figure 3.5: Modulated carrier with C/A-code and navigation message. Adapted from J.C. Ramón [17]

Each satellite also broadcasts a navigation message that consists of 5 sub frames on L1 and L2. Sub frame 1 consists of information about the satellite clock and GPS time. Sub frame 2-3 have information about ephemeris(satellite orbit) and the last two sub frames contain information about the almanac components and corrections. The almanac components contain information about the satellites which can be used to calculate the position of each broadcasting satellite [18].

The GPS uses CDMA as a method for multiplexing the signals. This allows for all satellites in the constellation to transmit the carriers on the same frequency and still enable identification of each individual satellite. The ID of each satellite is

transmitted inside the P-code and C/A-code, so by identifying these two codes for each satellite in the receiver it is possible to pin point them back to the specific satellite that transmitted the signal and thus, identify it [19].

3.2.1 Signal Generation - Atomic clocks

In order to generate the signals onboard the satellites, precise atomic clocks are used for the high accuracy that is necessary for satellite positioning. On each satellite atomic clocks are implemented, the most common case consists of two cesium and two rubidium atomic clocks. In order to create a stable and precise clock cesium and rubidium atoms are combined with a quartz crystal. The quartz crystal has the ability to generate a very stable and periodic frequency response when being exposed to a voltage. This combination results in stable atomic clocks which are used in order to generate a frequency of 10.23 MHz which the GPS signals are built upon.

However, these atomic clocks have to be incredibly stable since a faulty time difference ΔT of only 100 nanosecond will result in a deviation of accuracy ΔR of around 30 meters when the signal is transmitted to the earth's surface, since $\Delta R = c\Delta T$. By sending corrections from larger and even more accurate atomic clocks on the ground the natural drift of the atomic clocks on board the satellite can be mitigated. By combining both the corrected clocks and synchronizing the generation of the signal the satellites can provide signals that are accurate to a picosecond level [20].

3.3 GNSS receivers

As explained previously the specific C/A code for each satellite should already be known by the receiver in order to work with a specific GNSS. Thus, a receiver that is intended to be used for uniquely GPS signals will have all of the C/A codes for the active satellites. This receiver can not however be used together with for example the Chinese BeiDou satellites since they use different codes than those of the GPS satellites. The receiver will constantly loop the known codes while simultaneously receiving the signals from all available satellites. The receiver finds which satellites that are sending messages by correlating the received code with the known codes. The codes are designed in such a way that only one satellite has the same code and thus if the correlator in the receiver gets a high enough peak against one of the known codes the receiver knows which satellite is sending the message. There are two different measurements that are important for basic GNSS positioning. These are the code observables and the phase observables.

An example of an observable is what is output by the receiver as a range. The code observable is given in meters and is often referred to as the pseudorange and the phase observable is given in number of wavelengths. The pseudorange is found by correlating the received signal with the known signals in the receiver. When the correct satellite is found there will be a time delay from when the satellite sent the signal to when the receiver receives the same one. This is modeled as $T_R - T_S$ where

T_R is the time of reception in the receiver and T_S is the time of transmission from the satellite. See figure 3.6.

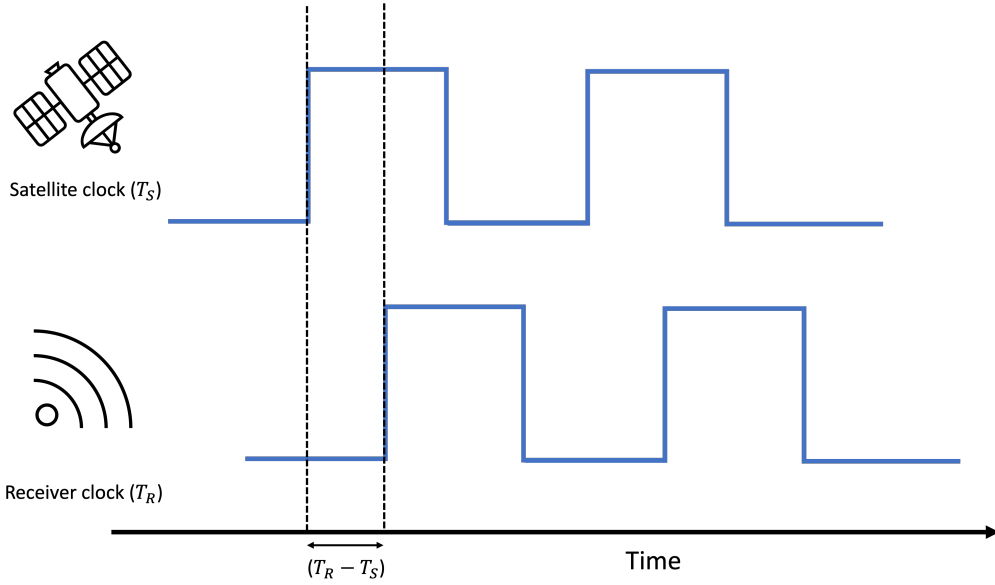


Figure 3.6: Receiver correlation between satellite clock and receiver clock

In real applications the receiver and satellite clocks are not usually perfectly synchronized. This is modeled by adding offsets in time to the reception and transmission times T_S and T_R as in equation (3.1) below.

$$\begin{aligned} T_R &= t_R + \Delta t_R \\ T_S &= t_S + \Delta t_S \end{aligned} \tag{3.1}$$

where t_R and t_S are the true times of reception and transmission respectively and Δt_R and Δt_S are offsets in time due to synchronization errors. Using equation (3.1), the pseudorange is acquired by multiplying the time delay with the speed of light in vacuum, c .

$$\begin{aligned} P &= c(T_R - T_S) \\ &= c[(t_R + \Delta t_R) - (t_S + \Delta t_S)] \\ &= \rho + c(\Delta t_R - \Delta t_S) \end{aligned} \tag{3.2}$$

In the pseudorange equation above, ρ is the actual geometric distance from satellite to receiver (the true range) whilst the second term is the synchronization error from the receiver and satellite clocks. In equation (3.2) the atmospheric and ionospheric delays are not included for simpler understanding.

3.3.1 Carrier phase measurements

To receive the best possible accuracy for the designed system, measurements of the carrier phases are processed. This is a rather precise method of pinpointing a

location using GNSS since compared to C/A-code and P-code the carrier phases has a theoretical accuracy of 1-2 mm since accuracy is proportional to around 1/100 of a wavelength when using phase measurements. Since the carrier L5 is only available on the latest block III of satellites, measurements are instead made on only L1 and L2 which are available for all satellites in the GPS constellation. When the GPS signal propagates from the satellite towards the earth via the atmosphere, it experiences delays due to both the troposphere and the ionosphere. In equation (3.3) below the formula for using carrier phase measurements is displayed.

$$L = \rho + c(\Delta t_R - \Delta t_S) + Z - I + B + \nu \quad (3.3)$$

Where L above is the carrier phase observable, expressed in received carrier wavelengths, $\rho + c(\Delta t_R - \Delta t_S)$ is the pseudorange. In addition to the clock synchronization correction term, other corrections have to be made. Z is the time delay from the troposphere, this term can be divided into zenith wet delay (ZWD) and zenith hydrostatic delay (ZHD) which can be combined to zenith total delay (ZTD). I is the term for ionospheric delay, B is known as the "carrier phase bias" and ν is the additional noise term for residual atmospheric, receiver and ground noise etc. The ionospheric term I has a negative sign due to ionospheric divergence, a phenomenon happening in the ionosphere where the phase velocity increases when compared to the group velocity and thus, experiences a negative delay when travelling through the ionosphere [21].

The tropospheric delay is elevation dependent and can be corrected for by using models. This means that the elevation angle of the satellites compared to the receiver plays a role in how much delay the signal will have before it is received. An example of satellites with different elevation angles can be seen in figure 3.7. The delay is caused by the content of the atmosphere which depends on humidity, pressure and temperature changes and can be split into a wet (ZWD) and dry component (ZHD). These models both monitors the behavior of the troposphere and considers the elevation of the satellites in order to give the most accurate correction. Since the ZTD only accounts for delay in zenith, mapping functions are useful tools when modeling the tropospheric impact. These mapping functions changes in expression depending on the elevation, for elevation angles $\epsilon \geq 15^\circ$ the mapping function can simply be derived as $m(\epsilon) = \frac{1}{\sin(\epsilon)}$ [22].

There are other ways of forming mapping functions but for elevations $\geq 15^\circ$ most mapping functions have similar performance. For elevation angles $\leq 15^\circ$ the models become more and different mapping functions can be used depending on where the receiver is situated [23]. The mapping functions also increase in complexity if azimuth angles and the curvature of the earth are taken into account. In addition the ZTD affects the vertical component of GNSS mostly, so an adequate model is necessary in order to improve the vertical component. The mapping functions are combined with the zenith total delay to give the atmospheric delay Z as in equation

(3.4) below.

$$Z = ZTD \cdot m(\epsilon) \tag{3.4}$$

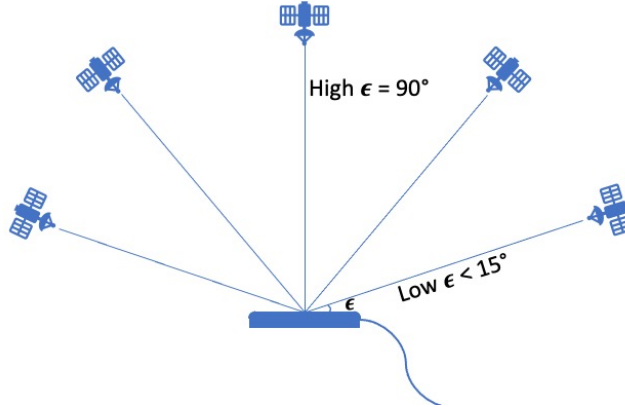


Figure 3.7: Different elevation angles ϵ of satellites compared to the receiver. $\epsilon = 90^\circ$ is zenith and $\epsilon = 15^\circ$ is the lowest elevation angle for "simple" mapping functions.

The ionospheric delay can also be largely corrected for by using a model, however, unlike the correction for the tropospheric impact there is a more effective way to remove most of the impact from the ionosphere. The ionospheric delay differs from the tropospheric delay since it is caused by free electrons⁷. This results in a frequency dependent delay which enables a dual-frequency correction in the form of a linear relation. By deriving this linear relation between the measured carrier phases L1, L2 and the measured codes P1, P2 the impact of the ionosphere can be removed to a degree of 99.5 %. The linear relation is displayed in equation (3.5) and (3.6) below. When using this relation it is necessary to be aware that the signal noise level will be three times as large as the noise level when using L1, L2 and P1, P2 separately. L3 and P3 below can be used as corrected terms for the phase and code measurements.

$$L_3 = 2.546L_1 - 1.546L_2 \tag{3.5}$$

$$P_3 = 2.546P_1 - 1.546P_2 \tag{3.6}$$

The carrier phase bias parameter B is a necessary term to solve in order to solve for L in equation (3.3). This term specifies the number of wavelengths between the receiver and the satellite and can be used to accurately measure the distance between these. The changes from one epoch to another are measured by tracking the carrier phase within the receiver. However, whenever the receiver loses contact with the satellite this phase ambiguity has to be resolved again, this causes what is called a cycle slip and has to be accounted for by implementing an algorithm for detection of these slips. If a cycle slip is present and not dealt with properly, the derived velocity/position will be affected.

⁷The free electrons increases with height and is a direct consequence solar activity [24].

In order to solve for the carrier beat phase ambiguity, the GPS receiver will generate a reference signal $R(t) = R_0 \sin(2\pi\phi_R(t))$ along with the received GPS signal $G(t) = G_0 \sin(2\pi\phi_G(t))$. By mixing these two signals and filtering the high frequency components a beat signal is created which has a frequency and phase equal to the difference of the mixed signals.

$$LPF[R(t) \otimes G(t)] = \frac{R_0 G_0}{2} \cos(2\pi\phi_R(t) - \phi_G(t)) \quad (3.7)$$

where LPF indicates a low pass filter. In figure 3.8 below an example of a beat signal is displayed.

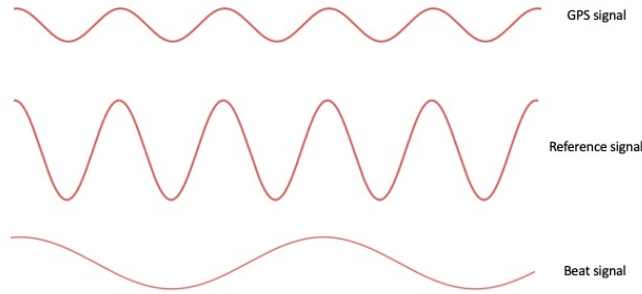


Figure 3.8: Beat signal for detecting phase ambiguity. Adapted from [19]

The recorded phase from the receiver Φ is merely the number of phases passed since the recorder locked on to the transmitted satellite signal. The number of full wavelengths that are lost during transmission before the receiver receives the transmitted signal is the integer phase ambiguity N . The phase reception in the receiver is modelled as in equation (3.8).

$$\Phi + N = \phi_R(t) - \phi_G(t) \quad (3.8)$$

Using one satellite S for transmission the equation can be rewritten as

$$\Phi^s(T) = \phi(T) - \phi^s(t) - N^s \quad (3.9)$$

where T is the time of reception, $\phi(T)$ is the phase of the receivers reference signal and $\phi^s(T)$ is the phase of the received satellite signal. Using this expression and the nominal frequency $f_0 = \frac{\phi(t) - \phi_0}{T(t)}$ it is possible to create the expression for the carrier phase observable as in equation (3.10).

$$\Phi^s(T) = f_0(T_R - T_s) + \phi_0 - \phi_0^s - N^s \quad (3.10)$$

This observable can be converted in to range by multiplying with the corresponding wavelength.

$$\begin{aligned} L(T) &= \lambda_0 \Phi^s(T) \\ &= c(T_R - T_s) + \lambda_0(\phi_0 - \phi_0^s - N) \\ &= c(T_R - T_s) + B \end{aligned} \quad (3.11)$$

This gives the corrected carrier phase equation as in (3.12) [25].

$$L = \rho + c(\Delta t_R - \Delta t_S) + Z - I + B + \nu \quad (3.12)$$

3.4 Dilution of precision (DOP)

One way to decrease position uncertainty when using GNSS measurements is by using receivers that can find multiple GNSS and use the signals from all available satellites. Using more GNSS might help with the satellite geometry by having more satellites available spaced all in all directions. By using only one GNSS such as GPS some satellites may be blocked in view from the receiver. This blockage can be caused by obstructions such as buildings or trees. This is known as dilution of precision or DOP. DOP can be seen as a degradation in performance due to the geometry of the satellites that are visible by the receiver. The DOP can be explained in terms of position uncertainty σ using equation (3.13).

$$\sigma = DOP \cdot \sigma_0 \quad (3.13)$$

In equation 3.13 above the position uncertainty σ is made larger by the DOP which is always a number above 1. DOP in the equation is a term that depends on the receiver position and the position of the satellites. The measurement accuracy σ_0 can be comprised of one or more different DOP:s. The main DOP:s are *PDOP* (positional DOP), *VDOP* (vertical DOP), *HDOP* (horizontal DOP) and *GDOP* (geometric DOP) [26]. For example, the *PDOP* is in turn made up of its uncertainties in the position directions (east, north and up), $PDOP = \sqrt{\sigma_E^2 + \sigma_N^2 + \sigma_U^2}$. The DOP can be reduced by having a better geometry of satellites when measurements are taken with the receiver. A better geometry is available when satellites are visible in a multitude of cardinal directions and preferably with different elevation angles relative to the receiver [27, 26]. Figure 3.9 represents two different cases of satellite geometry resulting in different DOP.

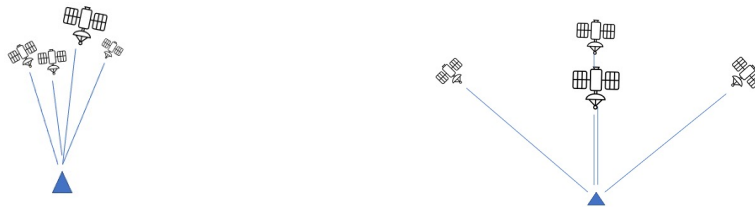


Figure 3.9: Dilution of precision, left with high DOP, right with low DOP.

In the left part of figure 3.9, high DOP is present (increased position uncertainty) since the available satellites are positioned very close to zenith from the receivers point of view. The image on the right has a more diverse positioning of the satellites

which will result in a decreased DOP and thus, a decrease in position uncertainty. The best theoretical satellite geometry for four satellites is three satellites placed with 120° apart in azimuth and elevation just above the horizon with the last satellite placed above in zenith. By maximizing the solid angles between the satellites, better geometry follows.

Using more satellite systems is a way to increase the number of satellites that are visible and ensuring that wherever the receiver is placed, all the visible satellites are used for positioning to reduce the DOP. The same argument can be made when the receiver is located in urban areas with high buildings around. An increase in the number of satellites will yield a better satellite geometry, which gives better coverage in dense urban environments.

3.5 Antenna models

The performance of a GNSS receiver will be impacted by the type of antenna used for the GNSS receiver and the calibration of such antennas. The more modern and advanced antennas are often calibrated in order to have an antenna phase center that is adapted to GNSS signals. The antenna phase center is the point where the receiving signal gets measured, this point varies depending on the frequency and the elevation of the incoming signal so for modern antennas calibrations are necessary for all GNSS signals. The calibration for GLONASS signals are the most complex since the system uses FDMA with different frequencies for all satellites. In the left of figure 3.10 below the different phase centers for a choke-ring antenna can be seen, note how the phase centers changes depending on the incoming carrier. For this specific antenna the height of the antenna is $\lambda/4$ in order to eliminate resulting currents from the signal, this enables the antenna to be more robust against multipath. For smaller antennas i.e ones inside smartphones the phase center can be more complex to accurately calibrate since the device can be twisted and moved in all directions. In the right of figure 3.10 an example of the phase center of a mobile phone is displayed.

The technology for antennas inside smartphones has evolved rapidly the last couple of years but are not as reliable as the bigger external GNSS antennas. The phase centers for the mobile antenna can be spread out in the circle in the top right corner of the mobile phone. As with the other antennas, if this is not properly calibrated for, the precision and accuracy of the system will be compromised. In the right of figure 3.11 a puck antenna which is used for collecting data for the project can be seen. This type of antenna is more sturdy and reliable than the mobile antenna but not as precise as the choke ring, it is however, both more applicable for projects where different measuring locations are used and it is cheaper than the choke-ring antenna. The left of figure 3.11 displays two Antcom 53G1215A-XT1 antennas mounted on the helicopter which are connected to a Javad Delta Duo G2D-4 GNSS receiver. This setup was used to capture the GNSS measurements for the CARABAS-3 flight.

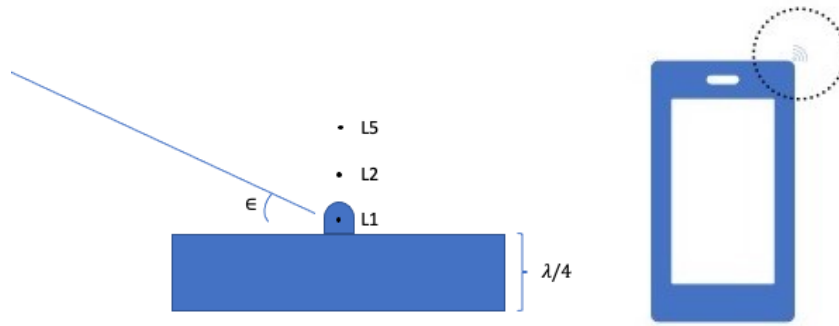


Figure 3.10: Phase center for choke-ring and mobile antenna

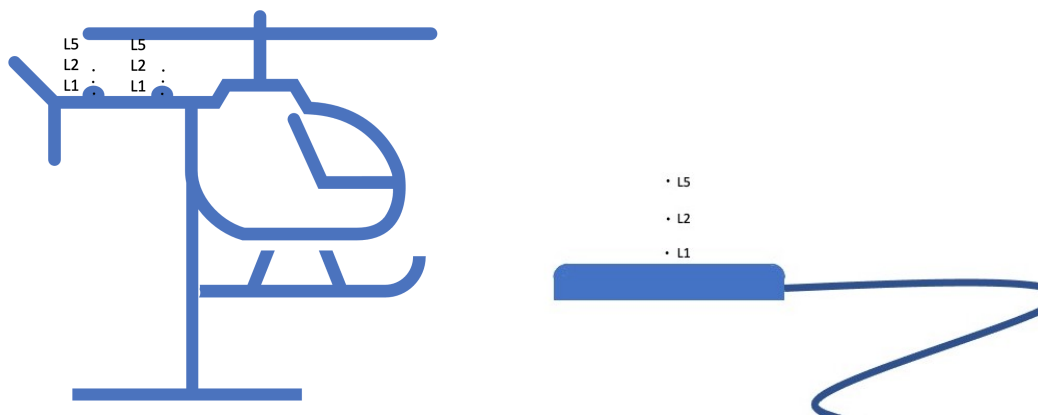


Figure 3.11: Phase center for Antcom antennas and GNSS puck antenna

3.6 Possible error sources when using GNSS

When using GNSS to calculate a position it is necessary to account for error sources that affect the precision and reliability of the derived position. There are measures of mitigation against these error sources that generally counteracts the errors, to at least some degree.

3.6.1 Vertical component

The precision of the vertical component in GNSS applications is more uncertain and less accurate than the horizontal components. This is due to poor satellite geometry since there are no visible satellites beneath the horizon. This is one of the drawbacks when using GNSS technology and it can be mitigated by sensor fusion, where other sensors, e.g barometers/radars/lidars etc will aid in the estimation of the vertical component. In addition to a bad vertical component from satellite geometry, the vertical component will also suffer in accuracy from the tropospheric delay. In order to correct for this delay the use of more comprehensive and detailed mapping functions can be a solution. If more satellites are implemented into the orbits further calculations of the tropospheric impact can be done by mapping the gradient in more

azimuth and elevation angles, making the system more adaptable to tropospheric changes.

3.6.2 Multipath

When testing and validating the method, measurements are collected in urban environments on ground level. This can potentially result in signal multipath. This occurs when the transmitted signal from the satellite gets reflected on a nearby surface to the receiver, the signal will then give a faulty reading inside the receiver. In figure 3.12 an example of multipath occurrence can be seen. The GNSS antenna receives signals that has been reflected on nearby building and experiences multipath.

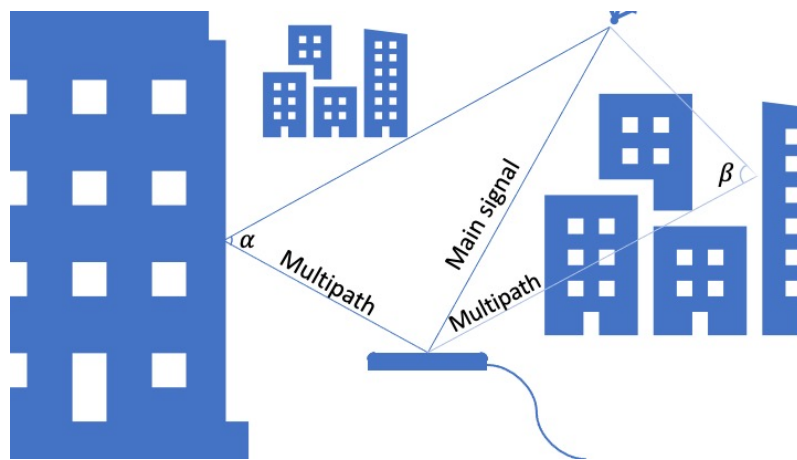


Figure 3.12: Example of GNSS receiver experiencing multipath

There are several different methods that can be implemented in order to mitigate the influence of multipath. The simplest method is to avoid dense urban areas, for the measurements on board the helicopter this problem should be reduced since the helicopter travels at a high altitude over buildings and often outside cities. However, for the validation of the tests on ground level, multipath will be present to a larger degree. Especially since the tests are done in Gothenburg, Sweden which is located at latitude $\phi = 57.7^\circ$, a higher latitude will result in less satellite visible in zenith subsequently, the system relies on low elevation satellites that potentially could be blocked by buildings. A solution to this problem could be to add support satellites such as Japan's QZSS⁸ where satellites are placed in geostationary/incline geosynchronous orbits in order to supply regional coverage for higher latitudes. Or incorporate the GLONASS system in the solution which has an inclination of 65° which allows for satellites in Zenith since the latitudinal coordinates is of lower value than the inclination angle of the orbit.

Another method to mitigate multipath can be to implement a detection algorithm for reflected signals. The transmitted signal from the satellites are generated to

⁸Not applicable in Sweden since the satellites are placed over Japan

be RHC-polarized, when this signal propagates and gets reflected, the signal will experience a different angle of attack (AOA) compared to line-of-sight signal. The polarization will also change from RHC to LHC and predominantly be LHC in the receiver if it is reflected. An algorithm that can detect reflected signals from directly propagated ones could mitigate this problem. However, some errors should still be accounted for since these kind of algorithms most likely will be imperfect [28].

Multipath issues can also be decreased by implementing a binary offset carrier (BOC) modulated signal. A BOC modulated signal is a product of a multiplication between a square wave and the BPSK signal. The result is a signal with less spectral energy concentrated around the carrier frequency. Instead the energy will be concentrated in two separated lobes which subsequently, leads to a much narrower correlation peak inside the receiver. A narrow correlation peak has less deformation due to multipath since the amplitude of the reflected signal will not be inside the narrower spectrum for accepted values. And can thus, be an alternative when eliminating multipath. BOC modulated signals are however, not used on all GNSS⁹ and their signals, since the multiple correlation peaks that is a result from BOC can cause ambiguities that would need corrections [29].

3.6.3 Relativistic effects

The atomic clocks on board the satellites will experience a different gravitational potential when compared to components on the earth. This will result in a natural drift of the clocks due to general relativity and difference in speed. An error of around 50-100 ps is usually accounted for because of this phenomenon, this results in a distance error of around ± 1 cm. The same effects are present when designing models and calculating the satellite orbits. By introducing a time difference factor when constructing the satellites this effect can be mitigated, this is done by changing f_0 to $10.23(1 - 4.4647 * 10^{-10})$ MHz instead of the original $f_0 = 10.23$ MHz. In equation (3.14) below the compensation for the relativistic effect is displayed. This is applied to the carrier phase measurement in order to compensate for the relativistic effects.

$$\Delta_{rel} = -2 \cdot \frac{r^{sat} v^{sat}}{c^2} \quad (3.14)$$

where r^{sat} and v^{sat} are the satellite position and velocity [30].

⁹It is implemented on e.g the Galileo systems E1 signal

4

GNSS processing

4.1 RINEX

The observed satellite data in the receiver will be stored in a format called Receiver INdependent EXchange (RINEX). This is an ASCII based file format which is internationally used as the default format for GNSS observations. The RINEX file contains information about the carrier phases L, the code measurements C, Doppler measurements D and the signal strength (SNR) S among other observations. The RINEX format has the possibility to store data from several GNSS system at the same time with all the observables that the receiver is capable of collecting. When processing GNSS data to get a precise position the RINEX file is a vital part in getting an accurate result, especially in combination with precise orbital parameter of the satellites [31]. Throughout the GNSS history the layout and content of RINEX files have changed multiple times. At current writing time the newest format is RINEX 4.00. With RINEX 4.00 some options that enable better use of the satellite navigation message have been implemented [32]. The layout of the file has changed quite a bit since the early renditions of the RINEX format but some content still remains the same. The newer versions of the RINEX format have capabilities to handle data from Galileo satellites as well as older systems.

In order to process data transmitted from the satellites it is often required to convert the data to the desired RINEX format, since different receivers use different standards for storing GNSS observables.

4.2 U-center

In later sections tests using Ublox receivers are performed. To get the data from these receivers a software program called U-center is used. U-center is a software program developed by Ublox used in order to handle the data from their receivers. When the receivers collect data they are stored in .ubx format which is Ublox standard format storing the data in a binary stream of data. These binary values are then stored in different packets. However, a more standard way of storing GNSS data is in a .obs RINEX file, and the Matlab code used for the main method is also adapted for RINEX files. It is thus necessary to convert the .ubx file from u-center to a .obs file, this can be done with the GNSS open source program RTKLIB and the

subprogram RTKCONV. The process of converting raw GNSS data to the RINEX format is displayed in figure 4.1 below.

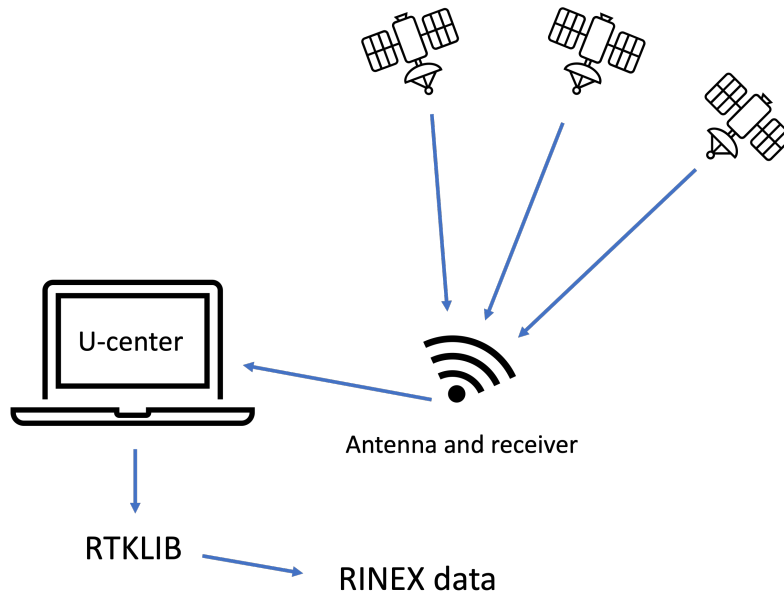


Figure 4.1: Satellite data collection, from raw GNSS data to RINEX

4.3 RTKLIB

RTKLIB is an open source GNSS software program used for handling and processing raw satellite and receiver data. It is particularly used to convert `.ubx` files to RINEX files with the format `.obs` using the built in function `RTKCONV`, which has the ability to convert the files into `.obs` and `.nav` for the navigation message if desired. In figure 4.2 below the process from `.ubx` to `.obs` is displayed.

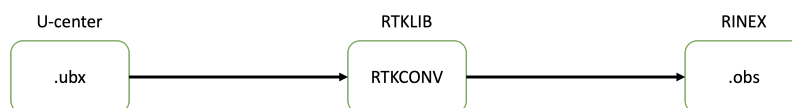


Figure 4.2: Process from `.ubx` to `.obs` with U-center and RTKLIB

4.4 Satellite Orbits

When using GNSS data as a method of deriving a precise position, it is necessary to have accurate positions of the satellites. There are generally two different methods for determining the orbits of the satellites. The first method for obtaining the satellite positions is to use GNSS data products from different suppliers that calculate the orbits and positions via ground based tracking stations. This tracking network is displayed in figure 4.3 below. The data from these stations are then

collected in data analysis centers where the satellite positions etc. are calculated. These files supply the user with satellite positions that have an update rate of five or 15 minutes depending on the supplier, thus interpolating the positions between these points are required. The other method for obtaining the satellite positions is to use a navigation message that the satellites transmit. This navigation message contains orbital parameters that is used in order to calculate the satellite orbits. Since the orbits are calculated as a function of time there is no need to interpolate the positions. There are benefits and drawbacks depending on which method that is used for determining the satellite positions.

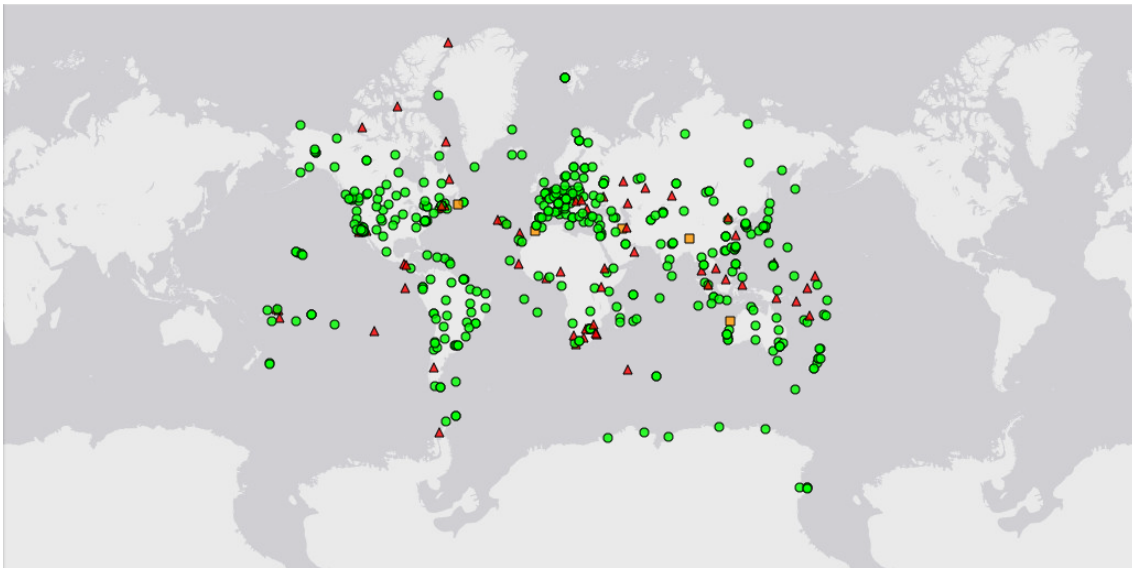


Figure 4.3: IGS tracking stations for all GNSS across the world. The green dots represent healthy stations that have collected data within the last ten days, the orange squares healthy stations that have collected data within the last month and the red triangles represent the faulty stations in the network. Source: International GNSS Service (IGS) [33]

4.4.1 International GNSS Service (IGS)

The international GNSS service (IGS) is an organization that has provided GNSS data products (precise orbits, earth rotation, etc) since 1994. The IGS have analysis and data centers that continuously collect data from the different GNSS and can be used as a tool when high precision and accuracy is needed for a GNSS application.

IGS supplies among other things sp3-files that are files containing information about the satellite orbits. The information about the respective orbit of each satellite is usually obtained by the transmission of a navigation message that is broadcasted from each satellite. However, the precision of the orbits from the navigation message (≈ 100 cm) is not as precise as the orbital information from the sp3-files from the IGS, see table 4.1. The precise orbits of satellites are processed and calculated by combining collected ephemeris data from over 300 ground based GNSS stations. These 300 stations transmit their collected data to special analysis centers where

Table 4.1: IGS orbital products. Source: IGS [34]

Type	Accuracy	Latency	Updates[UTC in h]
Broadcast	≈ 100 cm	real time	-
Ultra-Rapid(predicted half)	≈ 5 cm	real time	03:00,09:00,15:00,21:00
Ultra-Rapid(observed half)	≈ 3 cm	3-9 hours	03:00,09:00,15:00,21:00
Rapid	≈ 2.5 cm	17-41 hours	17:00 daily
Final	≈ 2.5 cm	12-18 days	every Thursday

further calculations and processing are being done in order for IGS to supply the best possible precision for the satellite orbits and store them in the sp3 format.

In table 4.1 below the different types of sp3 data is displayed. When higher precision is needed the latency of the file will increase since more processing is necessary. The selection of sp3 type depends on if the designed system requires good real time applications with less precision or vice versa. The final version of the data is available for all GNSS while ultra-rapid and rapid is only available for the GPS. An error of ≈ 1 cm has to be considered when using products from the IGS, this is because of orbit and clock errors that will affect the final product irrespective of type.

For measurements for this specific application it is desirable to have the sp3 data available as fast as possible since this will result in less time for the final SAR-image to be processed, thus, leading to less information delay for the system. In order to achieve this, sp3-files with the type ultra-rapid is recommended to use. These files consist of observed values and predicted values that are combined in order to create a file with satellite positions for 48 hours. These are obtained in real time with the drawback of being less accurate than final orbits.

4.4.2 GeoBM GmbH

Besides IGS there are several different suppliers of orbital products. For example the German Research Centre for Geosciences, GFZ which provide the same type of products. Multi GNSS products of orbit and clock corrections are available for ultra rapid solutions [35]. The GFZ no longer process ultra rapid solution for satellites, but a spin-off from GFZ called GeoBM GmbH has been created, which can supply ultra rapid solutions that are used in its place [36].

4.4.3 Broadcasted navigation message

Since the TDCP method is fundamentally built on calculations that are relative former position and is not reliant on absolute positions, it can be a viable option to use the broadcasted navigation message from each satellite that includes among other things Kepler elements. These orbital elements can be combined in order to make an expression for a specific orbit which in turn can be used to determine satellite orbits with a precision of ≈ 1 m. Since TDCP is being used, the accuracy of the position of the receiver can still be high since the method uses relative positioning. The benefit of using the navigation message instead of sp3-files is that the need of

relying on an external supplier of files can be eliminated and the system becomes more independent. Another possible benefit from the navigation message is that the periodic tendency that the sp3-files can contain when TDCP is being used, might be reduced, this behaviour is further explained later.

The Kepler elements that are transmitted from the satellites in the navigation messages can be seen in table 4.2 below. These are in turn divided into more detailed orbital elements along with additional information about the satellites according to table 4.3.

Table 4.2: Kepler elements inside navigation message. Note that the symbols are different from the ones in table 4.3

Kepler elements	Notation
Epoch	t
Orbital inclination	i
Right Ascension of Ascending Node	Ω
Argument of Perigee	ω
Eccentricity	e
Mean Motion	N_0
Mean Anomaly	M

Table 4.3: Derived orbital elements inside navigation message. Note that the symbols are different from the ones in table 4.2

Orbital elements	Notation
Sine term, radius	C_{rs}
Cosine term, radius	C_{rc}
Sine term, arg. of latitude	C_{us}
Cosine term, arg. of latitude	C_{uc}
Sine term, inclination	C_{is}
Cosine term, inclination	C_{ic}
LoAN at weekly epoch ¹	Ω
Argument of perigee	ω
Rate of right ascension	Ω_0
Mean motion difference	Δn
Mean anomaly at reference time	M_0
Square root of semimajor axis	\sqrt{A}
Time of ephemeris	t_{eph}
Inclination at reference time	i_0
Rate of inclination angle	i
GPS week	GPS_{week}

¹LoAN = Longitude of ascending node

These elements are used in order to determine the position and velocities of the GPS satellites according to equation (4.1) - equation (4.12) below with the constants displayed in table 4.4 below.

Table 4.4: Constants used for calculating satellite position

Constant	Value	Unit
μ	3.986005e+14	$\left[\frac{m^3}{s^2}\right]$
$\dot{\Omega}_e$	7.29211551467e-5	[°]
A	$\sqrt{A^2}$	[m]
n_0	$\sqrt{\frac{\mu}{A^3}}$	[m]
dt	1e-4	[s]
t_{off}	-0.075	[s]
n	$n_0 + \Delta n$	[m]

Time of ephemeris since start of GPS time 1980-01-06.

$$t_{eph_{start}} = t_{eph} + 7 \cdot 86400 \cdot GPS_{week} \quad (4.1)$$

To get the mean anomaly at the time when the satellite positions are calculated equation (4.2) below is used, where $t = t_{transmit} + \Delta t$ is the satellite transmit time for each satellite with reference to the used epoch and $t_{transmit}, \Delta t$ are the time of transmit and sampling rate.

$$t_{ks_0} = t - t_{eph_{start}} + t_{off} \quad (4.2)$$

The mean anomaly a small time step later will be calculated according to equation 4.3 below and is used to derive the velocities of the satellites.

$$t_{ks} = t - t_{eph_{start}} + t_{off} + dt \quad (4.3)$$

where the mean anomaly is derived as equation (4.4) below.

$$M_k = M_0 + n \cdot t_{ks} \quad (4.4)$$

In order to calculate the eccentric anomaly from the mean anomaly equation (4.5) is used.

$$E_k = M_k + e \cdot \sin(E) \quad (4.5)$$

where $E = M_k \cdot \sin(M_k)$ This is used to derive the true anomaly ν_k with equation (4.6) below. This in turn can be used to calculate the argument of latitude for the satellites according to equation (4.7).

$$\nu_k = \arctan\left(\frac{\sqrt{1-e^2} \cdot \sin(E_k)}{\cos(E_k) - e}\right) \quad (4.6)$$

$$\Phi_k = \nu_k + \omega \quad (4.7)$$

Since the earth is not precisely spherical but more of an ellipsoid the gravitational pull that affects the satellites will be slightly different depending on the satellite positions. To account for this du_k , dr_k , and di_k have to be corrected with second harmonic perturbations according to equation (4.8) and equation (4.9) below.

$$\begin{aligned} du_k &= C_{us} \cdot \sin(2\Phi_k) + C_{uc} \cdot \cos(2\Phi_k) \\ dr_k &= C_{rs} \cdot \sin(2\Phi_k) + C_{rc} \cdot \cos(2\Phi_k) \\ di_k &= C_{is} \cdot \sin(2\Phi_k) + C_{ic} \cdot \cos(2\Phi_k) \end{aligned} \quad (4.8)$$

$$\begin{aligned} u_k &= \Phi_k + du_k \\ r_k &= A(1 - e \cdot \cos(E_k)) + dr_k \\ i_k &= i_0 + di_k + i \cdot t_{ks} \end{aligned} \quad (4.9)$$

Where, u_k is the corrected argument of latitude, r_k is the corrected radius and i_k is the corrected inclination. These are in turn used to calculate the satellite positions in orbit with equation (4.10) below.

$$\begin{aligned} x'_k &= r_k \cdot \cos(u_k) \\ y'_k &= r_k \cdot \sin(u_k) \end{aligned} \quad (4.10)$$

To calculate the satellite positions in the correct reference frame the positions are derived with reference to the inertial coordinate system (WGS-84) according to equation (4.11) below.

$$\begin{aligned} x_k &= x'_k \cdot \cos(\Omega_k) - y'_k \cdot \cos(i_k) \cdot \sin(\Omega_k) \\ y_k &= x'_k \cdot \sin(\Omega_k) + y'_k \cdot \cos(i_k) \cdot \cos(\Omega_k) \\ z_k &= y'_k \cdot \sin(i_k) \end{aligned} \quad (4.11)$$

Where $\Omega_k = \Omega_0 + \dot{\Omega}_e \cdot t_{ks} - \dot{\Omega}_e \cdot t_{kf} - \dot{\Omega}_e \cdot t_{eph}$ represents a frame rotation at the time t_{kf} . This resolves in three dimensional satellite positions as $[x_k \ y_k \ z_k]$ above and satellite velocities according to equation (4.12) below.

$$[v_x \ v_y \ v_z] = \frac{[x_k \ y_k \ z_k]_{t_{ks0}} - [x_k \ y_k \ z_k]_{t_{ks}}}{dt} \quad (4.12)$$

4.4.4 Elevation angle from navigation message

The broadcasted information from the satellites contains information that can be turned into the elevation angle for each satellite. This is done in equation (4.13) to equation (4.17) below. Firstly the derived satellite coordinates have to be three dimensionally rotated in order for the elevation angle to be referenced as 0° at the horizon and 90° in zenith. This is done according to equation (4.13)-(4.16) below.

$$rot_{z-axis} = \begin{bmatrix} (x_k - x_{rec}) \cdot zx_{rot} & (y_k - y_{rec}) \cdot zy_{rot} & (z_k - z_{rec}) \cdot zz_{rot} \end{bmatrix} \quad (4.13)$$

Which is the local coordinates z-rotated in order to derive the elevation angle. Where the rotation matrix is:

$$\begin{bmatrix} zx_{rot} \\ zy_{rot} \\ zz_{rot} \end{bmatrix} = \begin{bmatrix} \cos(\phi_z) & \sin(\phi_z) & 0 \\ -\sin(\phi_z) & \cos(\phi_z) & 0 \\ 0 & 0 & 1 \end{bmatrix} \quad (4.14)$$

and:

$$rot_{x-axis} = \begin{bmatrix} rot_{z-axis}[1] \cdot xx_{rot} & rot_{z-axis}[2] \cdot xy_{rot} & rot_{z-axis}[3] \cdot xz_{rot} \end{bmatrix} \quad (4.15)$$

Which is the local coordinates x-rotated in order to derive the elevation angle together with rot_{z-axis} . The [x] denotes that element x in an array is acquired.

with the rotation matrix:

$$\begin{bmatrix} xx_{rot} \\ xy_{rot} \\ xz_{rot} \end{bmatrix} = \begin{bmatrix} 1 & 0 & 0 \\ 0 & \cos(\phi_x) & \sin(\phi_x) \\ 0 & -\sin(\phi_x) & \cos(\phi_x) \end{bmatrix} \quad (4.16)$$

and the angles (ϕ) being $\phi_z = \frac{\pi}{2} - z_k$ and $\phi_x = x_k + \frac{\pi}{2}$

After the x and z (east, north) coordinates for the satellites are rotated to the correct local coordinates, the elevation angle is calculated by taking the angle of equation (4.17).

$$\epsilon = \sqrt{(rot_{x-axis}[1])^2 + (rot_{x-axis}[2])^2} + i \cdot rot_{x-axis}[3] \quad (4.17)$$

where i represents an imaginary number.

4.5 Reference frames

Another important factor that can influence the performance of a system built upon GNSS technique is the use of reference frames. For objects that are placed on earth its common to use the terrestrial reference frame (TRF) which basically is the reference frame as viewed from earth, with earth's center being the origin (ECEF) of the reference coordinate system. For objects that are located outside earth the celestial reference frame (CRF) is more commonly used. Unlike TRF the CRF is

dependent on a fixed reference point in space instead of earth's center, a common approach to get this is to use quasars, which are light sources so far away in space that they appear to be static. When handling objects both in space and on earth it is necessary to combine and recalculate the objects reference frames in order to accurately pin point their location. If the wrong reference frame is used, the position of the satellites and/or the receiver will be affected and thus, result in a method that has a decreased ability to estimate a position [37, 38].

5

Positioning using GNSS

Since SAR applications need great positional accuracy there is a need for methods that can provide this while not being cumbersome to work with. There are different ways of getting a position using GNSS.

5.1 Real time kinematic (RTK)

A good way of calculating exact positions of a receiver is by using real time kinematic (RTK). RTK works by placing a base station at a known location. This location has to be stationary with constant position while the RTK position is being measured. A rover or a movable receiver is then placed on the target of interest. When the base and the rover both see the same satellites the signals can be combined to reduce possible error sources such as atmospheric delay. The downside of this method for positioning is the need of the base station [39]. Without the base station the rover is affected by the error sources without any real mitigation of these. There are models that can reduce the errors but these models will not be as good as the RTK solution. Depending on factors such as atmospheric conditions, the maximum distance between the rover and base for the method to remain effective will be dynamic. If they are too far away from each other, this will affect the accuracy of the method.

5.2 Precise point positioning (PPP)

Precise point positioning (PPP) and kinematic precise point positioning (KPPP) are methods for obtaining static and moving positions of a receiver using GNSS. The PPP method derives the receiver position by comparing observed (phase + code) and calculated (orbits + models¹) values, where the orbits are obtained with sp3-files. The method relies on estimations of the position via iterations in a Kalman-filter for the observed and calculated values.² For conventional PPP to be precise it is of advantage to capture data during a long period of time since the method is requiring a Kalman-filter, which has a long convergence time in order to estimate the position

¹Models for relativistic effects, tropospheric, ionospheric impact etc.

²In some cases the Kalman-filter is substituted with a more simple least-square-filter

accurately. This processing time increases when KPPP is used, so the convergence time limits the real time application of the method [40, 41].

5.3 Time differenced carrier phase (TDCP)

Accurate estimations of the velocity of a GNSS receiver can be useful in several different applications, especially for the case with a SAR mounted on a helicopter since the precision of the flight path is an important parameter for the performance of the SAR processing. The flight path can be derived from the velocity estimation of the receiver on board the helicopter. The reason why an accurate flight path is necessary is because this directly correlates with the image quality of the resulting computed SAR image, an imprecise flight path will subsequently lead to an unfocused image with less information as explained in chapter 2 "Synthetic aperture radar" (SAR).

A common way of estimating the velocity is to use what is called the Doppler measurement from the observed variables D1 and D2, which is the Doppler frequency observable on the different carriers L1 and L2. From this Doppler shift between the receiver and satellite, the measurement has an accuracy of about cm/s level. The Doppler shift on i.e L1 is derived from the change in phase between two consecutive epochs on the signal but is limited in its use due to the influence of the phase ambiguity parameter, compared to TDCP. However, there are other methods that theoretically can result in higher precision of the velocity estimation that are on the sub cm/s level.

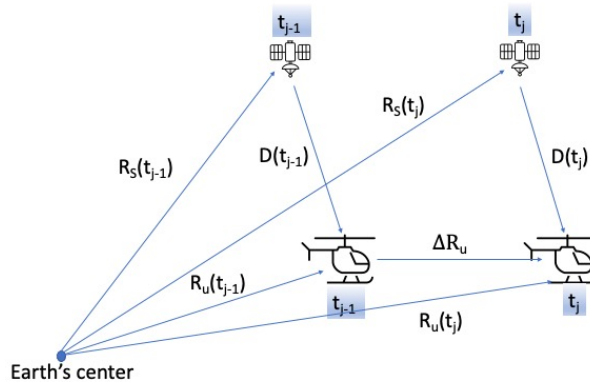


Figure 5.1: TDCP basic geometry. The image represents the method in two different time epochs t_j and one epoch before t_{j-1} . Where the subscripts S and U represents satellite and user (receiver). Source: Modified from [42]

Time differenced carrier phase (TDCP) is one of the techniques used in order to make a velocity estimation with higher precision. This is possible by differencing the received carrier phases from i.e L1 at small sampling intervals from the same satellite. The differences between the measured phases will be used in order to derive the change in range between receiver and satellite between two epochs and later it

will be derived into the user velocity [42]. In figure 5.1 the most basic principle of TDCP with just one satellite is displayed.

With the estimated user velocity it is then possible to predict the position of the receiver if both the direction and velocity change is available and known. In equation (5.1) below the TDCP at two different time epochs is displayed.

$$\Delta L = [L(t_j) - L(t_{j-1})] = \Delta d + c(\Delta t_R - \Delta t_S) + \Delta d_{eph} + \Delta Z - \Delta I + \Delta B + \nu \quad (5.1)$$

Where ΔL the observed change in carrier phase, Δd the change in range between the receiver-satellite for two time epochs, the Δt_R and Δt_S terms are the clock correction terms for receiver and satellite. The Δd_{eph} , ΔI , ΔZ are the ephemeris, ionospheric and tropospheric errors. And $\Delta \nu$ is the noise term from multipath and internal noise of the receiver. The Δ before the terms corresponds to the terms being differenced in time. When differencing at high enough sampling intervals the carrier phase bias between two epochs will barely change and is therefore not included as long as there is not a cycle slip in the receiver.

When solving for the receiver velocity estimation each carrier phase measurement has to be corrected for error sources before any further calculations can be done. Fortunately when differencing some error sources can be mitigated with ease. The ionospheric and tropospheric impact is negligible with the use of models and the fact that the atmospheric properties will not change with any noticeable magnitude during the brief window between measurements, however, when measurements are taken over a large quantity of epochs, this becomes a problem in the form of drift over time. By using sp3-files (or navigation message from satellites) it is also possible to eliminate the ephemeris error and satellites clock error to a level where the remaining error after correction is around ± 5 cm, see table 4.1. After these corrections the formula for TDCP at two different time epochs can be simplified to equation (5.2) below.

$$\Delta L = [L(t_j) - L(t_{j-1})] = \Delta d + c(\Delta t_R - \Delta t_S) + \nu \quad (5.2)$$

Where ν is the term for the noise with additional residual errors from the ionosphere, troposphere, clock and orbit. The Δd is the term that will be used in order to derive the receiver velocity estimation. From figure 5.1 Δd can be expressed as in equation (5.3) below.

$$\Delta d = d(t_j) - d(t_{j-1}) \quad (5.3)$$

The range from the user to the satellite at the different time epochs can be expressed as

$$d(t_j) = e(t_j) \cdot [R_s(t_j) - R_u(t_j)] \quad (5.4)$$

$$d(t_{j-1}) = e(t_{j-1}) \cdot [R_s(t_{j-1}) - R_u(t_{j-1})] \quad (5.5)$$

with the subscripts s and u represents satellite and user and where e is a line of sight (LOS) unit vector. The LOS unit vector is defined as the difference in position between a satellite and the user in one dimension divided by the magnitude of the

total position difference as in equation (5.6) below.

$$\begin{aligned}
 e_x &= \frac{x_s - x_u}{\sqrt{(x_s - x_u)^2 + (y_s - y_u)^2 + (z_s - z_u)^2}} \\
 e_y &= \frac{y_s - y_u}{\sqrt{(x_s - x_u)^2 + (y_s - y_u)^2 + (z_s - z_u)^2}} \\
 e_z &= \frac{z_s - z_u}{\sqrt{(x_s - x_u)^2 + (y_s - y_u)^2 + (z_s - z_u)^2}}
 \end{aligned} \tag{5.6}$$

Where x_s , y_s and z_s are elements in R_s and x_u , y_u and z_u are elements in R_u [43].

The change in range between two epochs can further be derived as in equation (5.7) as a consequence of that the receiver position can be expressed as $R_u(t_j) = R_u(t_{j-1}) + \Delta R_u$

$$\begin{aligned}
 \Delta d &= [[e(t_j) \cdot R_s(t_j)] - [e(t_{j-1}) \cdot R_s(t_{j-1})]] - \\
 & [[e(t_j) \cdot R_u(t_{j-1})] - [e(t_{j-1}) \cdot R_u(t_{j-1})] + e(t_j) \cdot \Delta R_u]
 \end{aligned} \tag{5.7}$$

And this can be further simplified as in equation (5.8) below

$$\Delta d = \Delta D - \Delta g - [e(t_j) \cdot \Delta R_u] \tag{5.8}$$

where

$$\Delta g = [e(t_j) \cdot R_u(t_{j-1})] - [e(t_{j-1}) \cdot R_u(t_{j-1})] \tag{5.9}$$

and

$$\Delta D = [e(t_j) \cdot R_s(t_j)] - [e(t_{j-1}) \cdot R_s(t_{j-1})] \tag{5.10}$$

The Δg term accounts for the satellite-receiver geometry change caused by the fact that the LOS-vector changes orientation and the ΔD term corresponds to the change in range and is proportional to the Doppler frequency shift relative the motion of the satellite-user. Subsequently the formula for TDCP with corrections and compensation for the ΔD and Δg terms will be according to equation 5.11 below :

$$\Delta L_{corrected} = \Delta L - \Delta D + \Delta g = -[e(t_j) \cdot \Delta R_u] + c\Delta t_R + \Delta \nu \tag{5.11}$$

This has to be solved for every satellite available for the receiver and the final value of ΔR_u and $c\Delta t_R$ can be computed by using a weighted least square solution where the least square estimation is weighted dependent on the elevation of the satellites. The weighted least square solution can be seen below in equation 5.12 [42].

$$\underline{x} = (H^T \cdot W \cdot H)^{-1} \cdot H^T \cdot W \cdot \underline{y} \tag{5.12}$$

Where H is a matrix containing the LOS unit vectors in each dimension and for each satellite n for each epoch, filled with ones to enable clock error estimation.

$$H = \begin{bmatrix} e(t_j)_1^x & e(t_j)_1^y & e(t_j)_1^z & 1 \\ e(t_j)_2^x & e(t_j)_2^y & e(t_j)_2^z & 1 \\ \vdots & \vdots & \vdots & \vdots \\ e(t_j)_n^x & e(t_j)_n^y & e(t_j)_n^z & 1 \end{bmatrix}$$

\underline{y} contains the corrected TDCP measurements $\Delta L_{corrected}$ for each satellite n such as

$$\underline{y} = \begin{bmatrix} \Delta L_{corrected,1} \\ \Delta L_{corrected,2} \\ \vdots \\ \Delta L_{corrected,n} \end{bmatrix}$$

The weight matrix W is a diagonal matrix containing elements corresponding to the squared sine of the satellite elevation angle ϵ_n .

$$W = \begin{bmatrix} \sin^2(\epsilon_1) & 0 & \dots & 0 \\ 0 & \sin^2(\epsilon_2) & \dots & 0 \\ \vdots & \vdots & \ddots & \vdots \\ 0 & 0 & \dots & \sin^2(\epsilon_n) \end{bmatrix}$$

The weight matrix ensures that the received signals from satellites affected with multipath etc matter less when estimating the position. This is done by checking the elevation angle of each satellite seen by the receiver. If the elevation angle is very low, the weight of this measurement will be small compared to those measurements from satellites of higher elevation.

The result will be in vector form, and contains four solutions in a column vector. The vector displays the receiver position \underline{R}_P in terms of x, y, z position and time error.

$$\underline{R}_P = \langle \Delta R_u^x, \Delta R_u^y, \Delta R_u^z, \Delta t_R \rangle$$

Since the vector \underline{x} should contain four solutions, at least four equations have to be solved for each epoch. One satellite measurement can provide one solution for each equation, which means that at least four satellites are needed to get a three dimensional solution of position and time. Also, since TDCP uses differencing between epochs, these four satellite measurements have to be available during epoch t_{j-1} as well as the next epoch t_j . It is therefore necessary that as many satellites as possible are visible and transmit their data for the TDCP algorithm to work as intended.

After this has been solved the average user velocity can be calculated according to equation (5.13) below.

$$\langle \underline{V} \rangle = \frac{\Delta R_u}{t_j - t_{j-1}} \quad (5.13)$$

where the vector ΔR_u is a version of \underline{x} that contains the position of the user as below.

$$\underline{\Delta R_u} = \langle \Delta R_u^x, \Delta R_u^y, \Delta R_u^z \rangle$$

A flowchart of the main process for TDCP is displayed in figure 5.2 below.

The ionospheric and tropospheric models can be neglected when using TDCP since differencing is done between consecutive epochs. The time of data collecting during a SAR run is also small enough for the ionosphere and troposphere to not change drastically in their characteristic, which further makes neglecting the models viable.

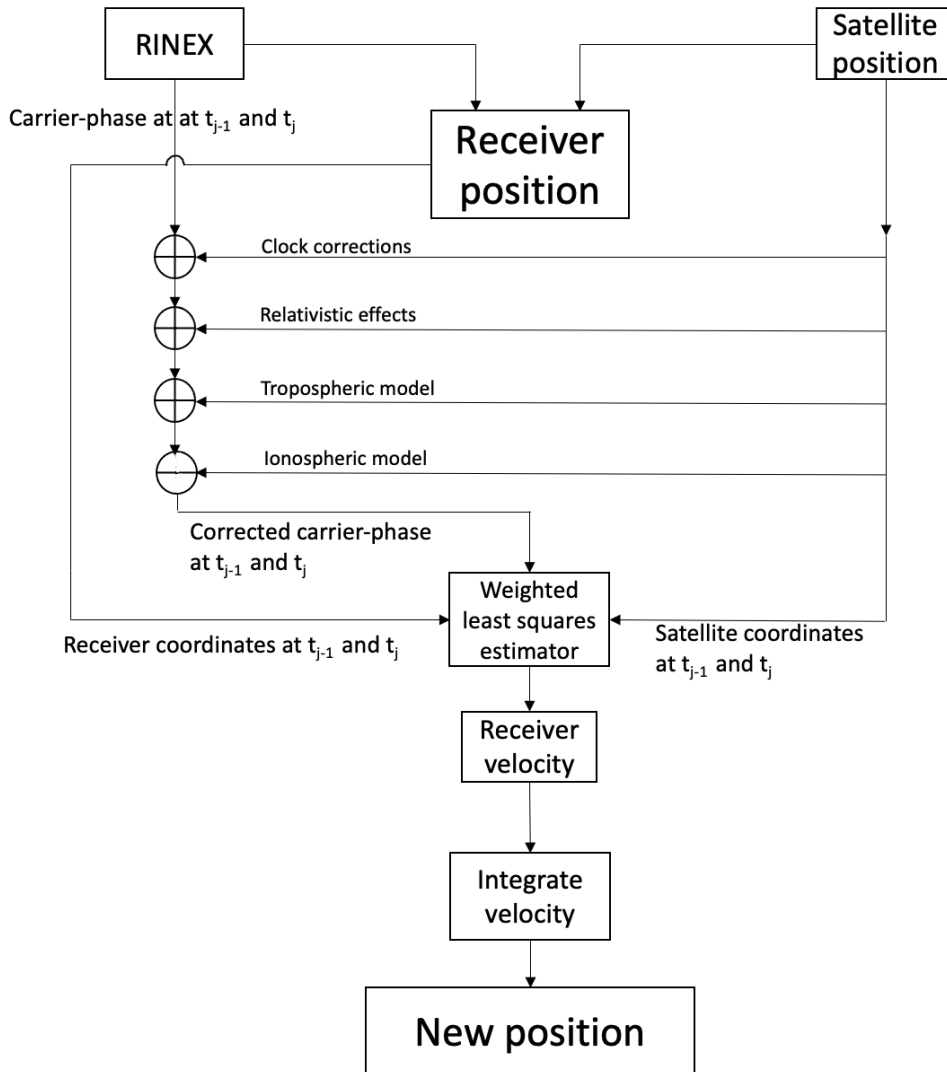


Figure 5.2: TDCP flow chart. Source: Modified from [42]

5.4 Referenced TDCP

There are other ways to calculate a relative position using time differenced carrier phase measurements than the one previously mentioned, where the velocity and

position is based on the relative change between two consecutive epochs. It is also possible to include a reference measurement to compare the new position to, instead of getting the relative change in carrier phase measurements as in equation (5.3) the change in position relative to a reference epoch will instead be as in equation (5.14).

$$\Delta d = d(t_j) - d(t_{ref}) \quad (5.14)$$

The reference epoch t_{ref} is chosen by the user at an epoch where the receiver position is known, preferably the first epoch where the position can be acquired with a code solution. If the position of the reference epoch is very well known, the resulting errors on subsequent epochs will be very small [43]. The referenced TDCP method has the potential to mitigate the position drift that is present in regular TDCP, but with the drawback of being more sensitive to start position errors. When a cycle slip appears for referenced TDCP it is also necessary to change the reference epoch to an epoch after the cycle slip appeared. This sub method of TDCP could be applied for SAR position estimation, but would need evaluation of how an error in the starting position would affect the performance.

5.5 Error sources and mitigation for TDCP

One major problem when using TDCP is the potential disruption which can be caused by cycle slips. This subsequently affects the phase ambiguity of the carrier, and causes a brief disconnection between the receiver and the satellite. Depending on the length of this cycle slip and the sampling frequency it affects the precision differently. If e.g L1 is used which has a wavelength of around 19 cm and the error is 5 cycles at a sampling interval of 1s the resulting error in precision of the velocity estimation will be around 100 cm/s.

In order to mitigate the problem with cycle slips it is necessary to implement different algorithms which have the capacity to detect and repair the slip. The complexity of such an algorithm increases when the receiver and signal experience more ionospheric impact or when the system is connected to satellites with low elevation angles. There are generally two types of algorithms that can eliminate the cycle slip effects. One type of algorithm that focuses solely on carrier phase measurement and one type that combines both carrier phase and code measurements. The difference is that the method with both carrier phase and code measurements eliminates geometric effects as well as dispersive effects e.g from the ionosphere but the first mentioned algorithm only eliminates geometric effects. There are different applications for each algorithm, since the first mentioned algorithm provides a very accurate test signal with low influence from multipath but gets more influenced by ionosphere and vice versa for the other algorithm [44].

5.5.1 Cycle slip detection

Depending on what signals that are available in the raw RINEX data, different cycle slip detection algorithms can be implemented. These cycle slip algorithms

are implemented on the raw RINEX data which makes it possible to discard certain satellites that might give erroneous measurements, even before the least square filter in the TDCP method.

One way of finding cycle slips is by comparing the difference between code and phase measurements over two consecutive. If the change in phase over two epochs is much different compared to the change in pseudorange from the code measurements there might have appeared a cycle slip in the raw data. By creating differenced code ΔC and differenced phase ΔL measurements over two epochs as below, these can be compared. If the two differences are larger than a certain threshold T , it indicates a cycle slip according to equation (5.15).

$$\Delta L - \Delta C \geq T \quad (5.15)$$

where

$$\begin{aligned} \Delta C &= C(t_j) - C(t_{j-1}) \\ \Delta L &= L(t_j) - L(t_{j-1}) \end{aligned}$$

Where the carrier phase measurements L are comprised of the observed carrier phases L_{obs} multiplied by their corresponding wavelength λ_L as such $L = L_{obs}\lambda_L$. An illustration of the ΔC and ΔL terms as well as a cycle slip can be seen in figure 5.3.

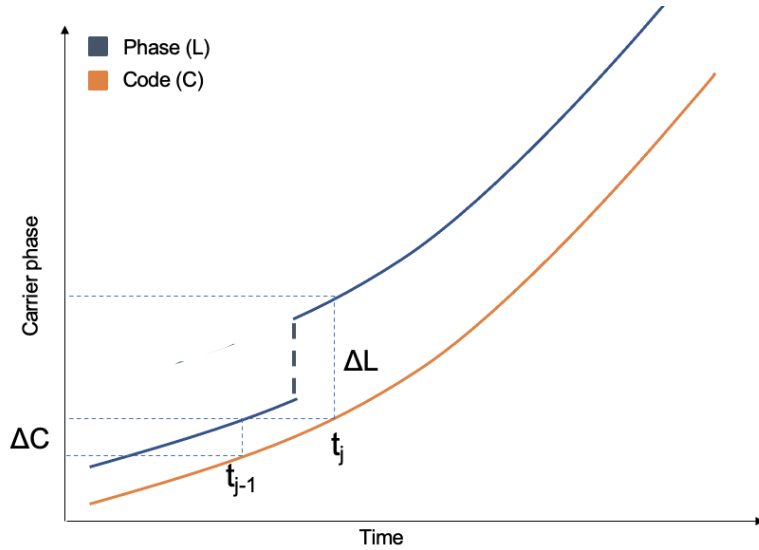


Figure 5.3: Code and phase differences ΔC and ΔL on data with a large cycle slip

There are also other ways of finding cycle slips. When having access to both L1 and L2 it is possible to also detect cycle slips in a similar way to using code and phase as above. The carrier phase measurements have a much higher resilience against multipath compared to the code observations and can thus be used together for higher chances to find cycle slips. Similarly to the code and phase detection, a

difference in the carrier phases are created as below.

$$\begin{aligned}\Delta L_1 &= L_1(t_j) - L_1(t_{j-1}) \\ \Delta L_2 &= L_2(t_j) - L_2(t_{j-1})\end{aligned}$$

With these differences the threshold for cycle slips can be established as

$$|\Delta L_1 - \Delta L_2| > f \cdot \sigma_{comb} \quad (5.16)$$

where f is an integer confidence factor that decides how tight a slip has to be before it is caught and σ_{comb} is a combination of wavelengths and thermal noise of the carrier phases.

$$\sigma_{comb} = \sqrt{2} \cdot \sqrt{\lambda_{L1}^2 + \lambda_{L2}^2} \cdot \sigma_{L1,cycle} \quad (5.17)$$

where $\sigma_{L1,cycle} = \sigma_{L2,cycle}$ is the standard deviation of thermal noise of the carrier phase signals. The standard deviation of around 1 mm is assumed to be the same for L1 and L2 [45].

These two cycle slip detectors are combined to ensure that most of the cycle slips are found. Since, using these methods, the cycle slips are found in the raw RINEX data it is possible to remove the satellites responsible for the cycle slips before calculating the delta positions in the least squares solution in the TDCP method. This gives a great robustness against erroneous measurements in the final velocity.

5.5.2 Outlier detection

Another appearing problem when using the method is due to the presence of irregular outliers in the raw RINEX observation data. An outlier is a measurement that is incorrect, with a value that is unreasonable compared to similar data. Outliers will effect the precision of the method. These outliers can be removed with an outlier detection filter [46].

An example of this behavior can be seen in figure 5.4 below. In the top figure the velocity of the receiver is shown. It is clear that the majority of the velocity measurements are around 0 m/s. There is a simple filter in place that removes all velocities over a certain threshold $T = |v| > 0.03$ m/s. This very simple filter is possible to use since it is known that the receiver is stationary. The bottom image contains the position in x and y calculated by integrating over the velocities. When the outliers are present there are sometimes in the order of ± 1 m/s. This makes the TDCP algorithm think that the receiver has moved this distance over that epoch and this will create shifts in positions which are recognizable in the blue points.

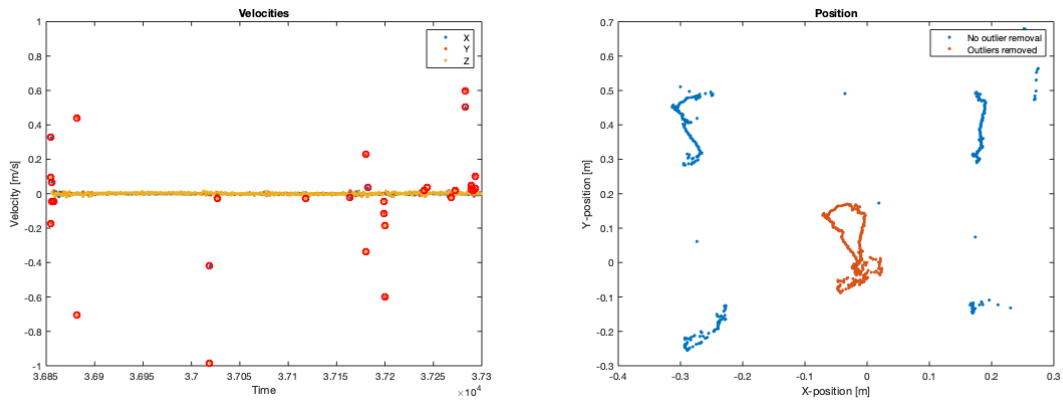


Figure 5.4: Outliers in measured velocity for stationary receiver. The blue points are positions when integrating over the velocities with the outliers, and the orange points are positions calculated when the outliers in the velocities are removed. The outliers that are removed are highlighted with red circles.

In the case of SAR processing, the synthetic aperture will be formed by flying in a relatively straight line over a time period. This means that the velocity of the receiver should be relatively constant. One way to find possible outliers in this case is by using a so called exponential weighted moving average (EWMA) filter. The EWMA is a version of the regular moving average (MA) filter. A regular MA filter uses a specified number of data points, called window, and calculates the mean of these. This can be done over all points and thus, the mean will move with the the data points. This filter can be described simply with a sum as in equation (5.18).

$$\frac{1}{k} \sum_{i=n-k+1}^n p_i \quad (5.18)$$

where k is the number of data points that are viewed (window size) and n is the index for determining which epoch the filter is applied to [47].

The more advanced version of the MA is the weighted moving average (WMA) filter. The common approach for constructing such a filter is to put more weight on data points surrounding the examined point, and less weight on points that are further back in the data set. The decay of the weight on older data points can be applied in multiple ways. The exponential moving average (EWMA) filter decreases the weight of each point exponentially. This filter is especially valuable if the outliers are sparse and appear infrequently. The exponential decay rate for the EWMA is chosen via trial and error for this particular application[48].

An illustration of how the filter looks like on velocity data can be seen in figure 5.5. In the figure the large dots represent data points that the filter recognizes as outliers and the dotted lines represent the error bounds for the outliers that decay exponentially.

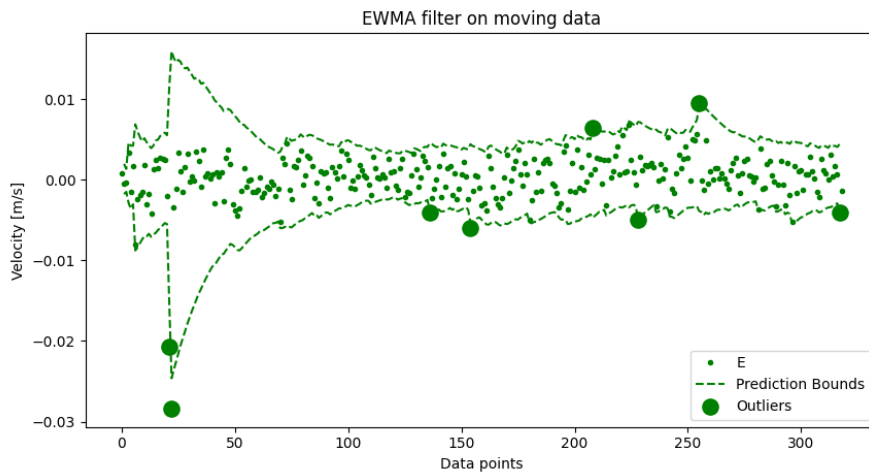


Figure 5.5: Exponentially weighted moving average (EWMA) filter on velocity data for stationary receiver.

6

Performance of TDCP

This section will include all testing and results for the TDCP method. The tests are done to see how well the TDCP method copes with cycle slips, outliers and positional drift. The TDCP method will also be compared to highly accurate RTK solutions to evaluate the positional drift over time. Positional drift with different offsets in starting position will also be examined to see how robust the TDCP method is against errors in starting position. The tests are divided into two different parts, self designed tests, and tests done with collected data from preflown CARABAS-3 flights.

6.1 TDCP and outliers

In order to evaluate the TDCP method some initial tests are designed. These tests are designed in such a way that the expected positional drift over time of the receiver will be clear. The tests are also a way of evaluating how much of an impact the cycle slips have on the final results for velocity and position. The receivers used for the testing are a pair of Ublox c099-f9p where one receiver configured as rover and one as base. Connected to each receiver is a simple Tallysman Wireless 33-2412-07 antenna which only supports the L1 signal on GPS. These receivers are connected to a computer with the software program U-center that manages and stores the observed data from the receiver. The observed data is converted into the right format using the program RTKLIB. The receivers are also tested with a Ublox ANN-MB-00-00 antenna, which supports more GNSS and has a higher bandwidth that enables receiving more GPS signals

One test is constructed to see how much impact cycle slips and velocity outliers have on the final position. This test is done by placing one receiver with antenna on a still and level surface for a couple of minutes. The expected result is that the velocity in all directions east, north and up (ENU) should be close to zero since the receiver is not moving. Corrections in the form of relativistic corrections and clock corrections are applied to the signals when using the TDCP method, no form of cycle slip detection on raw data is used.

In figure 6.1 three plots from the test can be seen. The top left plot shows the velocities that are created from the TDCP method. As mentioned, the velocities

should be close to zero during the duration of the test. It is clear however that there are times where the velocities in some direction seems to 'jump' up or down for one measurement and then return to the expected positions. These outliers are most likely due cycle slips directly from the receiver. The outliers can also be due to other effects upon the reception of the satellite signals such as multipath or other delays. These velocities are then turned in to positions by integration and are seen in blue in the bottom image of figure 6.1. When a velocity outlier occurs there is a large change in position.

To reduce the effects of the outliers the very obvious outliers can be removed. In this test the outliers are removed by deleting any measurements that are clearly too high in velocity, this leaves the measurement points around zero velocity. The outliers that are removed can be seen in to top right plot of figure 6.1. The red rings indicate where outliers have been removed, the rest of the data points are kept the same as before. When creating a position from these velocities there is a significant improvement in positional change and drift. The position created from the velocities with outliers removed can be seen in orange in the bottom plot of the figure. The positions are much more centered around the center point which is to be expected.

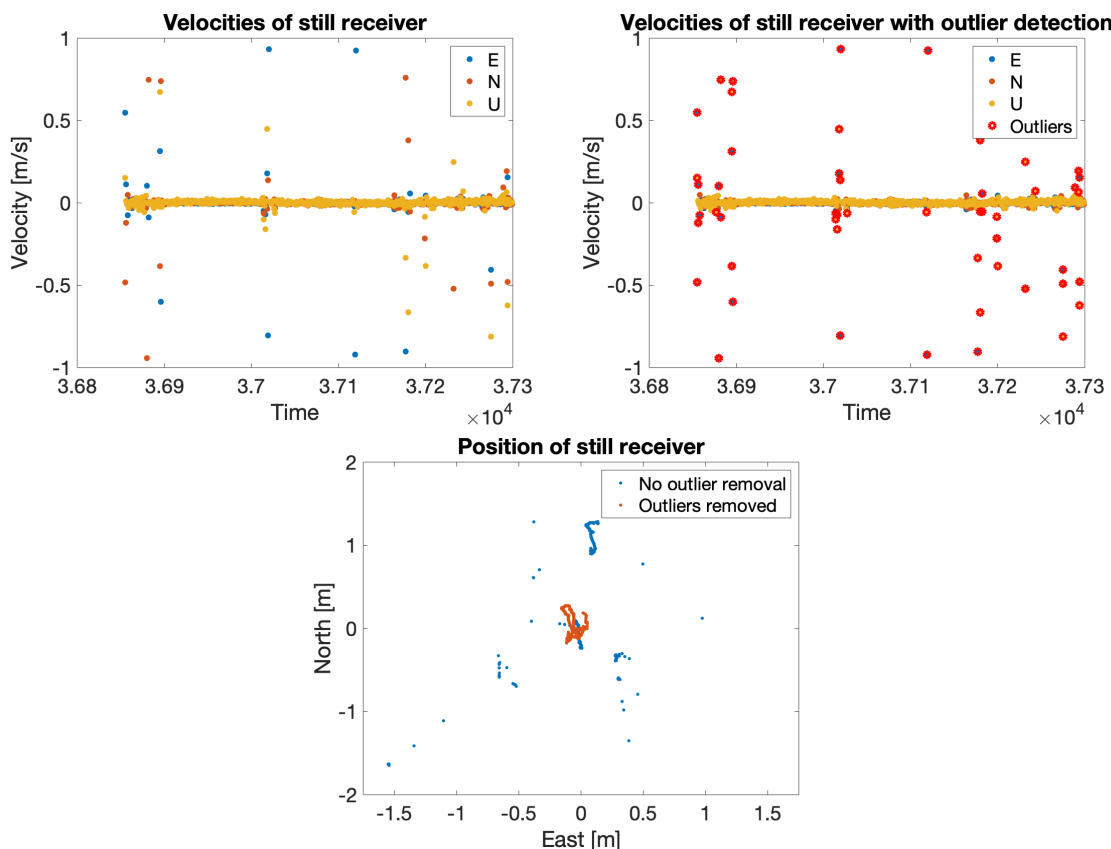


Figure 6.1: Impact of cycle slips on measurement data: Velocities on still/stationary receiver. Top left: Velocities in ENU on still receiver, shows many cycle slips. Top right: Velocities in ENU on still receiver with obvious outliers removed. Bottom center: Positional (EN) difference from velocities with outliers (blue) and with outliers removed (orange).

This amount of outliers in the data is not a normal occurrence for the tests. The receiver with the Tallysman antenna is in this case largely affected by multipath which creates many of the outliers. This is most likely due to the receiver being placed close to other devices such as a computer which might block some of the signals and reflect others. An ideal placement for the equipment in this test is to use a longer wire and place the antenna further away from the computer and receiver. The antenna should also be elevated. This reduces the risk for multipath and blockage.

6.2 TDCP and positional drift

It is of importance to see how much the method is affected by cycle slips, different velocities and outliers. A test is conducted by moving a GNSS receiver on a board over a straight line, for about a minute of data collecting. An illustration of the test can be seen in figure 6.2.

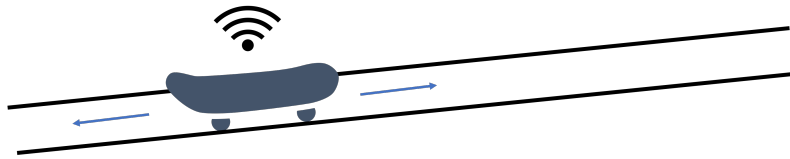


Figure 6.2: Test setup, receiver placed on board. Moved along a straight line

A receiver is placed at a stationary position on top of a board, the board is then moved along a straight track. The track is marked with start and stop points. When the board comes to one of these points the board with the receiver is moved in the opposite direction, this is done multiple times during two minutes. The accuracy of the start/stop is estimated to be within ± 1 cm for east and north directions due to human error when changing directions of the board movement. The vertical error is assumed to be much smaller since the receiver is moved along a relatively flat surface. This test should show if there is a clear positional drift from the TDCP method if the change in position after returning to the start position is more than the estimated error of ± 1 cm.

In figure 6.3 the positional results in east versus north (EN) positions can be seen. The plot indicates that the receiver was moved in a straight line with the data points around the start and stop points tightly clustered. This shows that the positional drift for the rather low velocity of the board during two minutes is not very large, in the order of centimeter level. Instead of looking at the position in east versus north it is more clear to see how the position in ENU changes with respect to time. This is seen in figure 6.4.

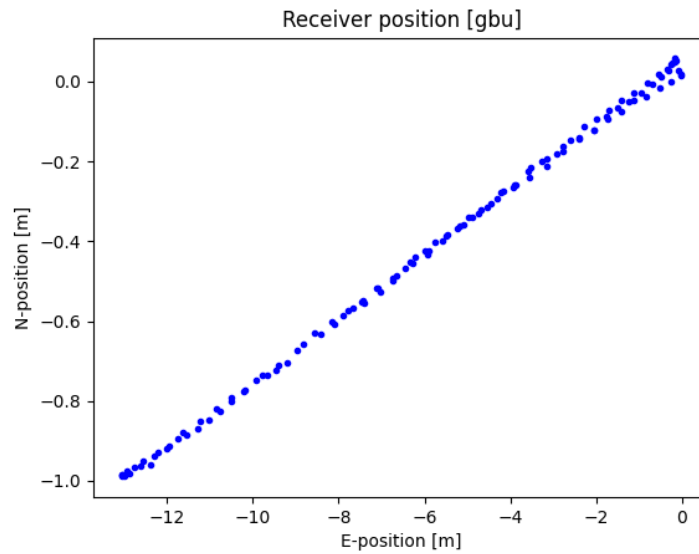


Figure 6.3: Position result (EN) of straight line test, The plot shows the receiver moving towards the end of the track and then returning to the starting position.

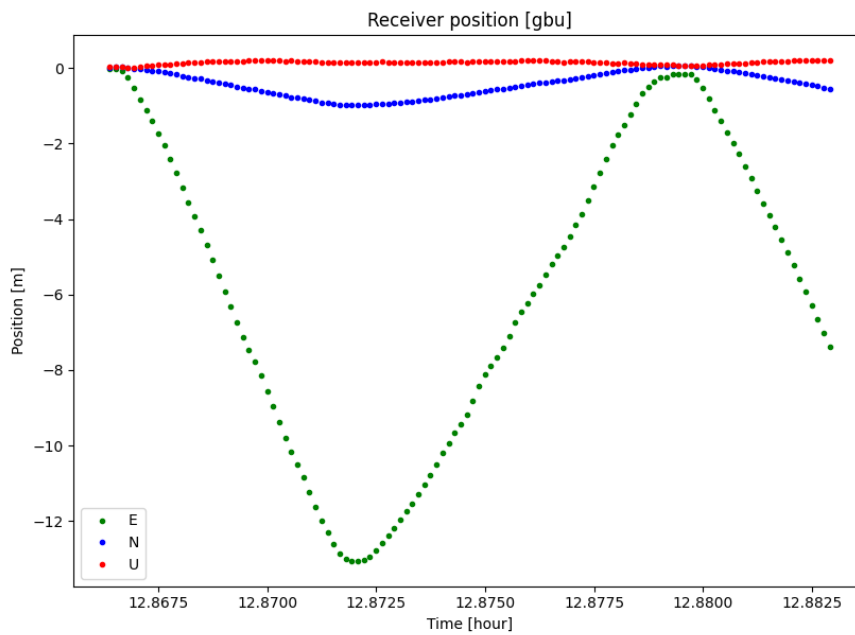


Figure 6.4: 3D Receiver position as a function of time for straight line test.

In figure 6.4 the 3D positional error after returning to the start position is about 110 mm. This shows that the positional drift is close to the goal of a drift less than 100 mm after 60 seconds even for a relatively basic receiver with a preliminary set up using a board to move the receiver.

6.3 TDCP method using different sp3-files

As mentioned previously the satellite positions in orbit are a key part of getting a reliable solution. When calculating the positions of satellites using their respective navigation messages the position is based on equations that are an estimation of the actual position. These equations do not impose much periodical behaviour in the satellite orbits. When using the orbital solutions from sp3-files with the TDCP method a clear periodic tendency is visible in the orbits, with a periodic equal to the satellite position update rate appears in the sp3-file. This rate is usually five or 15 minutes. This in turn affects the velocity of the receiver with a similar behaviour.

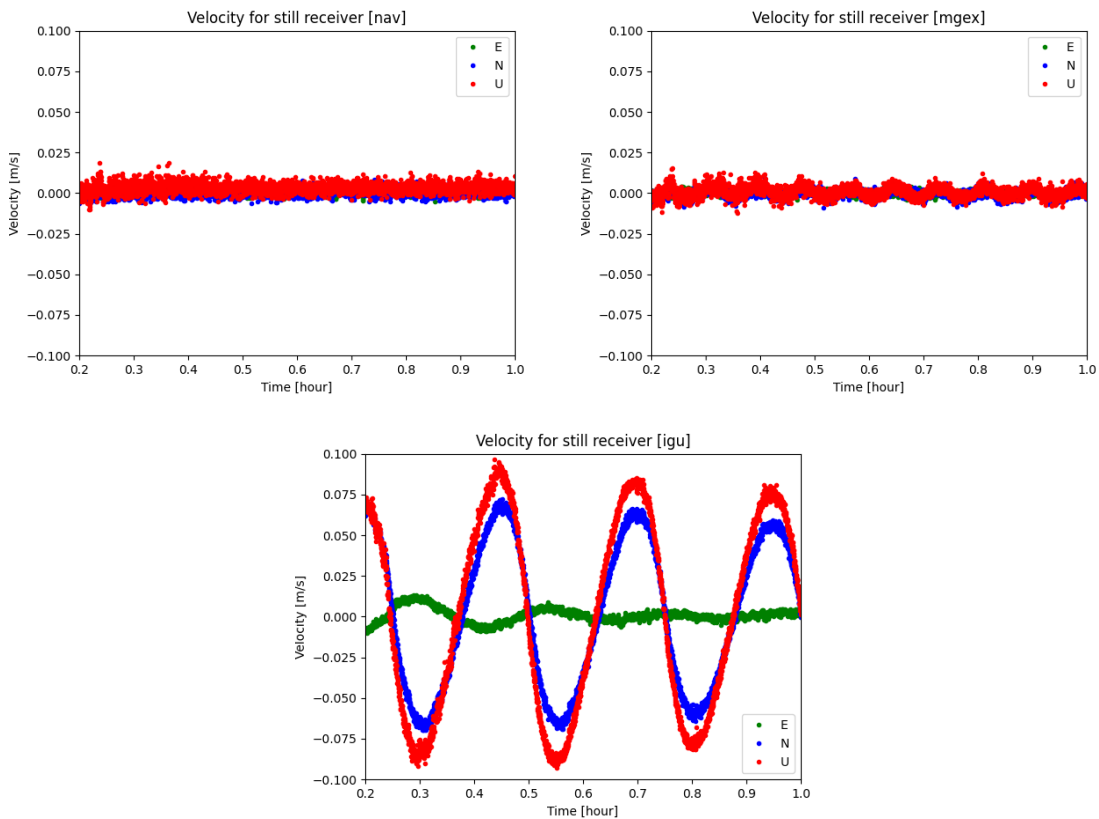


Figure 6.5: TDCP velocity in ENU for stationary receiver during one hour using navigation message (top left), using an sp3-file with five minute update rate (top right) and using an sp3-file with 15 minute update rate (bottom center).

By using a still receiver over multiple periods this behaviour is very clear. The plots in figure 6.5 show the differences in receiver velocity in ENU when using the same processing with the same RINEX data but with different ways of getting the satellite positions. The top left plot shows the velocities in ENU for the still receiver using the navigation message during 1 hour. The velocities are close to 0 m/s in all cardinal directions which is to be expected. The top right plot shows the velocity for the same receiver when using an sp3-file with a five minute update rate. When the velocity is plotted for close to an hour the periodic tendencies in velocity is

quite clear. The bottom center plot contains the velocities of the same receiver but when using sp3-files with an update rate of 15 minutes. Here the periodic tendencies completely change the velocities in all directions by such a large amount that it is not reasonable to use these types of files.

To further show the differences between the satellite positions from using the navigation message and different sp3-files the difference between satellite orbits are shown in figure 6.6. The left part of the figure, a sp3-file (from gbm) with five minute update rate is plotted against the position from the navigation message. And in the right part of the figure the difference between a sp3-file with 15 minute update rate (from igu) and the navigation message is displayed. Both are displayed for a time period of one slightly over one hour. The same conclusions are made with these plots. The sp3-file with a 15 minute update rate is not applicable for this method since the change in position between each peak is of too large magnitude. For short SAR runs the five minute files can be used since even if there is a periodic tendency, the change in position between the peaks are relatively low, in the order of decimeter level.

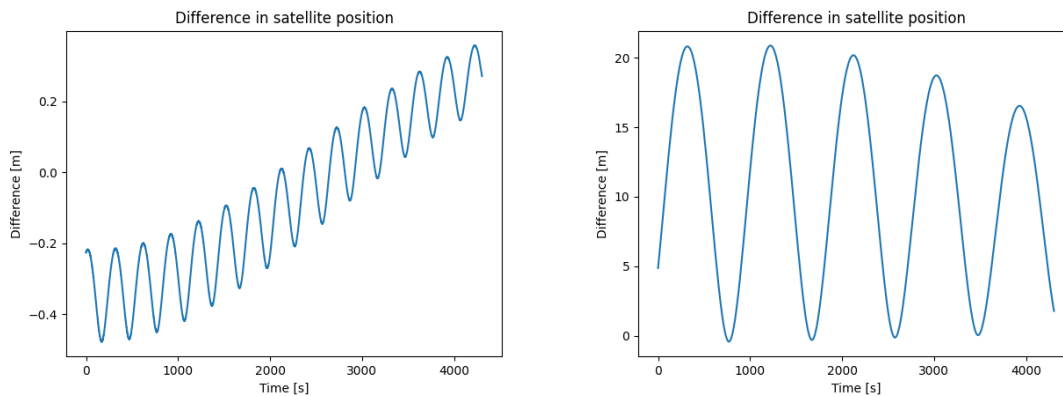


Figure 6.6: Difference in satellite positions over one hour between navigation message and sp3-files. Left: five minute sp3-file (gbm) compared to navigation message. Right: 15 minute sp3-file (igu) compared to navigation message

This behaviour is very similar to that of Runge’s phenomenon. The phenomenon is an oscillation that can appear when using high order polynomial interpolation for points spaced at roughly equal distance, such as the case with satellite orbits. This should however not be the case since cubic spline interpolation is used to interpolate the satellite positions and cubic spline interpolation is inherently robust against Runge’s phenomenon [49].

6.4 TDCP versus RTK

Lastly, for the tests done with the helicopter two Antcom 53G1215A-XT1 GNSS antennas are used with the GNSS receiver Javad Delta Duo G2D-4. The data from these measurements are already processed into RINEX format so processing in

RTKLIB is unnecessary, except for checking the skyplot of the satellites to get the DOP values.

The method used for obtaining a position of a GNSS receiver for a CARABAS-3 flight today is by using RTK. In order to evaluate the performance of TDCP, the positions from TDCP can be compared to the positions from the RTK solutions. The CARABAS-3 flights commonly consist of a longer flight with multiple straight flight lines, referred to as "SAR runs". The purpose of these runs is to fly in a straight line in some direction at a constant velocity for between 30 and 100 seconds. The straight lines are seen as the aperture of the SAR. The processing time for SAR is reduced when the receiver position is very close to the true aperture. It is therefore important to have a very good position.

An example of how these SAR runs looks like can be seen in figure 6.7. The flight path is the RTK solution of the real flight path and should therefore be close to the real flight path. Highlighted in blue are the straight line SAR runs with relatively constant velocity.

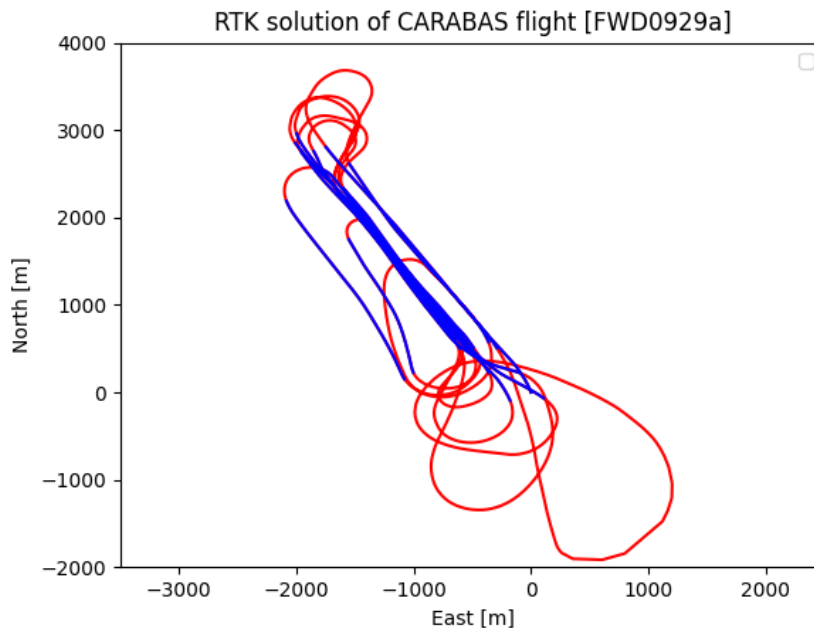


Figure 6.7: Part of CARABAS-3 flight with RTK solution in RED and straight SAR runs highlighted in blue.

Since TDCP needs two epochs of approximate starting position to get started, when comparing TDCP with the RTK solutions these starting positions are taken directly from the RTK solution. The impact of incorrect starting positions will be investigated further later on. The receiver sampling frequency is set to 10 Hz in all tests where CARABAS-3 data is used. The velocity from the TDCP solution for an example SAR run can be seen in figure 6.8. The figure also contains the error bounds and detected outliers from the EWMA filter. As expected the velocity remains rel-

actively constant without very large fluctuations in the data set, which is ideal for the EWMA filter.

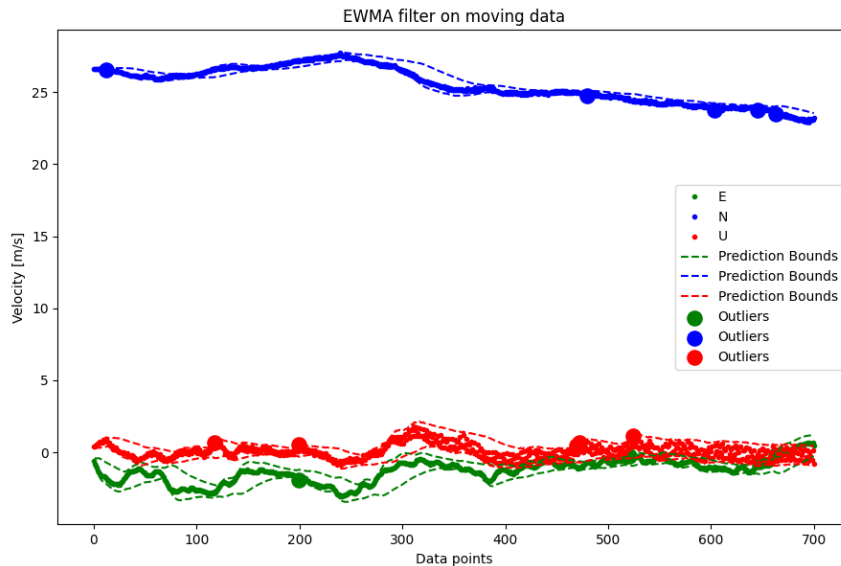


Figure 6.8: Velocity for SAR run with added EWMA outlier detection for east (green), north (blue) and up (red).

6.5 Analysis of SAR runs

In this section the results from four different CARABAS flights containing multiple SAR-runs in each flight will be analyzed. For context these runs are named FWD0929a, FWD0929b, FWD1002c and FWD0611a. The first three files are recorded in 2016 and the FWD0611a is recorded in 2014. The main reason for analyzing the runs is to see how much positional drift the TDCP method has compared to the RTK solutions. The data from the SAR runs can be split up in to smaller pieces with set starting positions and run time. By splitting the long runs in to smaller runs the statistics of the positional drift in all directions may be evaluated. Because the runs are split the number of data sets increase by a large amount and the statistical data will be more substantial. For example, a regular SAR run that is 100 seconds long can be split in to 100 different runs that are 1 second long this increases the number of data points by a factor 100. A visualization of this is seen in figure 6.9. The total number of runs that is processed for the final plots can be seen in appendix A.

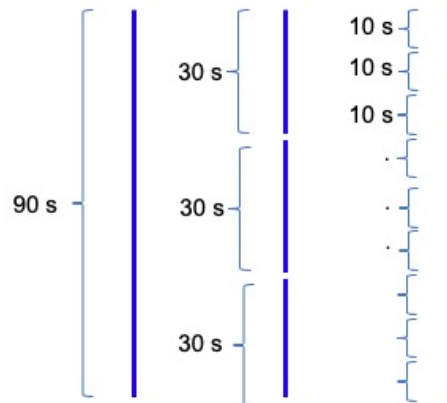


Figure 6.9: One SAR run (90 s) is split in to multiple shorter runs.

To visualize the amount of positional drift from TDCP compared to RTK the drift is measured every 2 seconds starting from 1 second and ending at 81 seconds. This means that every other second there is an amount of data points that will have somewhat different drifts depending on how good the SAR run being evaluated is. From these data points the median together with the 5th, 25th, 75th and 95th percentiles are extracted and plotted. Since the satellite positions from the 15 minute sp3-files are so bad, these files are not included in the plotting of drifts. The drift with percentiles can be seen in figures 6.10 - 6.12 where the left plots are the drift using navigation message for satellite positions and the right plots are created using sp3-files with 5 minute update rate.

The plots show that the median drift in all directions (east north and up) is below 100 mm after 60 seconds. For the drift in east direction in figure 6.10 the 75th percentile drift equates to around 150 mm while the 95th percentile equates to around 240 mm after 60 seconds. This change in drift for the higher percentiles is even more prominent in the north direction in figure 6.11 where the higher percentiles have a much larger amount of drift. The 75th percentile in north drifts around 250 mm and the 95th percentile around 450 mm after 60 seconds.

The positional drift in the up direction is expected to be larger than the others due to satellite geometry. From the figures below it is possible to see that the positional drift when using the navigation messages from the satellites is performing better compared to the drift when sp3-files are used. This is expected since the method is relying on relative positioning, which is an advantage when using navigation messages, since they yield unswerving satellite orbits but with a constant bias. This constant bias is not relevant when using relative position which results in that the navigation messages are better for the application.

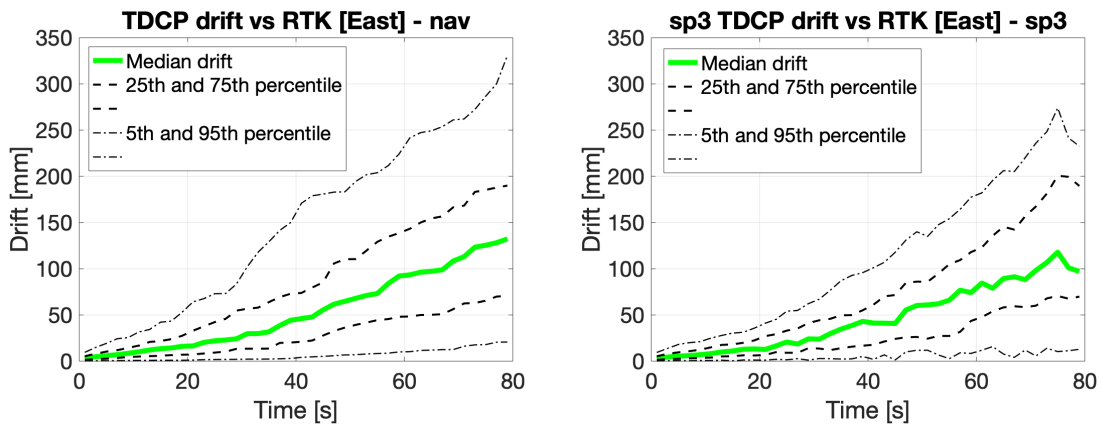


Figure 6.10: East median drift. Created using navigation message (left) for satellite positions and compared to drift with sp3 (right)

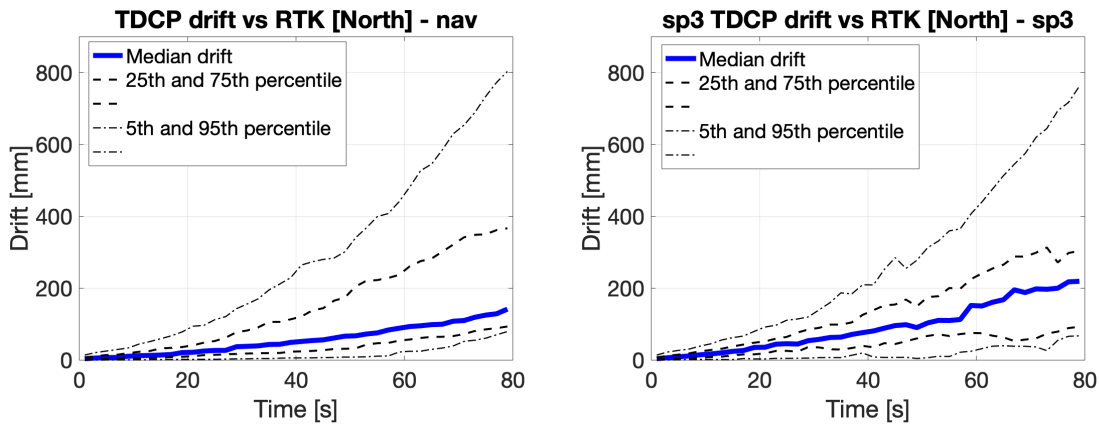


Figure 6.11: North median drift. Created using navigation message for satellite positions and compared to drift with sp3 (right)

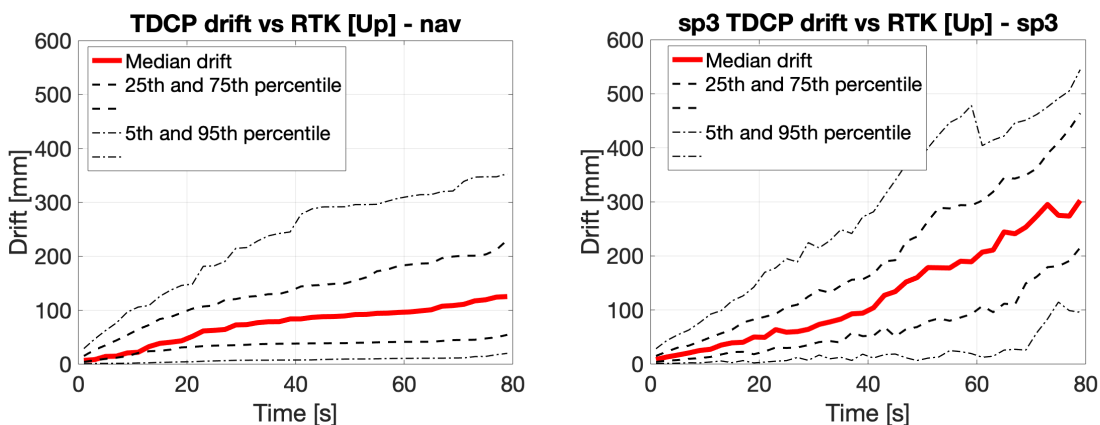


Figure 6.12: Up median drift. Created using navigation message for satellite positions and compared to drift with sp3 (right)

When the median drift from east north and up are combined to a 3D positional

drift it is possible to see how much total drift the TDCP method has compared to RTK. This drift is seen in figure 6.13. The plot contains one line for the 3D median drift using navigation message, one line for the 3D median drift using sp3-files and one line at 100 mm which is the wanted positional drift. The plot shows that the 3D drift is higher than 100 mm after 60 seconds for both satellite positions. For the navigation message the drift is closer to 160 mm after 60 seconds. This is not really a problem since the goal of 100 mm after 60 seconds is a very restraining goal. As will be seen later when using CARABAS-3 for SAR images this accuracy is good enough to get the wanted SAR images.

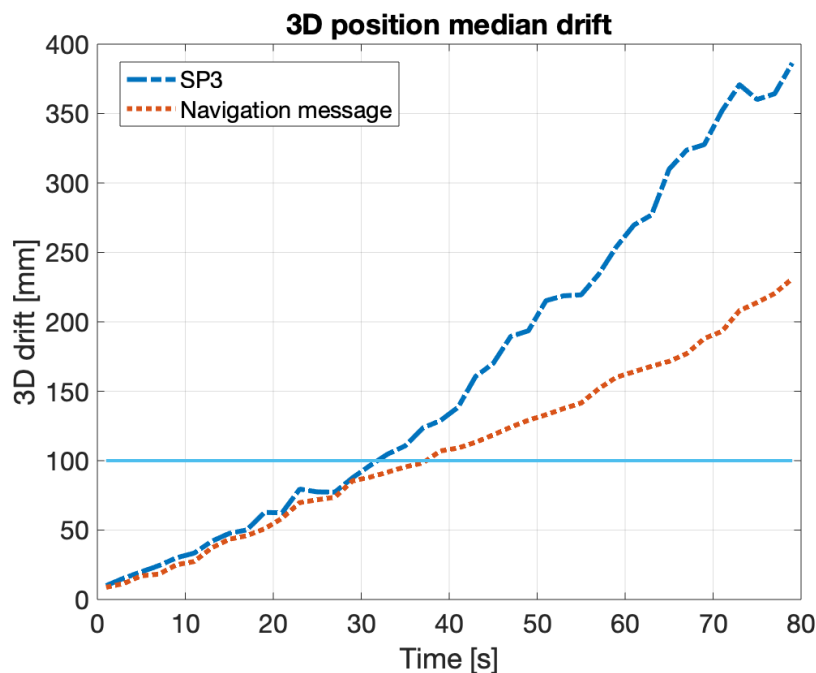


Figure 6.13: 3D positional drift for TDCP using satellite navigation message and sp3-files with a line at 100 mm

6.6 Possible errors from SAR runs

There are some runs that affect the drift in the figures above substantially, for example the data from the run titled FWD0929b has a large amount of drift in the north direction, this can be seen in figure 6.14. Since the data points are taken from a single file there are not as many data points that are analyzed which can skew the drift in some direction. However, for those data points that are available the drift is of large magnitude after a time period. Even the 5th and 25th percentiles of the median have large drift. This means that almost all of the runs drift a large amount in that certain direction. The drift in other directions from this file is of smaller magnitude, around 50 mm for both east and up. The drifts from all the individual flights processed separately can be seen in the appendix B along with the flight path and DOP for the runs.

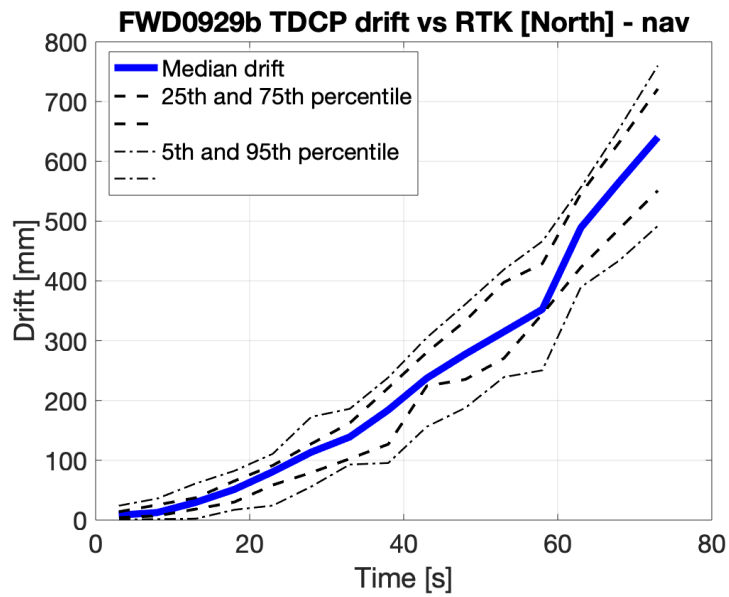


Figure 6.14: Drift in the north direction

The reason for the large drift in the north direction might be due to this being the only file of the four processed with a flight path that flies in a very clear east direction. By analyzing the drift for the runs in appendix B that have a very eastern flight path (FWD0604a and FWD0929b) it can be seen that both of these runs have large drifts in the north direction. This can however be a fortuity and not depend on the flight direction. In figure 6.15 below flight FWD0929b is displayed.

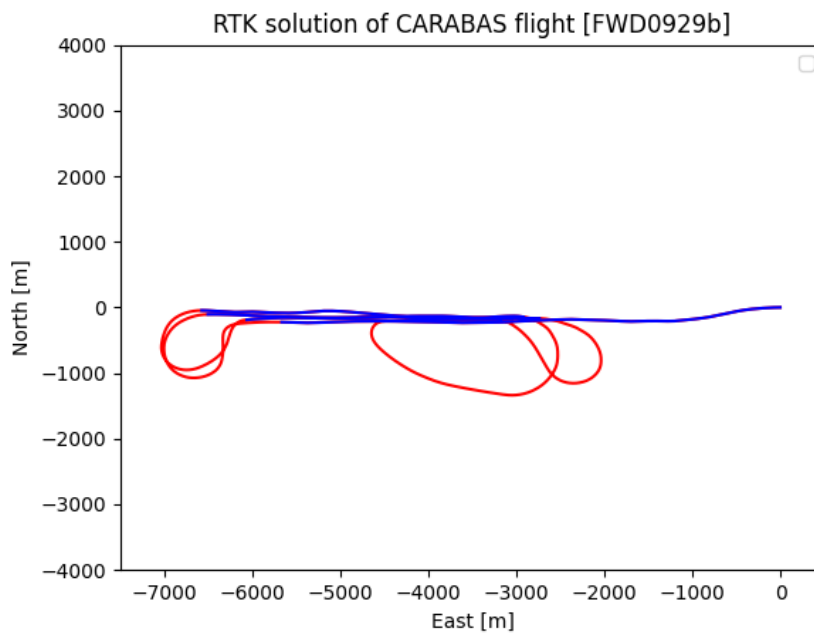


Figure 6.15: CARABAS flight with SAR runs highlighted in blue for FWD0929b, the SAR runs are flown in an eastern direction with very little difference in north.

The relation with large drift in the north direction being worse when flying east should also be apparent if a diagonal run is rotated to run in the same eastern direction. This does however not give the same results. When rotating the diagonal runs not much changes in the ways of drift in either eastern or northern direction. It is therefore impossible to pinpoint the reason for the large drift in the north direction without using much more data from many more flights in different directions.

Another reason for this flight giving much drift could be due to bad satellite positioning and high DOP. In figures 6.16 below the dilution of precision (DOP) from the CARABAS-3 flight FWD0929b can be seen. The number of satellites available are > 10 in each flight and the geometry of the satellite constellation indicates a low DOP which results in a better chance of getting a good position from the measurements. However, the sky-plot of FWD0929b suggests that the DOP might be higher during this flight since there is few satellites available in the southeast direction. The GPS satellites are displayed with the azimuth angle at the outer circle and the elevation angle at the vertical axis.

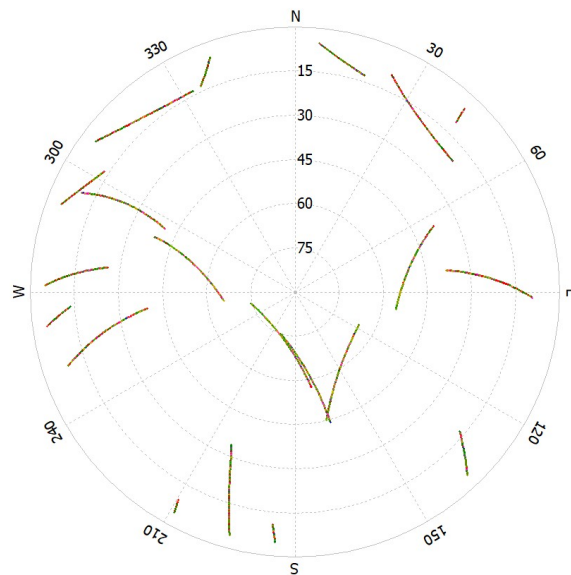


Figure 6.16: Sky-plot with visible satellites along with elevation and azimuth angle, from Carabas-3 flight FWD0929b

The DOP values for FWD0929b are displayed in figure 6.17 below . The x-axis represents time in hours and the y-axis represents $\frac{N_{satellites}}{DOP} \cdot 10(\epsilon \geq 0^\circ)$ where $N_{satellites}$ is the number of visible satellites and $(\epsilon \geq 0^\circ)$ represents visible satellites for the receiver. A higher value on the y-axis indicates a lower DOP. From this plot it is possible to deduce that the DOP values should not be affecting the performance of the system too much, since there are more than 10 satellites available with good satellite geometry in most dimensions. The sky-plots and DOP values for all flights can be seen in appendix B.

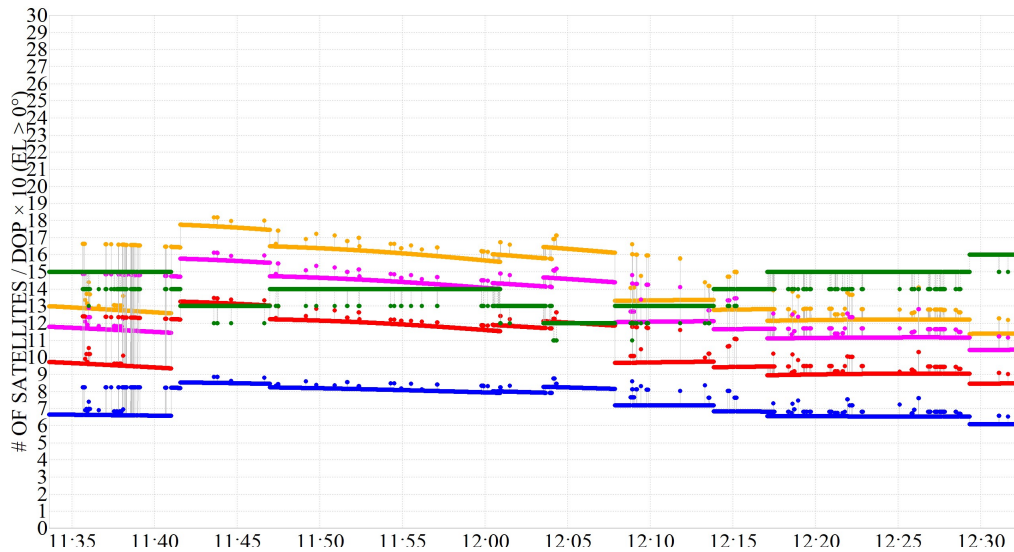


Figure 6.17: DOP from Carabas-3 flight FWD0929b where the yellow line represents geometric DOP (GDOP), the purple position DOP (PDOP), the green number of satellites available, the red vertical DOP (VDOP) and the blue horizontal DOP (HDOP).

6.7 Error in starting position

Since TDCP need two epochs of receiver positions at the start of the measurements it is of importance how accurate these positions have to be. Ideally, a simple GNSS code measurement with meter level accuracy should be sufficient for the starting positions. This would make the TDCP method completely independent from external base stations for positioning. To see how much an inaccurate starting position affects TDCP a normally distributed noise is applied to the initial RTK measurements used for the first positions. The noise is added with a mean of 0 meters and standard deviations of 15 m, 35 m and 50 m.

In figure 6.18 and 6.19 this drift error is plotted with the four different starting positions using the TDCP method. Figure 6.18 contains the drift with different offsets when using sp3-files and figure 6.19 contains the drift when using navigation message for satellite positions. The drift is measured with the RTK solutions as reference. The blue dash-dotted line with 0 m offset uses the RTK solution for its two first epochs in the TDCP method. From figure the figure it is possible to see that the drift increases when the starting position uncertainty is increased. It is however clear that TDCP with a starting position when a noise with 15 m standard deviation is applied performs similarly to when no noise is applied. This shows that it should be possible to use code measurements for the two initial epochs. The offsets seem to have a similar effect when using navigation message and sp3-files for satellite positions.

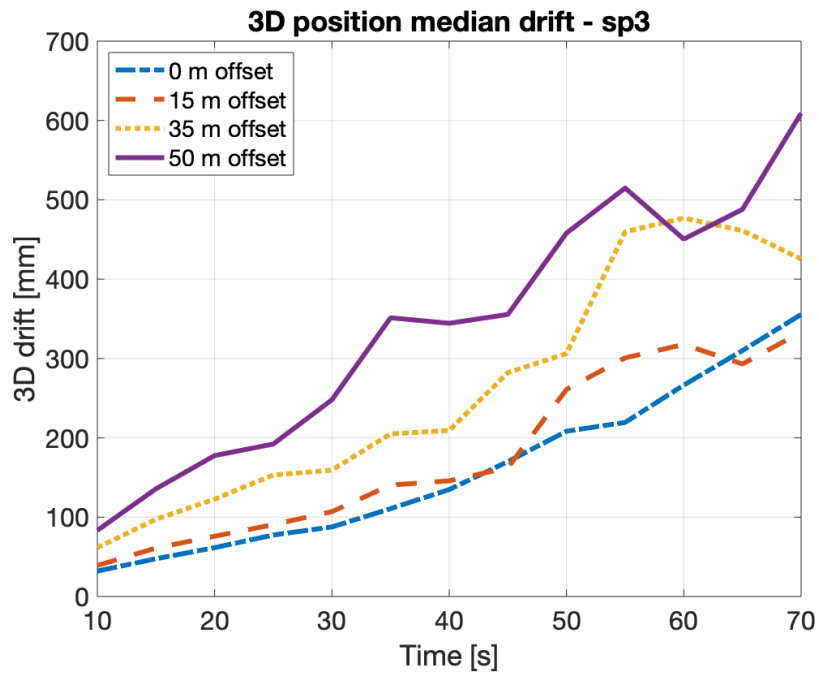


Figure 6.18: 3D positional drift from different starting positions using sp3-files for satellite positions

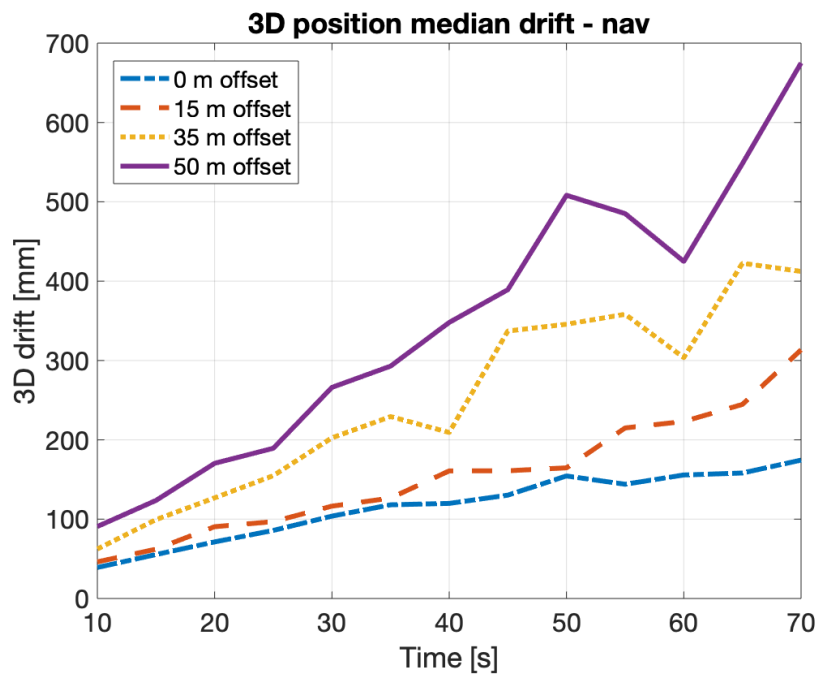


Figure 6.19: 3D positional drift from different starting positions using navigation file for satellite positions

6.8 Processed SAR image

To see how well TDCP performs compared to RTK when processing real SAR images from the CARABAS-3 system two SAR images of an area is created and compared. One is created using the position from RTK and one is created using the position from TDCP.

The processed SAR image is of a small area outside Linköping, Sweden ($58^{\circ}15'01.1''N$, $15^{\circ}34'57.4''E$) captured on flight FWD0611a. A satellite picture of the area is displayed in figure 6.20. The red lines and circles are to indicate what the points of interest in the SAR images are. The lines indicate a power line in the forest and the red circles indicate masts on a field.

The SAR equivalent when using RTK in the top of figure 6.21. The resulting SAR image from the same flight when using TDCP to track the flight path is seen at the bottom of the figure. When comparing the SAR images to the photographic image over the area, the masts in the red circles can be seen as reflectors and are clearly visible in both SAR images. The power line is also visible as a white line in the SAR images. There is no visible difference between the pictures which further indicates that TDCP works for the application as intended. If the SAR image processed from the TDCP method would have been blurrier than the one processed from RTK, the accuracy of the derived flight path from TDCP would probably be insufficient for SAR applications, since the autofocus algorithms in SAR processing need a relatively accurate position in order to refocus an image. The requirements for the precision depend on the type of algorithm that is used.



Figure 6.20: Satellite image from flight FWD0611a, the red arrows mark a power line which is visible in the SAR images, and the circles mark radio masts. Source: Google Earth [50].

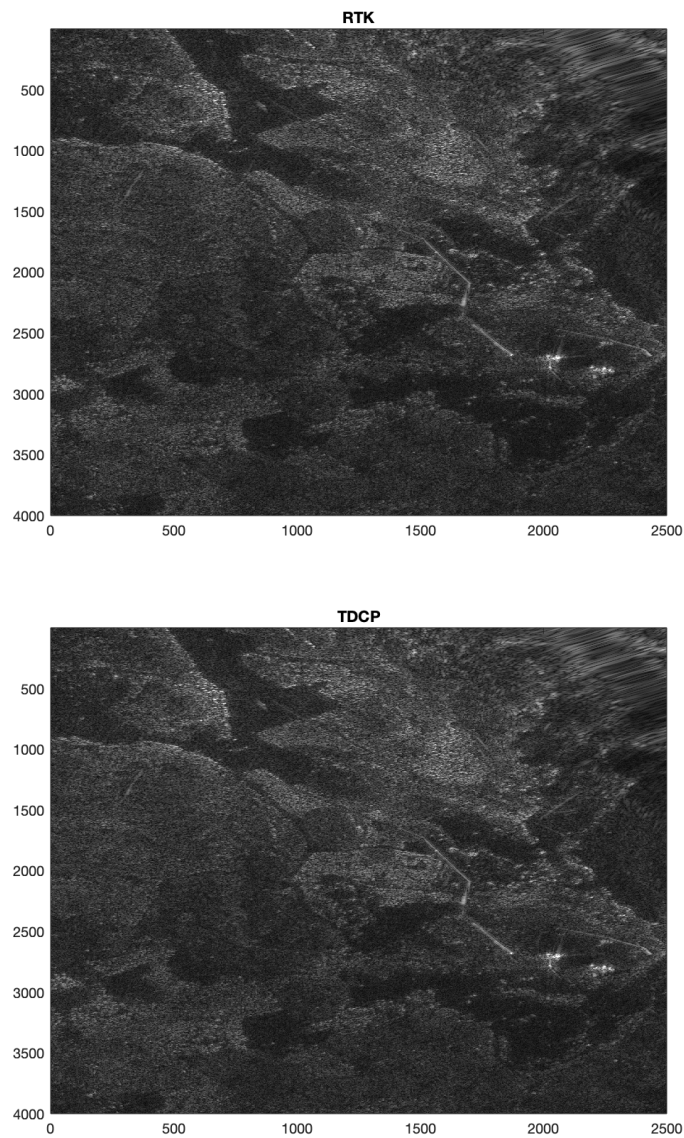


Figure 6.21: Processed SAR image from flight FWD0611a with RTK solution at the top and TDCP at the bottom. The white lines in the SAR images are electrical power lines which reflect the transmitted signal. And to the right in the pictures is a field with radio towers that also appears as bright spots on the SAR images. The blurry part in the top right corner is where the aircraft has flown, and no data is available in that area because of that, thus the unfocused area.

7

Discussion

7.1 Future of TDCP

In the future there could be a possibility to use the Galileo constellation as a measure of obtaining precise coordinates for the satellite positions instead of relying on external sp3-files. Galileo satellites has a higher upload rate of the navigation message which results in a reduction of the extrapolation errors in clock and orbit that can occur in e.g the GPS system. With this updated navigation message there could be an improvement in the performance of TDCP [51, 52].

With future improvements of the GNSS, the acquired position from the method can also be improved. There are several different methods and future ideas that could further increase the accuracy of receiver position when using TDCP. By using more satellites in the existing satellite systems improving the satellite geometry and mapping the behavior of the atmosphere even further can be enabled, which in turn could result in better accuracy of the position. Additionally, the method could be improved if more advanced GNSS receivers are available in combination with more sophisticated algorithms for cycle slip detection and repair. Since GNSS satellites are continuously developed to achieve higher signal quality, there is a possibility that TDCP could be preciser when satellites have advanced in their technology.

7.1.1 Future improvements for project

The next step for refining the method further would be to evaluate the possibilities of referenced TDCP. This could potentially enable the method to be more robust and sturdy towards the positional drift that is a problem for the ordinary TDCP, but with the drawback of being more sensitive to the derived starting position of the receiver. In order to implement referenced TDCP, the measurements for the starting epoch of the system will be used as a reference to the current epoch's measurements. Subsequently, the method will have a more solid reference for counteracting the drift, but with the mentioned drawback of being sensitive to the starting position since this is the reference point. When implementing referenced TDCP it is necessary to account for the cycle slips since there will be a change of reference point each time a cycle slip occurs.

The available GNSS data processed for the method does not involve data for any vehicle that travels above 40 m/s (144 km/h), this results in an uncertainty of how the velocity of the moving platform affects the performance of TDCP. There is a demand for positional accuracy of high velocity vehicles such as fighter jets (≈ 680 m/s) and regular airplanes (≈ 277 m/s) which travels far above 40 m/s, so an evaluation of how the method performs under such circumstances is needed. When higher velocity platforms are implemented for the method it is necessary to account for the higher precision requirements caused by fast variations from the intended aperture, as previously explained.

For this particular project the method was evaluated with the low frequency CARABAS-3 SAR system. Since SAR systems with higher operating frequency yield higher resolution radar images, there is an interest in adapting the method to work with such systems as well. However, with higher frequency the demands of positional accuracy will increase as well. An investigation of how TDCP performs for a system with high operating frequency on a fast platform is of high interest, this would result in a system that would require high positional accuracy but only for a fraction of the time, since high velocity platforms limit the integration time for the SAR (shorter SAR runs). Since the positional accuracy needed is dependant on the frequency of the SAR system it would be interesting to see how high the frequency can be before autofocus algorithms has to be used. Without involving autofocus algorithms for the SAR processing, the derived method will not yield sufficient precision to be implemented for faster platforms with SAR systems with operating frequencies, where the wavelengths are much smaller than the positional accuracy. However, the system could meet the requirements for SAR processing when auto focus is used, depending on what algorithm is used and how TDCP performs during higher velocities.

There would also be of interest to evaluate how much different auto focusing algorithms for SAR images can improve the requirements for the method, and get quantitative data for the requirements of the method with auto focusing included. The results in the project are displayed without taking into consideration the impact of auto focus, which has the ability to increase the allowable positional error for the method while still obtaining focused radar images after processing is done.

If more data from the CARABAS-3 flights was available for processing, the reasons for some files being worse than others might be explained. If the reasons are found the future flights can be more tailored to use with the TDCP algorithm.

8

Conclusion

The median position drift when using time differenced carrier phase (TDCP) is less than 100 mm after 60 seconds for all dimensions separately and around 160 mm after 60 seconds in 3D, it is shown that TDCP is a viable option to use when a position of a GNSS receiver is required for a short time period. If the method is implemented to work for applications with more substantial time periods of data collecting, the derived position has a tendency to drift from the true path, so other methods would be preferable in those cases. TDCP differs from other methods since its performance is not degraded when using the broadcasted navigation message from the satellites instead of using orbital products from suppliers (sp3-files). These orbital products would be more suitable for the method if they had a higher update rate or if a more appropriate interpolation method between the positions would be used, since the quality of the satellite positions are higher with sp3-files. TDCP effectively removes the need for base stations for differencing (RTK) at the cost of some positional drift. This results in a system which is independent from the need of external information and not reliant on any suppliers, this enables the method to be implemented for applications where operational redundancy is indispensable for a system. Additionally, TDCP has lower requirements for the precision of the starting position when compared to similar systems, since it is structurally based on relative positioning instead of absolute positioning. In conclusion this results in a GNSS methods which is independent, robust and adaptive, but with the drawback of being sensitive to position drift over time. Subsequently, TDCP is a suitable method for obtaining a position of an airborne vehicle during short SAR runs.

References

- [1] W A. Holm M A. Richards, J A. Scheer. *Principles of Modern Radar*, volume 1. SciTech Publishing, Raleigh, NC, 2010.
- [2] J A. Scheer W L. Melvin. *Principles of Modern Radar*, volume 2. SciTech Publishing, Raleigh, NC, 2013.
- [3] Gustafsson F Sjanic Z. "Simultaneous Navigation and SAR Auto-focusing" [Online], available: <https://www.diva-portal.org/smash/get/diva2:374840/FULLTEXT01.pdf>. accessed on 2022-06-09.
- [4] K. Herndon, F. Meyer, A. Flores, E. Cherrington, and L. Kucera. What is synthetic aperture radar? *NASA Earthdata open access for open science*, mar 2021. accessed on 2022-03-21.
- [5] Zoran Sjanic and Fredrik Gustafsson. Simultaneous navigation and sar auto-focusing. In *2010 13th International Conference on Information Fusion*, pages 1–7, 2010.
- [6] R M. Majewski W G. Carrara, R S. Goodman. *Spotlight Synthetic Aperture Radar, Signal Processing Algorithms*, volume 1. ARTECH HOUSE, INC., 685 Canton Street Norwood, MA 02062, 1995.
- [7] A. Gustavsson L. Ulander, P-O. Frölinde. "Bistatisk och passiv radar, årsrapport 2012, FOI, Totalförsvarets forskningsinstitut" [Online], available: <https://www.foi.se/rest-api/report/FOI-R--3588--SE>, Dec 2012. accessed on 2022-03-14.
- [8] Aron Sommer and Jörn Ostermann. Flight path reconstruction from sar images and spotlight sar data. In *11th European Conference on Synthetic Aperture Radar*, June 2016.
- [9] VectorNav. "WHAT IS AN INERTIAL NAVIGATION SYSTEM?," [Online], available: <https://www.vectornav.com/resources/inertial-navigation-articles/what-is-an-ins>, 2007. accessed on 2022-05-25.

- [10] José Ángel Ávila Rodríguez. *On Generalized Signal Waveforms for Satellite Navigation*. PhD thesis, Universität der Bundeswehr München, 6 2008.
- [11] Pavan Kumar, Prashant K. Srivastava, Prasoon Tiwari, and R.K. Mall. Chapter 20 - application of gps and guss technology in geosciences. In George p. Petropoulos and Prashant K. Srivastava, editors, *GPS and GNSS Technology in Geosciences*, pages 415–427. Elsevier, 2021.
- [12] United States Government. "Space Segment," [Online], available: <https://www.gps.gov/systems/gps/space/>, 2021. accessed on 2022-06-07.
- [13] Wikipedia. "GPS satellite blocks," [Online], available: https://en.wikipedia.org/wiki/GPS_satellite_blocks, Dec 12 2021. accessed on 2022-02-09.
- [14] U.S. Coast Guard Navigation Center. GPS CONSTELLATION STATUS FOR 03/08/2022, [Online], available: <https://www.navcen.uscg.gov/?Do=constellationStatus>, 2022. accessed on 2022-03-08.
- [15] United States Government. "GPS III Satellite," [Online], available: <https://www.gps.gov/multimedia/images/>, 2021. accessed on 2022-02-11.
- [16] Quartzlock UK Ltd. "A GPS Frequency and Time Standard," [Online], available: <https://www.microwavejournal.com/articles/2271-a-gps-frequency-and-time-standard>, mar 1 1998. accessed on 2022-05-23.
- [17] Wikimedia Commons. GGPS Signals, [Online], available: https://commons.wikimedia.org/wiki/File:GPS_Signals.png, May 2014. accessed on 2022-05-23.
- [18] College of Earth and Mineral Sciences, The Pennsylvania State University J Van Sickle. The Navigation Message, [Online], available: <https://www.e-education.psu.edu/geog862/node/1734>. accessed on 2022-03-07.
- [19] RRY095 Satellite Positioning J.Johansson. "Chalmers University of Technology, department of Space, Earth and Environment, Lectures 1-4, 6, 7-13, 15-16," [Online], available: <https://chalmers.instructure.com/courses/15927>, Okt-Dec 2021. accessed on 2022-02-11.
- [20] NASA. "What Is an Atomic Clock?," [Online], available: <https://www.nasa.gov/feature/jpl/what-is-an-atomic-cloc>, Jun 19 2019. accessed on 2022-03-03.
- [21] navipedia ESA. "Code-Carrier Divergence Effect" [Online], available: https://gssc.esa.int/navipedia/index.php/Code-Carrier_Divergence_Effect, Feb 23 2012. accessed on 2022-03-14.

-
- [22] H.Sakidin. "Simpler Nonhydrostatics UNBab Mapping Function for Tropospheric Delay" [Online], available:., Jun 2013. accessed on 2022-06-01.
- [23] Qiu Cong, Xiaoming Wang, Zishen Li, Zhang Shaotian, Haobo Li, Jinglei Zhang, and Hong Yuan. The performance of different mapping functions and gradient models in the determination of slant tropospheric delay. *Remote Sensing*, 12:130, 01 2020.
- [24] Andre Balogh, H. Hudson, K. Petrovay, and Rudolf Von Steiger. Introduction to the solar activity cycle: Overview of causes and consequences. *Space Science Reviews*, 186:1–15, 12 2014.
- [25] G. Blewitt. Basics of the gps technique : Observation equations. 2000.
- [26] R.B. Langley. Dilution of precision. *GPS World*, 10(5):52—59, 1999.
- [27] GISGeography. GPS Accuracy: HDOP, PDOP, GDOP, Multipath the Atmosphere, [Online], available:.. <https://gisgeography.com/gps-accuracy-hdop-pdop-gdop-multipath/>, June 2021. accessed on 2022-02-28.
- [28] M.Brenneman. "Mitigation of GPS Multipath Using Polarization and Spatial Diversities," [Online], available:.. https://www.academia.edu/76833145/Mitigation_of_GPS_Multipath_Using_Polarization_and_Spatial_Diversities, 2007. accessed on 2022-05-23.
- [29] Wei. J Tang. Z Wang. B, Li. T. "A new unambiguous tracking algorithm for sine-BOC(m,n) signals, GPS Solutions," [Online], available:.. <https://link.springer.com/article/10.1007/s10291-019-0849-8#citeas>, Apr 08 2019. accessed on 2022-03-15.
- [30] navipedia ESA. "Relativistic Clock Correction," [Online], available:.. https://gssc.esa.int/navipedia/index.php/Relativistic_Clock_Correction, jul 08 2018. accessed on 2022-04-11.
- [31] International GNSS Service (IGS), RINEX Working Group and Radio Technical Commission for Maritime Services Special Committee 104 (RTCM-SC104). RINEX: The Receiver Independent Exchange Format, version 3.03, [Online], available:.. <https://gssc.esa.int/wp-content/uploads/2018/07/RINEX-303.pdf>, jul 14 2015. accessed on 2022-03-08.
- [32] I. Romero. RINEX: The Receiver Independent Exchange Format, version 4.00, [Online], available:.. https://files.igs.org/pub/data/format/rinex_4.00.pdf, dec 1 2021. accessed on 2022-03-08.
- [33] International GNSS Service (IGS) / CDDIS. "IGS NETWORK - 512 STATIONS DISPLAYED," [Online], available:.. <https://www.igs.org/network#station-map-list>, 2020. accessed on 2022-05-05.

- [34] Riddell A. Hausler G Johnston, G. "The International GNSS Service. Teunissen, Peter J.G., Montenbruck, O. (Eds.), Springer Handbook of Global Navigation Satellite Systems (1st ed., pp. 967-982)" [Online], available: <https://igs.org/products/>, 2017. accessed on 2022-02-17.
- [35] Z. Deng, M. Fritsche, T. Nischan, M. Bradke. Multi-GNSS Ultra Rapid Orbit-, Clock- EOP-Product Series. GFZ Data Services., [Online], available: <https://doi.org/10.5880/GFZ.1.1.2016.003>, 2016. accessed on 2022-03-08.
- [36] Z. Deng, H. Schuh. We are working on the future of the satellite navigation technique!, [Online], available: <https://geobm.de/about-geobm/>, 2018. accessed on 2022-03-08.
- [37] Federal Agency for Cartography and Geodesy. The International Celestial Reference System (ICRS), [Online], available: <https://www.iers.org/IERS/EN/Science/ICRS/ICRS.html>, 2013. accessed on 2022-03-08.
- [38] ESA, navipedia. "Reference Systems and Frames", [Online], available: https://gssc.esa.int/navipedia/index.php/Reference_Systems_and_Frames, Jan 10 2014. accessed on 2022-03-08.
- [39] Lantmäteriet. RTK, [Online], available: <https://www.lantmateriet.se/sv/Kartor-och-geografisk-information/gps-geodesi-och-swepos/GPS-och-satellitpositionering/Metoder-for-GNSS-matning/RTK/>. accessed on 2022-03-07.
- [40] J. Arvidsson. "GPS Based Flight Motion Capture, Development and evaluation of a high-performance standalone GPS navigation solution for an airborne radar system" [Online], available: <https://odr.chalmers.se/handle/20.500.12380/244962>, 2016. accessed on 2022-03-16.
- [41] Inside GNSS. "GNSS Filtering Options" [Online], available: <https://insidegnss.com/gnss-filtering-options/>, 2013. accessed on 2022-03-21.
- [42] Pierluigi Freda, Antonio Angrisano, Salvatore Gaglione, and Salvatore Troisi. Time-differenced carrier phases technique for precise gnss velocity estimation. *GPS Solutions*, 19:335–341, 04 2015.
- [43] Yingwei Zhao. Applying time-differenced carrier phase in nondifferential gps/imu tightly coupled navigation systems to improve the positioning performance. *IEEE Transactions on Vehicular Technology*, 66(2):992–1003, 2017.
- [44] ESA. "Examples of multi-frequency Cycle-Slip Detectors," [Online], available: https://gssc.esa.int/navipedia/index.php/Examples_of_multi-frequency_Cycle-Slip_Detectors, February 2012. accessed on 2022-02-02.
- [45] Zhen Dai. Matlab software for gps cycle-slip processing. *GPS Solutions*, 16:267–

272, 04 2012.

- [46] Igor V. Bezmenov. Effective algorithms for detection outliers and cycle slip repair in gnss data measurements. In Tien Nguyen, editor, *Satellite Systems*, chapter 9. IntechOpen, Rijeka, 2021.
- [47] Pieter P. "Simple Moving Average" [Online], available: <https://tttapa.github.io/Pages/Mathematics/Systems-and-Control-Theory/Digital-filters/Simple%20Moving%20Average/Simple-Moving-Average.html>, Sep 23 2020. accessed on 2022-06-01.
- [48] Pieter P. "Exponential Moving Average" [Online], available: <https://tttapa.github.io/Pages/Mathematics/Systems-and-Control-Theory/Digital-filters/Exponential%20Moving%20Average/Exponential-Moving-Average.html>, Oct 03 2020. accessed on 2022-06-01.
- [49] Wikipedia. "Runge's phenomenon," [Online], available: https://en.wikipedia.org/wiki/Runge%27s_phenomenon, May 20 2022. accessed on 2022-06-02.
- [50] Google Earth. "Outside Linköping, Sweden, 58.250300, 15.582600" [Online], available:, Aug 26 2019. accessed on 2022-04-11.
- [51] O. Montenbruck L. Carlin, A. Hauschild. "Precise point positioning with GPS and Galileo broadcast ephemerides" [Online], available: <https://link.springer.com/article/10.1007/s10291-021-01111-4#rightslink>, 2021. accessed on 2022-04-06.
- [52] T. Burger L. Ries S. Schlötzer B.E. Schotsch M. Ouedraogo S. Damy E. Chatre M. Jeannot J. Godet D. Hayes M. Paonni, M. Anghileri. "Improving the Performance of Galileo E1-OS by Optimizing the I/NAV Navigation Message" [Online], available: https://www.gsc-europa.eu/sites/default/files/sites/all/files/IonGnss19_InavOptimisation_FullPaper_GSC.pdf, 2019. accessed on 2022-03-21.

A

Number of runs processed for
spliced flight data

Table A.1: Number of runs processed from four SAR flights.

Duration of run [s]	Number of runs processed
1	3063
3	1007
5	596
7	422
9	324
11	257
13	217
15	187
17	160
19	142
21	127
23	113
25	101
27	96
29	85
31	80
33	75
35	71
37	64
39	60
41	55
43	50
45	48
47	44
49	41
51	38
53	37
55	37
57	35
59	33
61	31
63	31
65	31
67	29
69	28
71	26
73	26
75	23
77	22
79	21
81	20

B

Stats of SAR runs from single SAR flights

B. Stats of SAR runs from single SAR flights

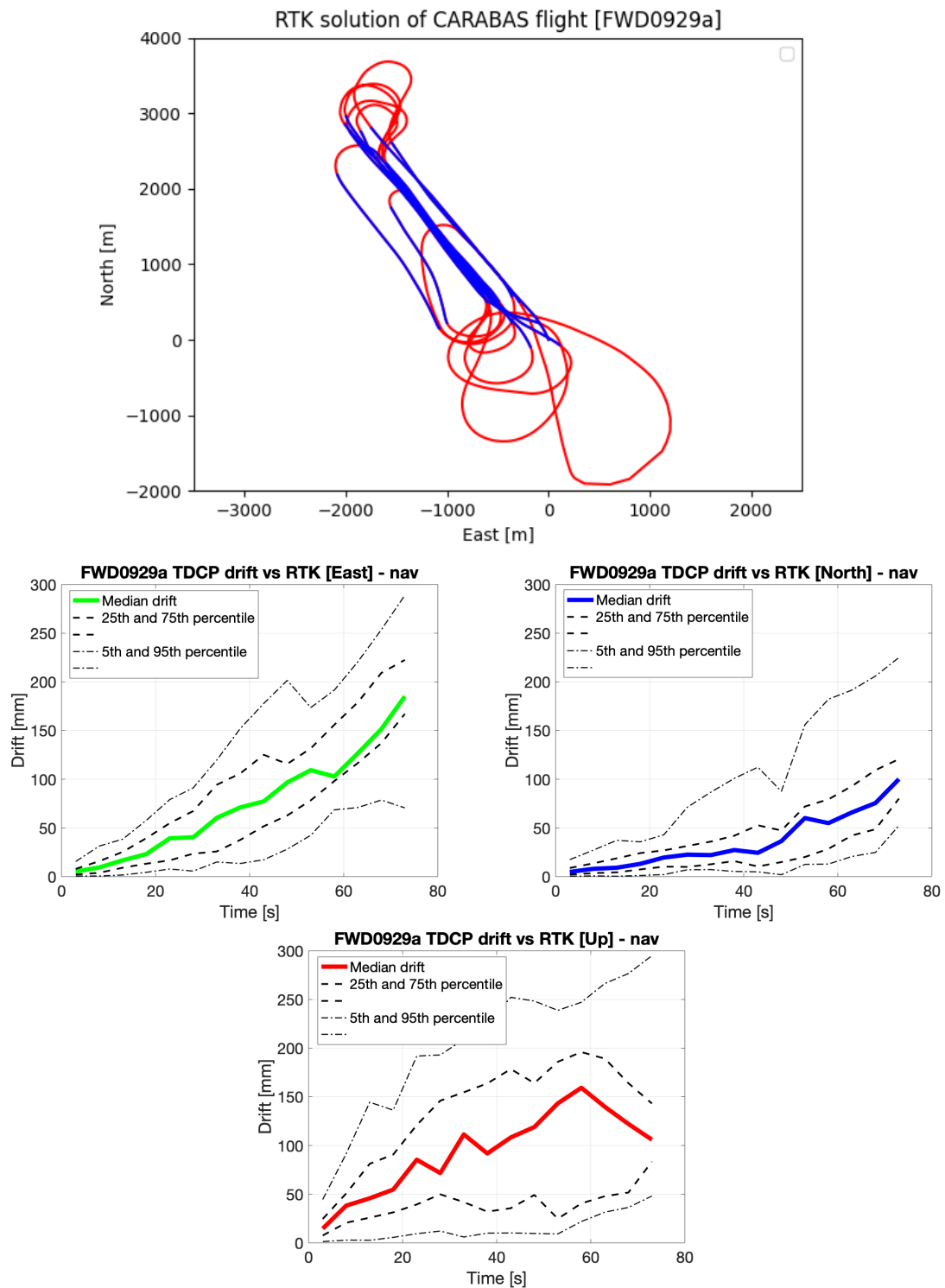


Figure B.1: FWD0929a Flight path with highlighted SAR runs (top) with East North and Up drifts using GPS navigation message

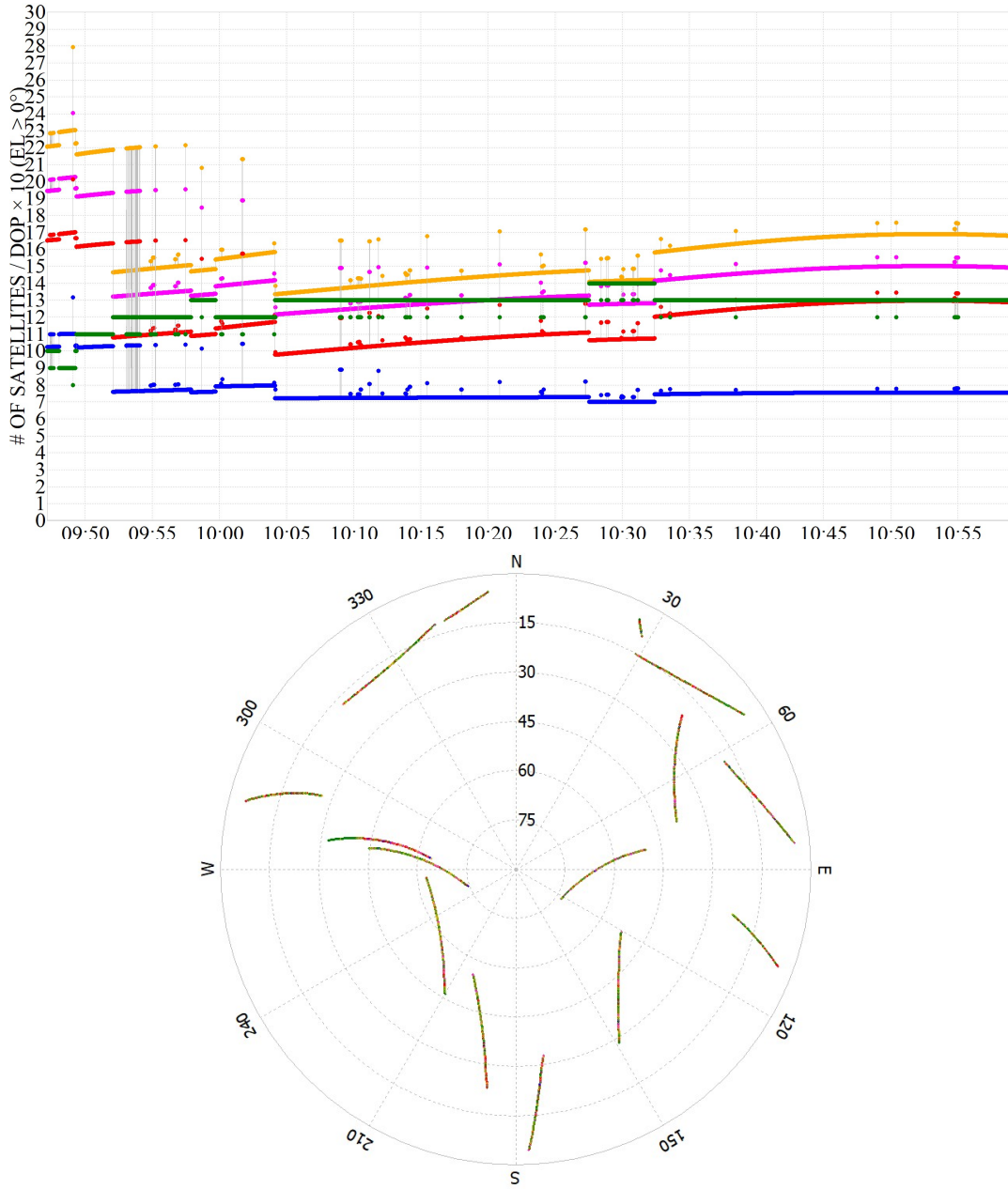


Figure B.2: FWD0929a DOP presented in number of visible satellites divided by DOP (top). Yellow line = GDOP, purple = PDOP, green = number of satellites visible, red = VDOP and blue = HDOP. Together with a skyplot for the satellites during the measurements (bottom)

B. Stats of SAR runs from single SAR flights

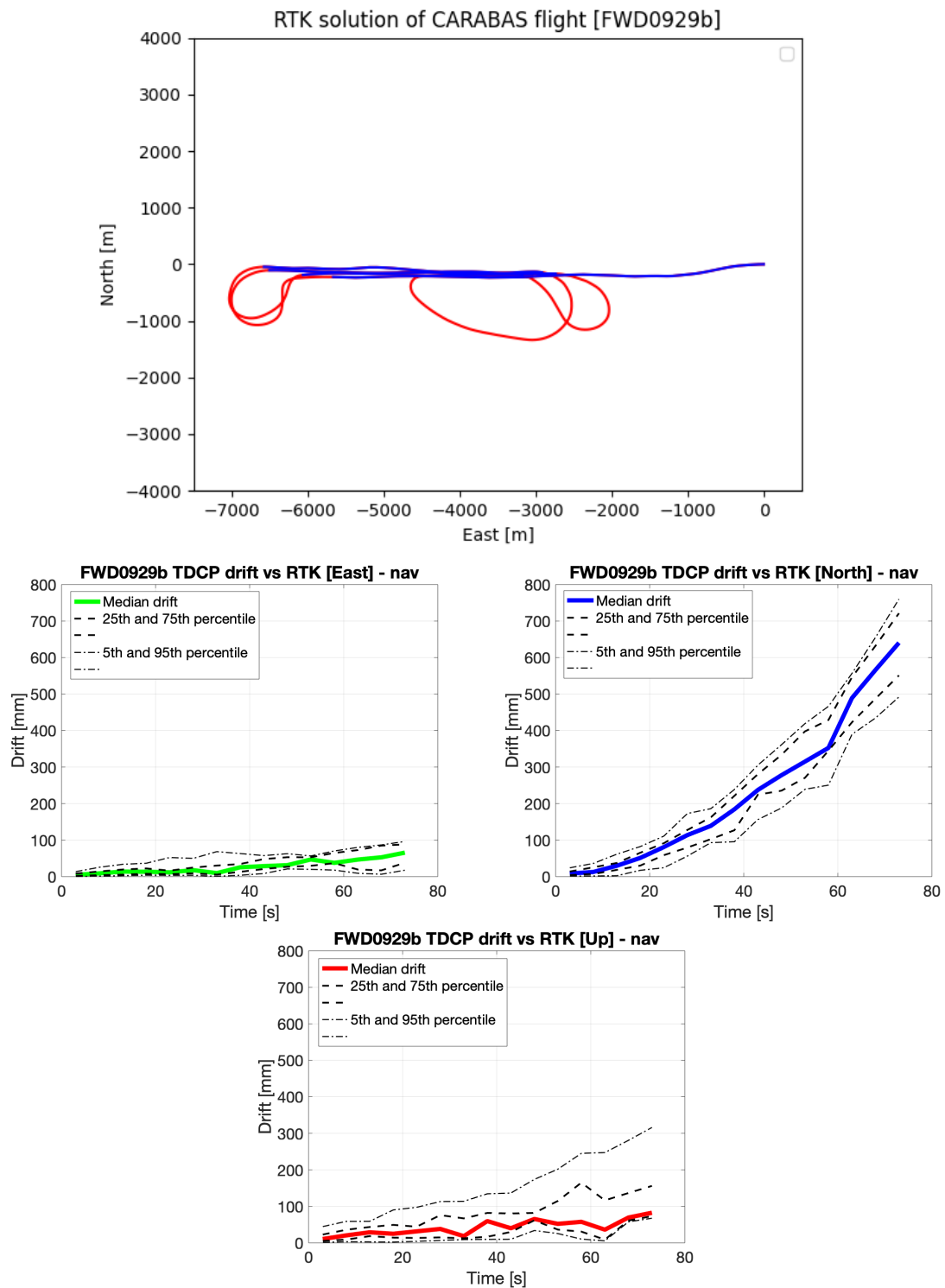


Figure B.3: FWD0929b Flight path with highlighted SAR runs (top) with East North and Up drifts using GPS navigation message

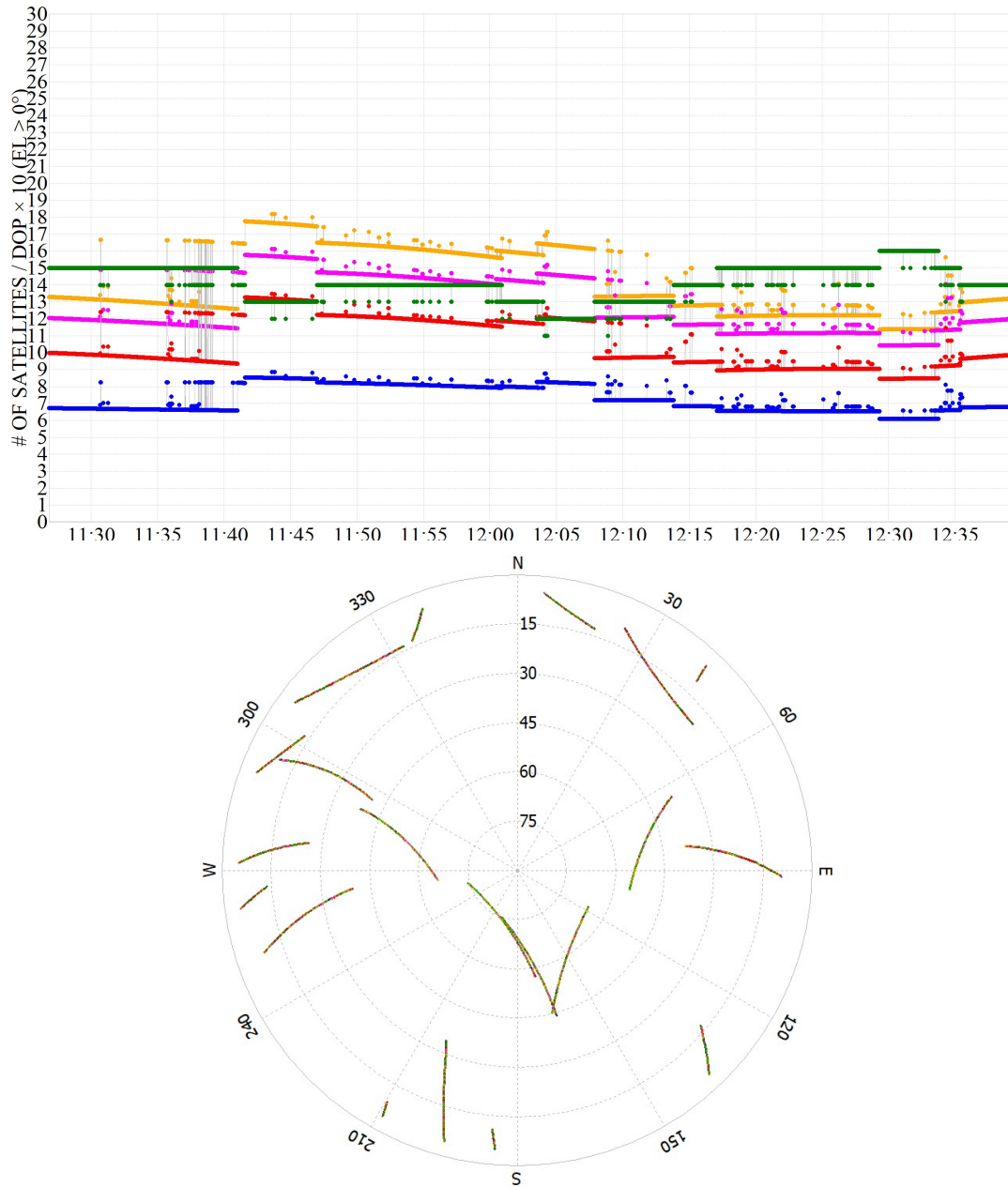


Figure B.4: FWD0929b DOP presented in number of visible satellites divided by DOP (top). Yellow line = GDOP, purple = PDOP, green = number of satellites visible, red = VDOP and blue = HDOP. Together with a skyplot for the satellites during the measurements (bottom)

B. Stats of SAR runs from single SAR flights

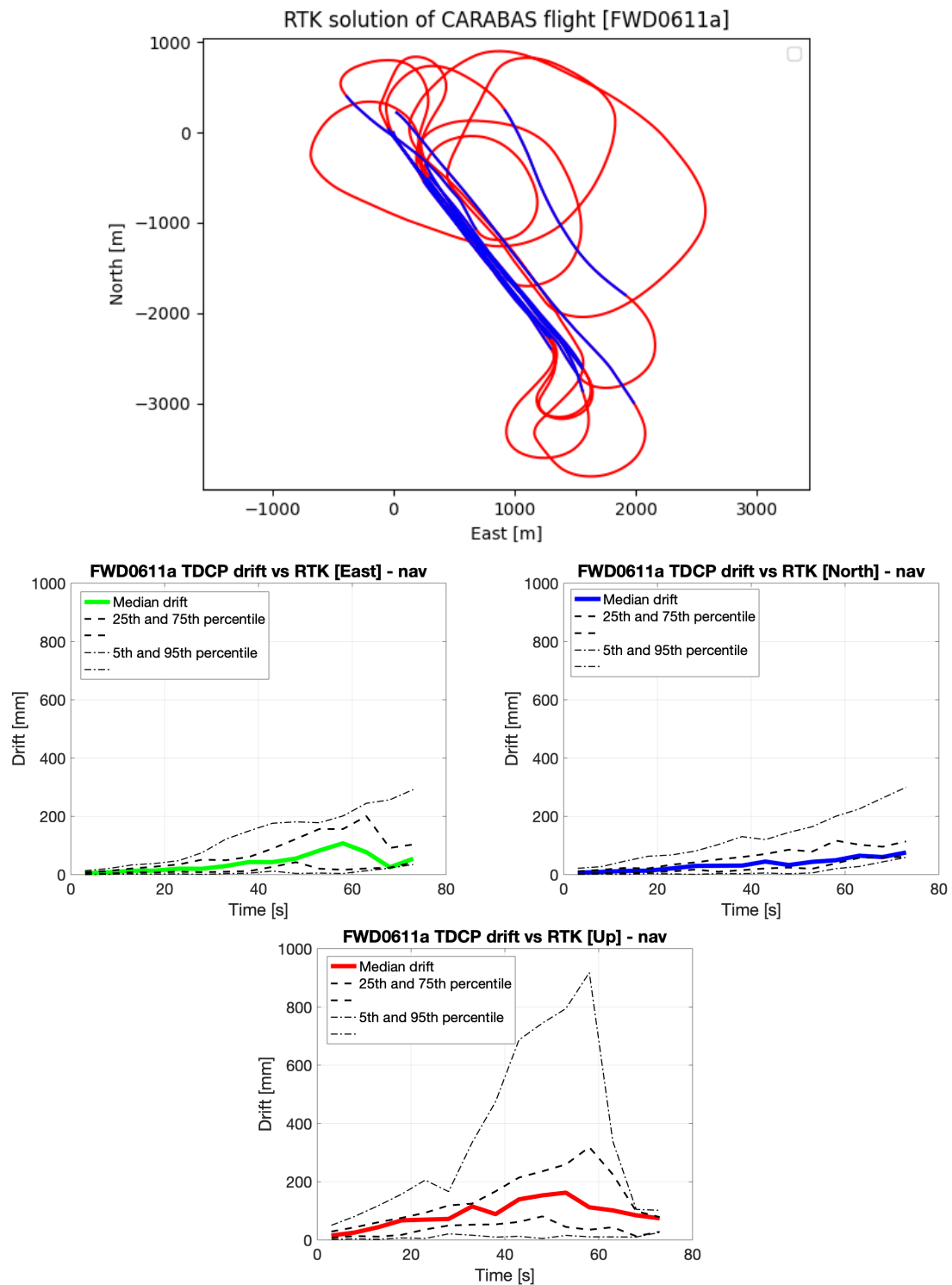


Figure B.5: FWD0611a Flight path with highlighted SAR runs (top) with East North and Up drifts using GPS navigation message

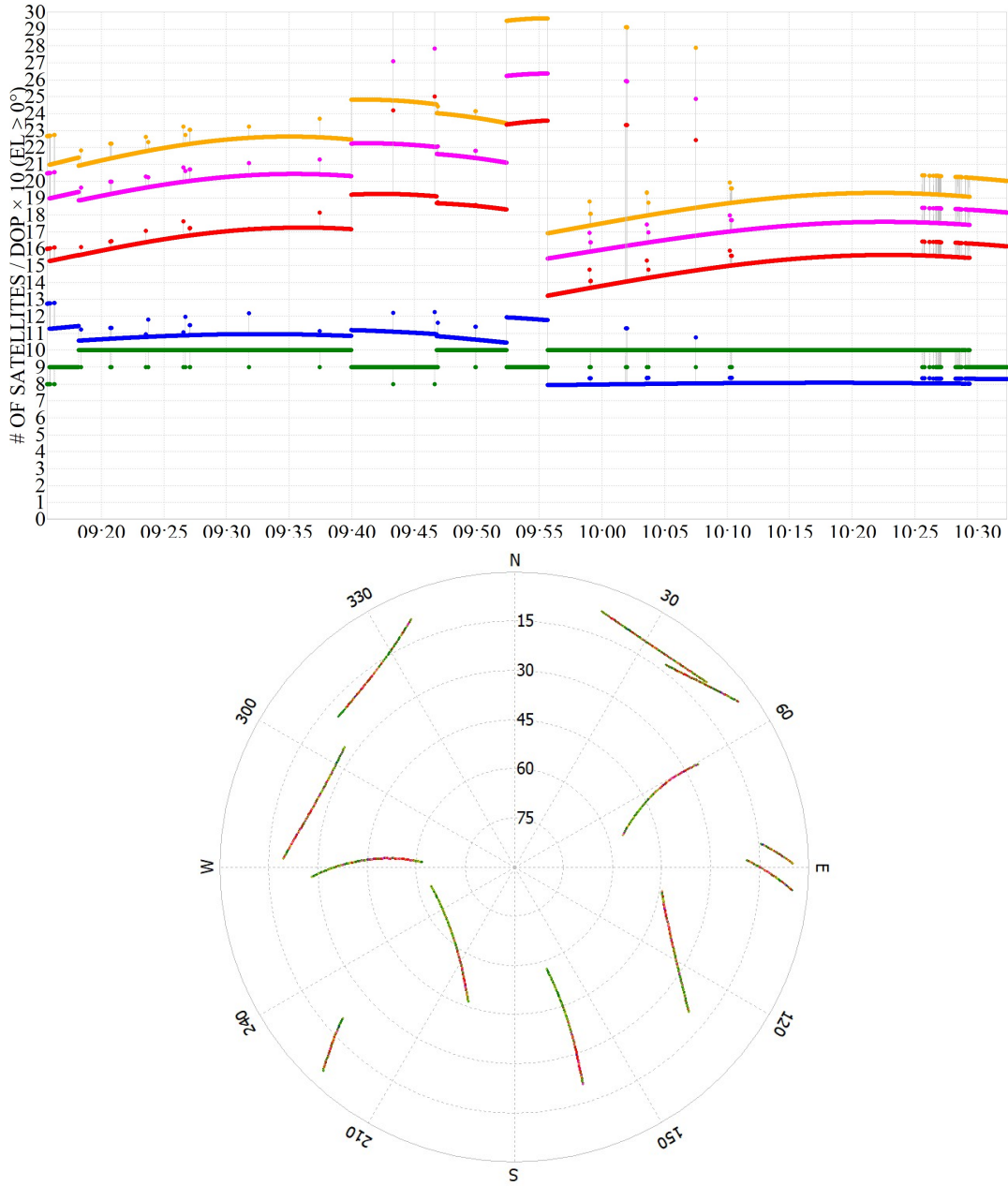


Figure B.6: FWD0611a DOP presented in number of visible satellites divided by DOP (top). Yellow line = GDOP, purple = PDOP, green = number of satellites visible, red = VDOP and blue = HDOP. Together with a skyplot for the satellites during the measurements (bottom)

B. Stats of SAR runs from single SAR flights

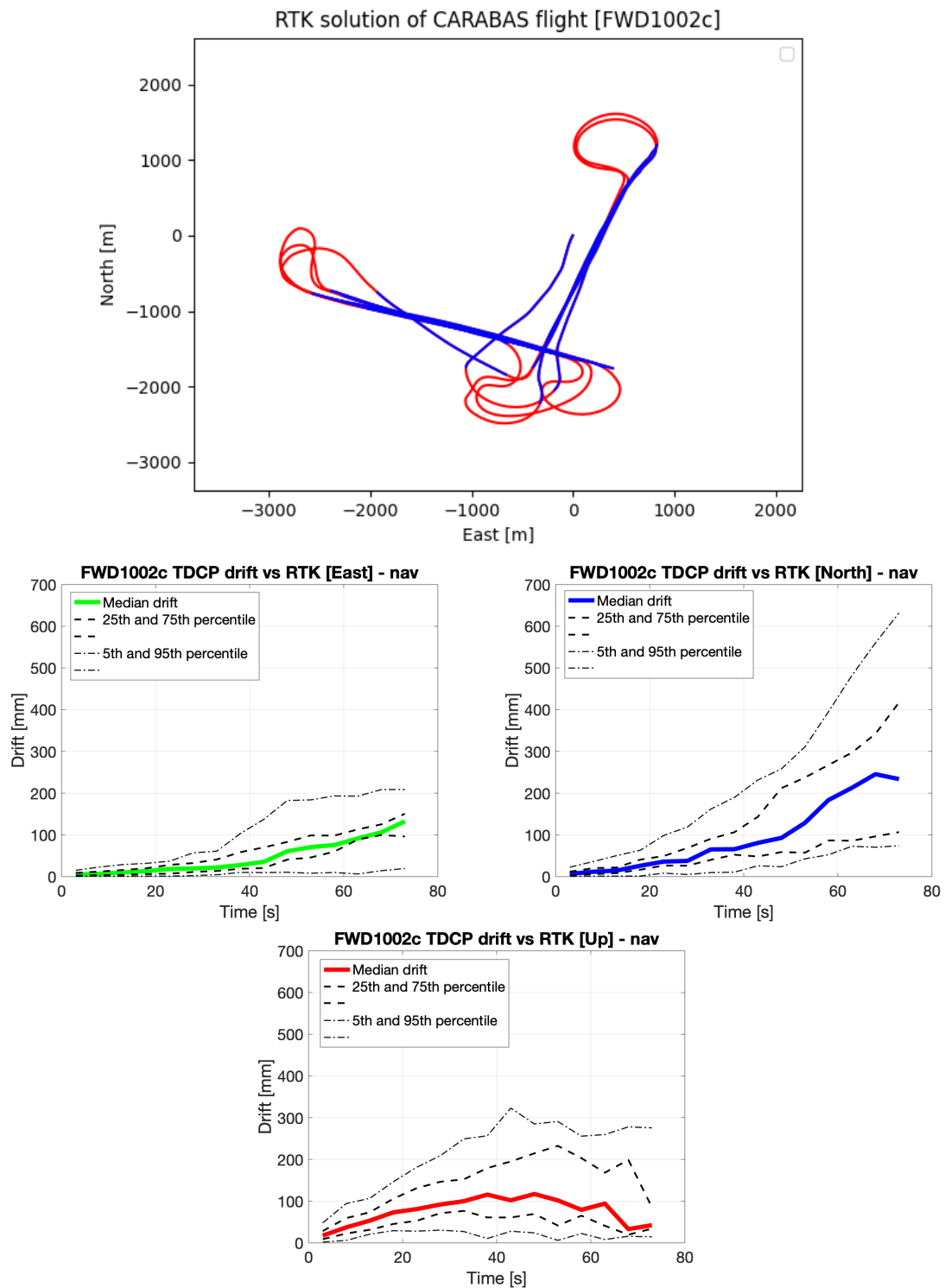


Figure B.7: FWD1002c Flight path with highlighted SAR runs (top) with East North and Up drifts using GPS navigation message

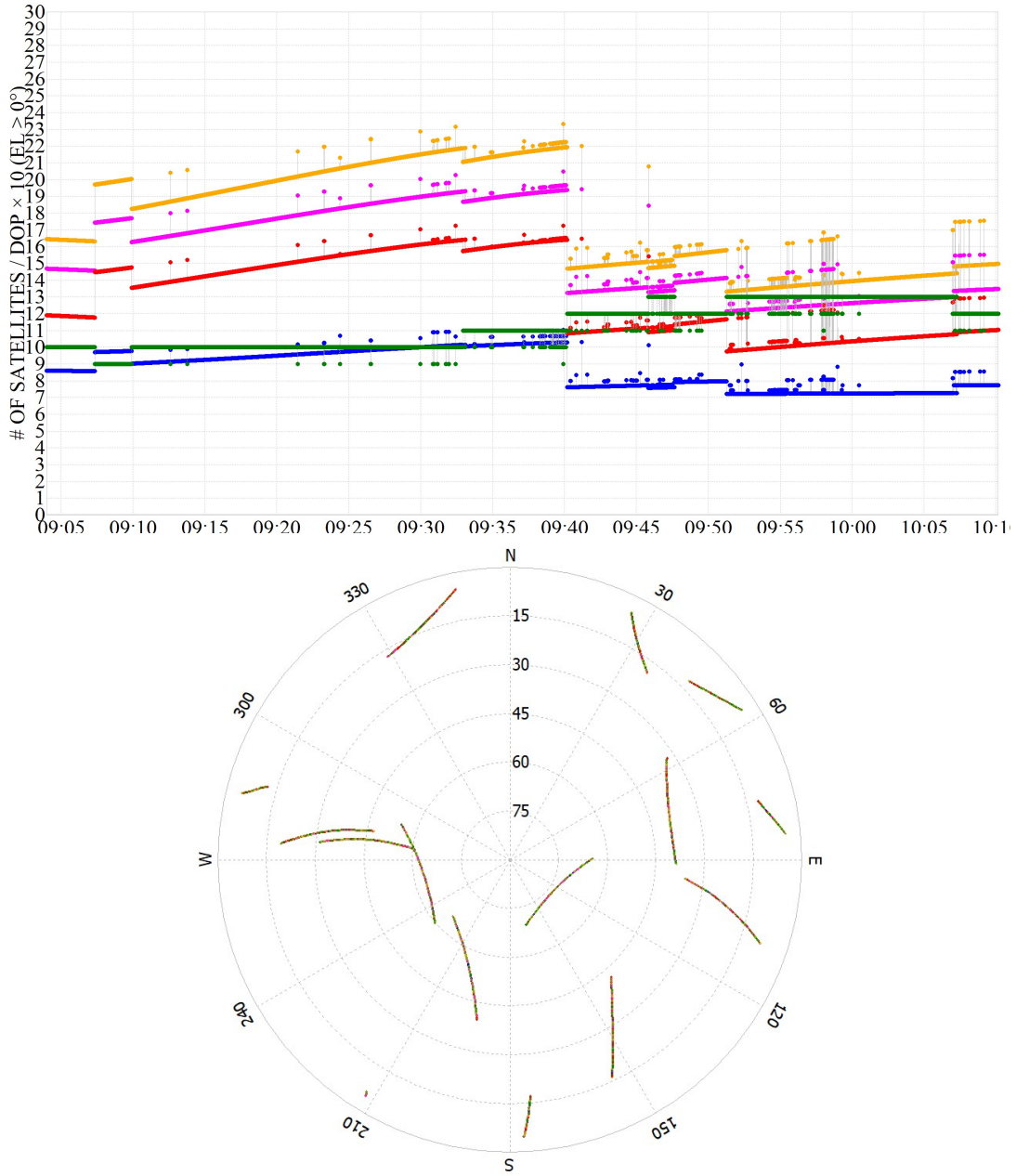


Figure B.8: FWD1002c DOP presented in number of visible satellites divided by DOP (top). Yellow line = GDOP, purple = PDOP, green = number of satellites visible, red = VDOP and blue = HDOP. Together with a skyplot for the satellites during the measurements (bottom)

B. Stats of SAR runs from single SAR flights

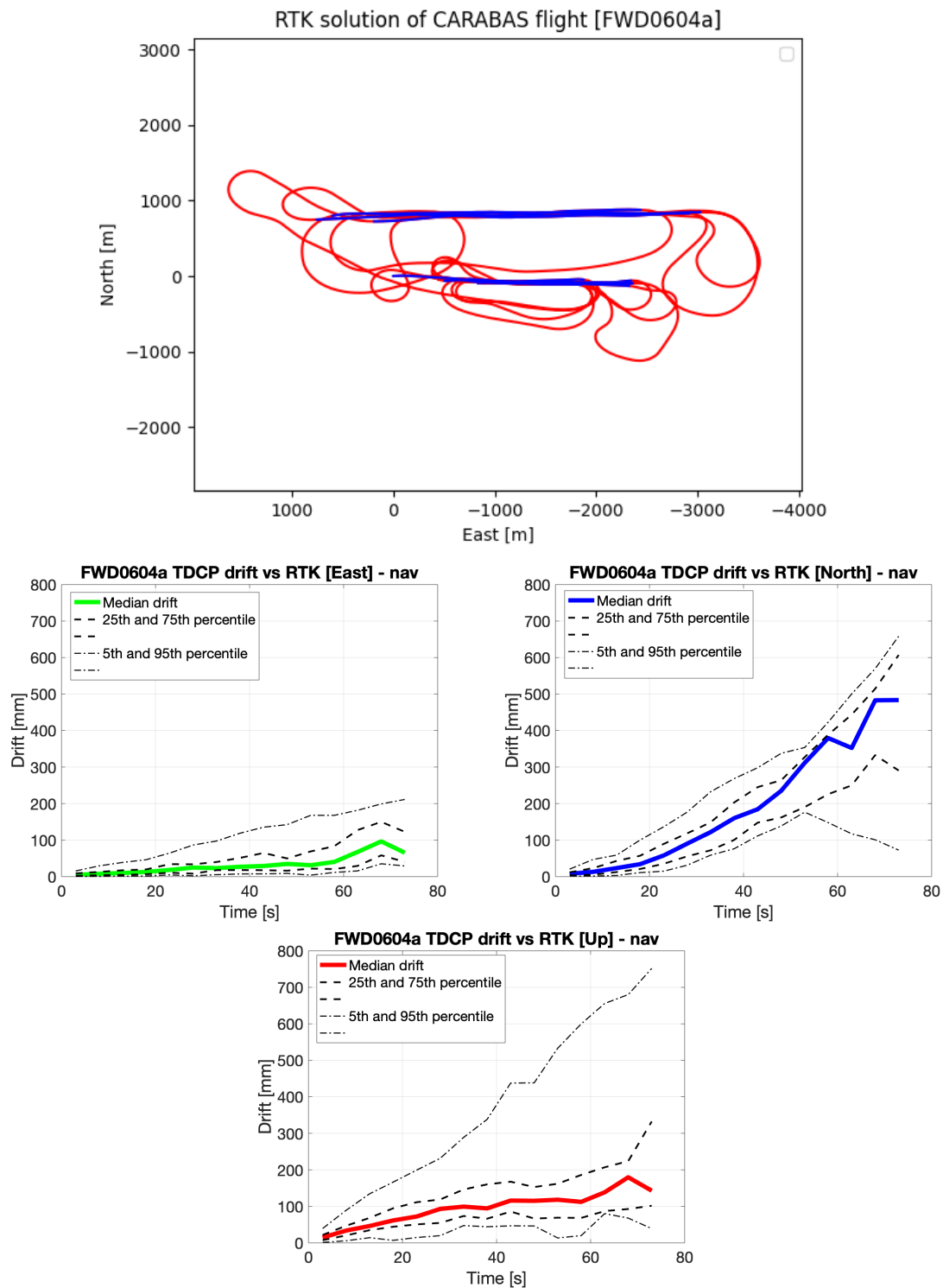


Figure B.9: FWD0604a Flight path with highlighted SAR runs (top) with East North and Up drifts using GPS navigation message

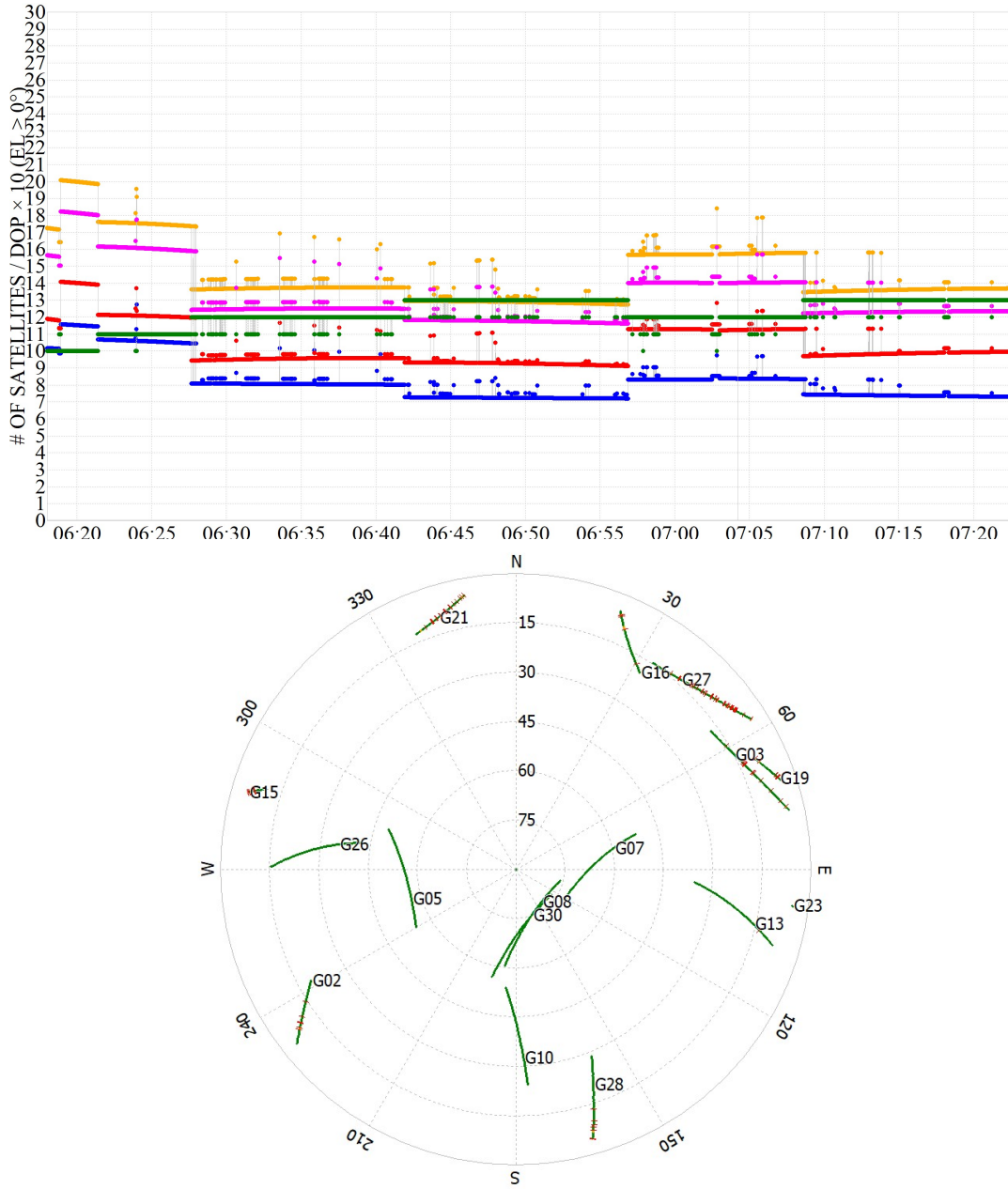


Figure B.10: FWD0604a DOP presented in number of visible satellites divided by DOP (top). Yellow line = GDOP, purple = PDOP, green = number of satellites visible, red = VDOP and blue = HDOP. Together with a skyplot for the satellites during the measurements (bottom)

B. Stats of SAR runs from single SAR flights

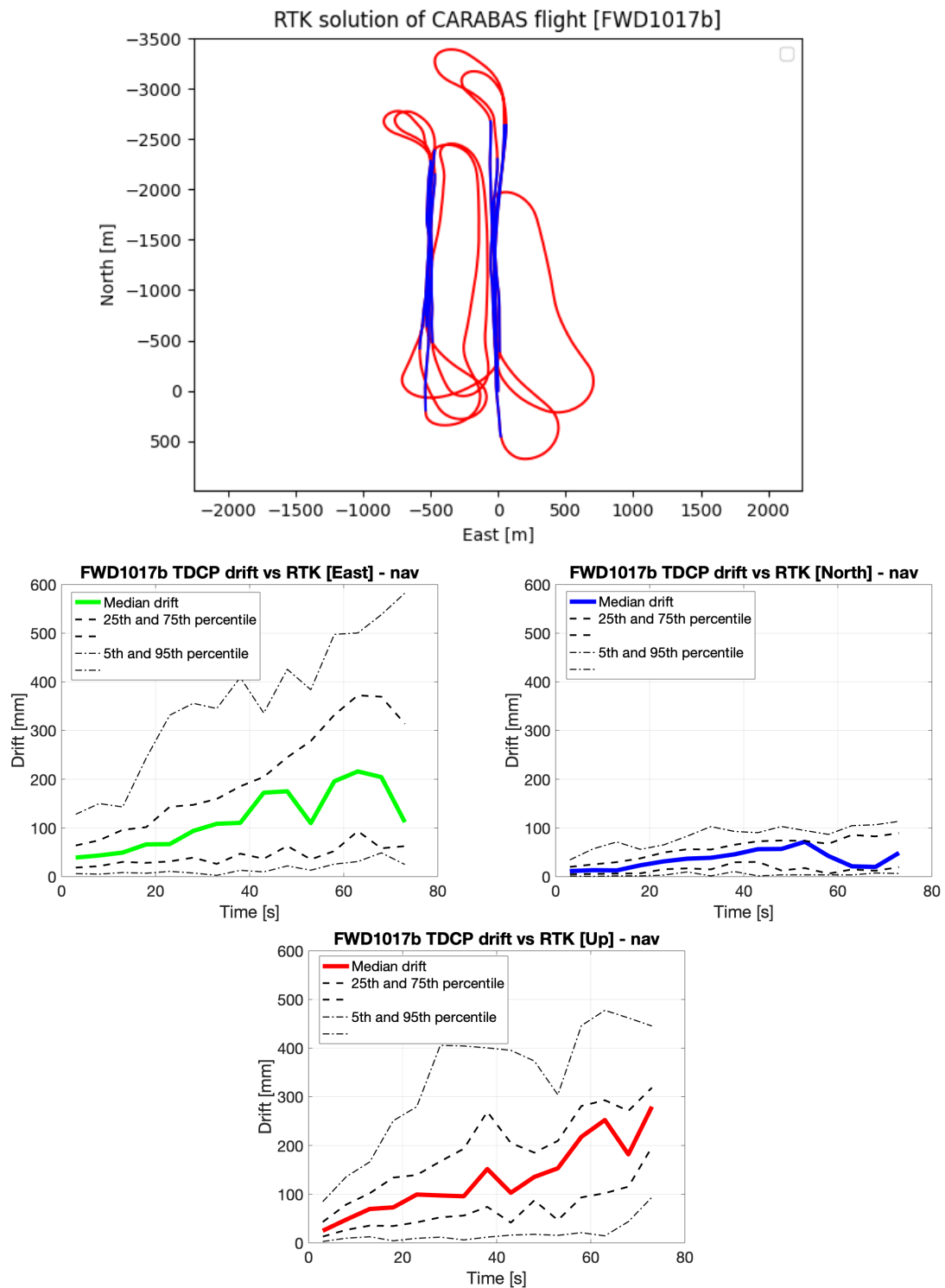


Figure B.11: FWD1017b Flight path with highlighted SAR runs (top) with East North and Up drifts using GPS navigation message

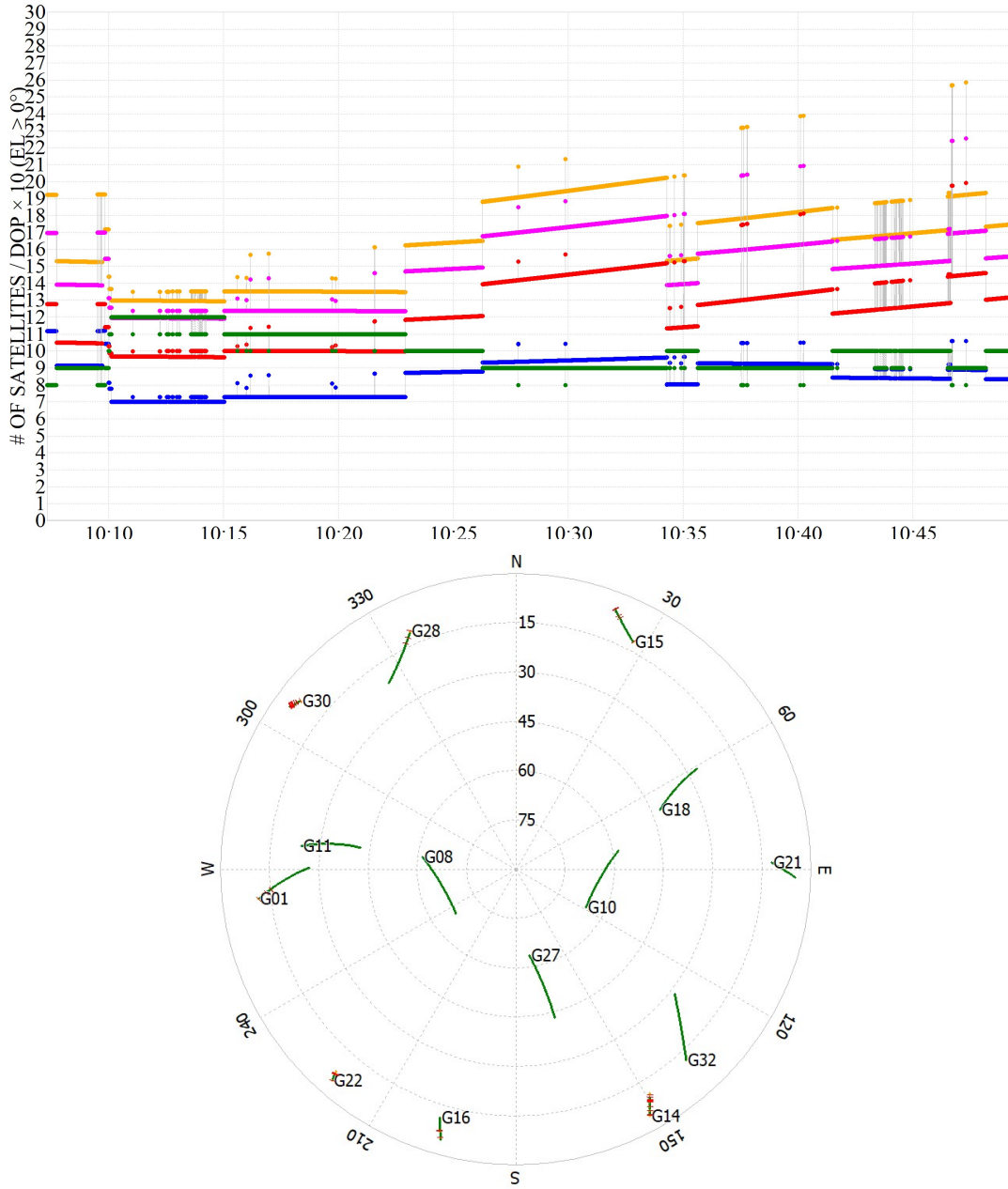


Figure B.12: FWD1017b DOP presented in number of visible satellites divided by DOP (top). Yellow line = GDOP, purple = PDOP, green = number of satellites visible, red = VDOP and blue = HDOP. Together with a skyplot for the satellites during the measurements (bottom)

B. Stats of SAR runs from single SAR flights

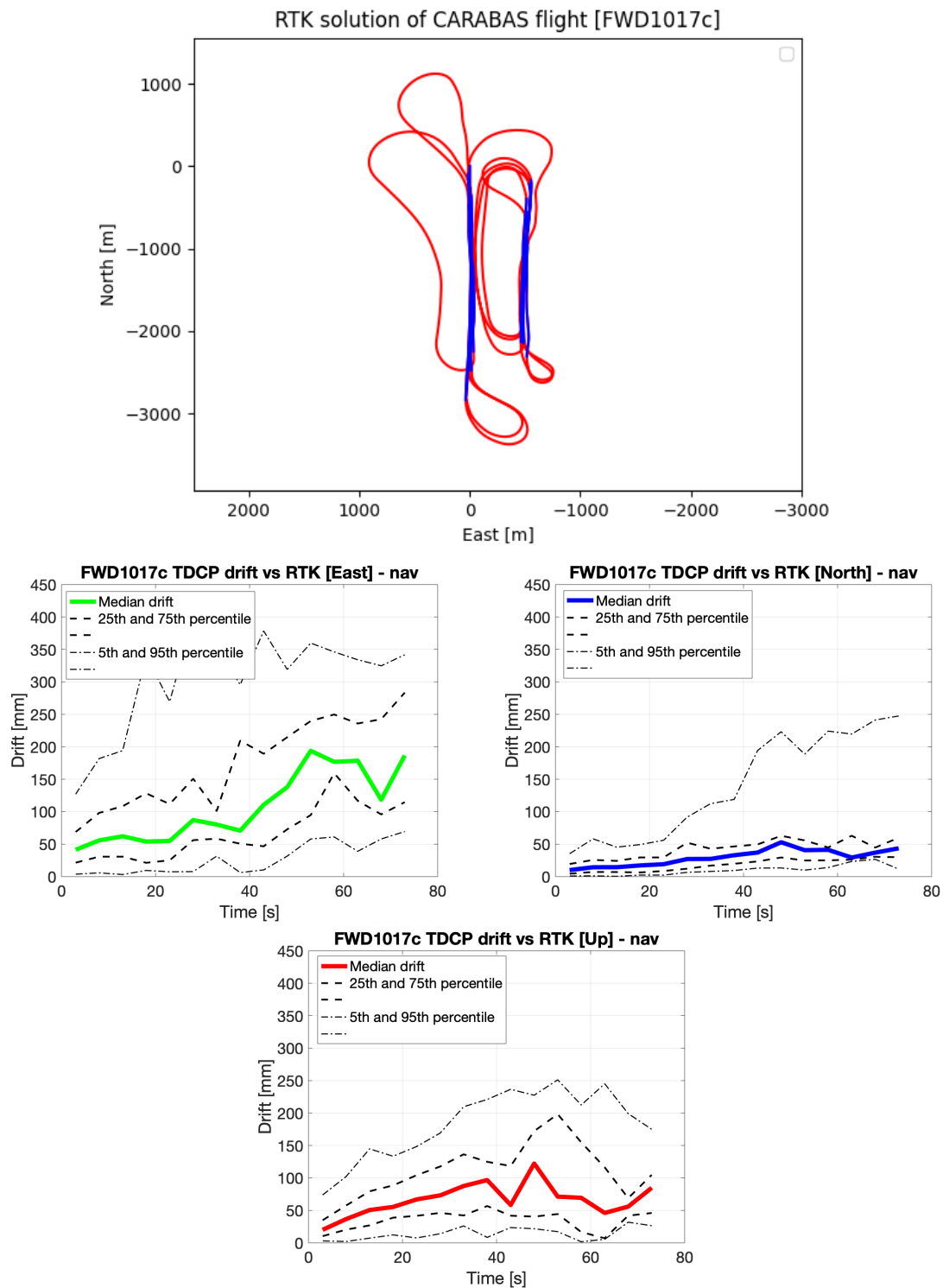


Figure B.13: FWD1017c Flight path with highlighted SAR runs (top) with East North and Up drifts using GPS navigation message

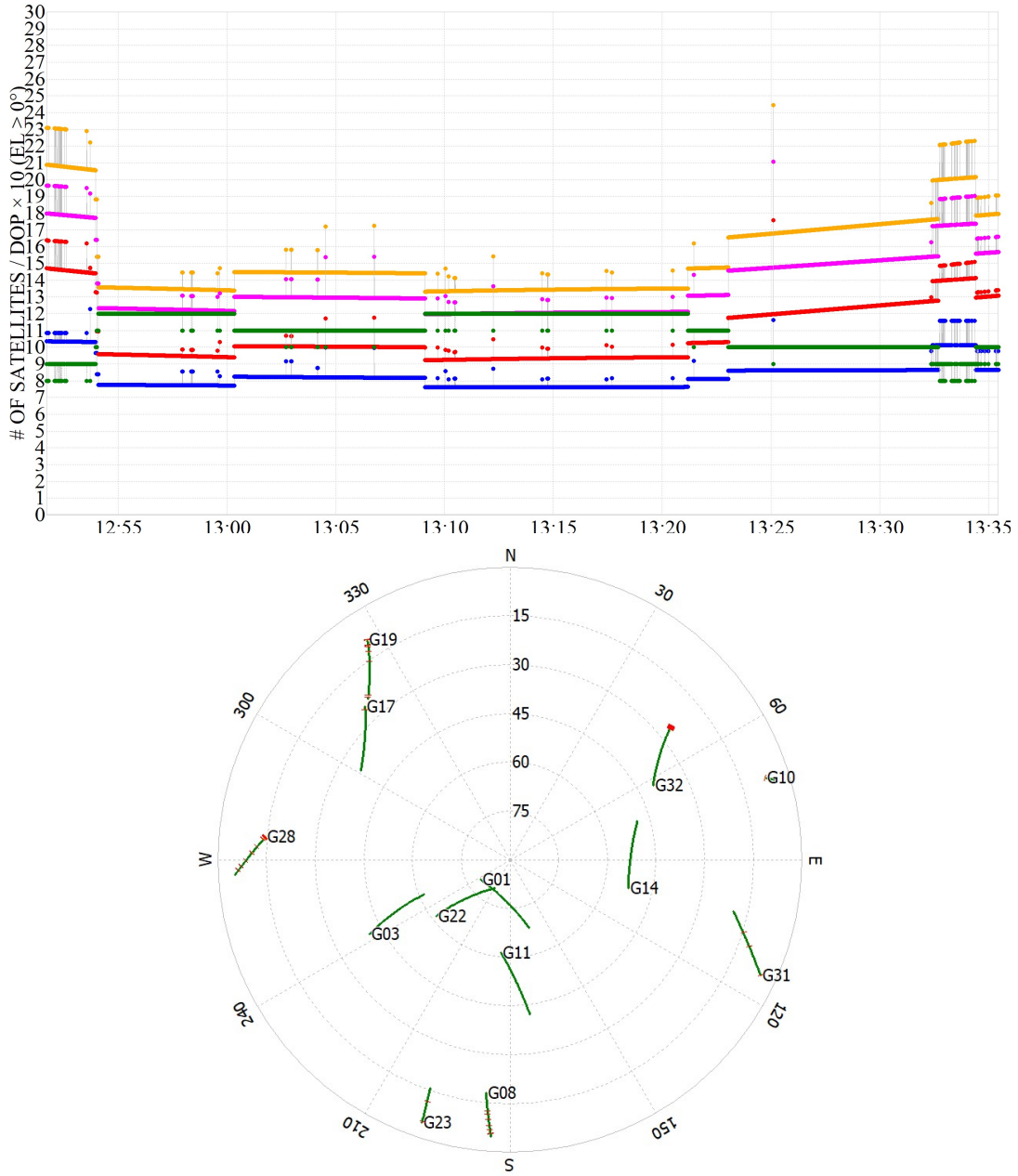


Figure B.14: FWD1017c DOP presented in number of visible satellites divided by DOP (top). Yellow line = GDOP, purple = PDOP, green = number of satellites visible, red = VDOP and blue = HDOP. Together with a skyplot for the satellites during the measurements (bottom)

Department of Space, Earth and Environment
CHALMERS UNIVERSITY OF TECHNOLOGY
Gothenburg, Sweden
www.chalmers.se



CHALMERS
UNIVERSITY OF TECHNOLOGY